

**THE EFFECT OF IRREGULAR FIBER DISTRIBUTION AND ERROR IN
ASSUMED TRANSVERSE FIBER CTE ON THERMALLY INDUCED
FIBER/MATRIX INTERFACIAL STRESSES**

A Thesis

by

SEUNG-DON ZU

Submitted to the Office of Graduate Studies of
Texas A&M University
in partial fulfillment of the requirements for the degree of
MASTER OF SCIENCE

May 2005

Major Subject: Aerospace Engineering

**THE EFFECT OF IRREGULAR FIBER DISTRIBUTION AND ERROR IN
ASSUMED TRANSVERSE FIBER CTE ON THERMALLY INDUCED
FIBER/MATRIX INTERFACIAL STRESSES**

A Thesis

by

SEUNG-DON ZU

Submitted to Texas A&M University
in partial fulfillment of the requirements
for the degree of

MASTER OF SCIENCE

Approved as to style and content by:

John D. Whitcomb
(Chair of Committee)

James Greenup Boyd
(Member)

Terry Creasy
(Member)

Helen L. Reed
(Head of Department)

May 2005

Major Subject: Aerospace Engineering

ABSTRACT

The Effect of Irregular Fiber Distribution and Error in Assumed Transverse Fiber CTE
on Thermally Induced Fiber/matrix Interfacial Stresses. (May 2005)

Seung-Don Zu, B.S, Hankook Aviation University, Korea

Chair of Advisory Committee: Dr. John D. Whitcomb

Thermally induced interfacial stress states between fiber and matrix at cryogenic temperature were studied using three-dimensional finite element based micromechanics. Mismatch of the coefficient of thermal expansion between fiber and matrix, and mismatch of coefficient of thermal expansion between plies with different fiber orientation were considered. In order to approximate irregular fiber distributions and to model irregular fiber arrangements, various types of unit cells, which can represent non-uniformity, were constructed and from the results the worst case of fiber distributions that can have serious stress states were suggested. Since it is difficult to measure the fiber transverse coefficient of thermal expansion at the micro scale, there is an uncertainty problem for stress analysis. In order to investigate the effect of error in assumed fiber transverse coefficient of thermal expansion on thermally induced interfacial stresses, systematic studies were carried out. In this paper, the effect of measurement errors on the local stress states will be studied. Also, in order to determine fiber transverse CTE values from lamina properties, a back calculation method is used for various composite systems.

To my parents, for their love, patience and sacrifices

ACKNOWLEDGEMENTS

I wish to express my deep sense of gratitude to my advisor, Dr. John D. Whitcomb. Without his patience and constant guidance, this work would have never been complete. I really appreciate the time he has taken out of his personal life to help me out. I am thankful from the bottom of my heart to Dr. J. Noh for being my mentor and teammate in this research work and above all for being such a nice friend. I was very fortunate to get a chance to work with him. He played a very important role in this project and his contribution provides the backbone for my research work. I want to thank our research team members Jongil, Jiwoong, Woosik, Deepak, Julian, and Bhavya, for providing a conducive environment for this research work. It was great being part of such a lively and friendly group of people. I am also thankful to all of my friends, especially Seungpyo, Jaesang, Jaehoon, Yusuke, Eunyee, Kyungnam, Brian, and Riecks' family. I am thankful to all the people who have directly or indirectly helped me accomplish whatever I have. Finally, I wish to express my sincere appreciation to my father, mother, sister, and brother for their never-ending support, love, prayers and sacrifices. Without them, I would not have been able to pursue graduate studies here at Texas A&M University.

TABLE OF CONTENTS

	Page
ABSTRACT.....	iii
ACKNOWLEDGEMENTS	v
TABLE OF CONTENTS.....	vi
LIST OF FIGURES.....	viii
LIST OF TABLES	xi
1. INTRODUCTION.....	1
1.1. Background and motivation	1
1.2. Literature review	2
1.3. Objective of research.....	7
2. INTERFACIAL STRESS STATE AND MICROCRACKS	8
2.1. Interfacial stress.....	8
2.2. Microcrack failure mechanisms at interface	9
2.3. Failure scenario	10
2.4. Interface strength.....	11
2.5. Failure criterion.....	11
2.6. Composite systems.....	12
2.6.1. Material properties of fiber and matrix	12
2.6.2. Laminate description	14
3. METHODOLOGY	15
3.1. Introduction	15
3.2. Micro level analysis	16
3.2.1. Representative volume elements.....	16
3.2.2. Periodic unit cells and boundary conditions.....	19
3.2.3. Calculating thermal-elastic effective composite properties	21
3.3. Macro level analysis.....	25
3.4. Interfacial stress state analysis	29
4. RESULTS AND DISCUSSION.....	31

	Page
4.1. Introduction	31
4.2. Study of perfectly regular fiber arrangement cases.....	32
4.2.1. Interfacial stress states induced by thermal loading in a lamina	33
4.2.2. Interfacial stress states induced by ply stresses (indirect mechanical loading) in laminate.....	36
4.2.3. Interfacial stress states induced by combined loadings.....	40
4.2.4. Effect each component of ply stresses on interfacial stresses	45
4.3. Study of large pattern arrangement cases.....	46
4.3.1. Introduction	46
4.3.2. Effect of matrix-rich zones on interfacial stress fields.....	47
4.3.3. Effect of spacing of matrix-rich zones on interfacial stress fields	54
4.3.4. Effect of size of matrix-rich zones on interfacial stress fields	55
4.3.5. Effect of low and high volume fraction areas	58
4.4. The worst fiber distributed case	63
4.5. Uncertainty of fiber transverse CTE	71
4.5.1. Importance of fiber transverse CTE	71
4.5.2. Range of fiber transverse CTE values.....	71
4.5.3. Effect of errors in assumed fiber transverse CTE values on interfacial stresses in lamina.....	73
4.5.4. Sensitivity of lamina CTE to change fiber volume fractions	76
4.5.5. Effect of errors in assumed transverse fiber CTE values on ply stresses in laminate composite.....	78
4.5.6. Effect of errors in assumed fiber transverse CTE values on interfacial stresses for laminate composite.....	79
4.5.7. Effect of errors in assumed fiber transverse CTE values on interfacial stresses in high volume fraction area in laminate composite	83
4.6. Prediction of fiber transverse CTE by back calculation.....	87
5. CONCLUSION	91
REFERENCES	93
APPENDIX A	98
APPENDIX B.....	100
VITA	103

LIST OF FIGURES

	Page
Figure 2.1. Interfacial stress components.....	8
Figure 2.2. Opening and sliding modes.....	9
Figure 2.3. Microcrack initiation and growing scenario	10
Figure 2.4. Segment of sandwich structure of X-33 fuel tank	14
Figure 3.1. Mechanism of thermally induced indirect mechanical loading.....	15
Figure 3.2. Three Steps to obtain thermally induced interfacial stress states.	16
Figure 3.3. Various unit cells.	18
Figure 3.4. Square and hexagonal unit cells.....	19
Figure 3.5. Laminate composite.....	26
Figure 3.6. Coordinate systems	26
Figure 3.7. Cartesian and cylindrical coordinate systems.....	30
Figure 4.1. Perfect periodic arrangement unit cells	32
Figure 4.2. Interfacial stress states of square array induced by thermal loading in a lamina	33
Figure 4.3. Interfacial stress states of hexagonal array induced by thermal loading in a lamina	34
Figure 4.4. Interfacial stress states induced by indirect mechanical loadings of square unit cell	37
Figure 4.5. Interfacial stress states induced by indirect mechanical loadings of hexagonal unit cell	38

	Page
Figure 4.6. The relationship between interfacial stresses and loading direction.....	39
Figure 4.7. Interfacial stress states induced by combined loadings of square unit cell.....	42
Figure 4.8. Interfacial stress states induced by combined loadings of hexagonal unit cell	43
Figure 4.9. Effect of ply stresses σ_1 and σ_2 on the interfacial stress states.....	45
Figure 4.10. Unit cell having matrix-rich zone in center (one fiber missed case).	47
Figure 4.11. Interfacial stress fields of perfectly regular unit cell and one fiber missed unit cell.....	48
Figure 4.12. Interfacial stress states due to laminate effect of hexagonal and one fiber missed unit cell.....	51
Figure 4.13. Interfacial stress states of on fiber missed unit cell.	52
Figure 4.14. Unit cells that are missing one fiber in center.	54
Figure 4.15. Interfacial stress state of one fiber missed unit cells.....	55
Figure 4.16. Unit cells that are having different quantity of matrix.....	56
Figure 4.17. Interfacial stress states of 6 fiber missed and 1 fiber missed unit cells	57
Figure 4.18. High volume fraction zones and low volume fraction zones.....	58
Figure 4.19. Unit cells to represent high and low volume fraction zones.....	59
Figure 4.20. Four step processes.	60
Figure 4.21. Non-uniformly distributed ply stresses.....	61
Figure 4.22. Interfacial stresses of a fiber located in low volume fraction area.	62
Figure 4.23. Debonding and microcrack areas.....	64

	Page
Figure 4.24. Debonding and microcrack areas of 6 fiber missed large pattern unit cell...	65
Figure 4.25. 8 fibers for 5 assumed fiber distributions	68
Figure 4.26. Interfacial stress states for the smallest and largest fiber transverse CTE values in lamina.....	73
Figure 4.27. Composite cylinder model.....	74
Figure 4.28. Sensitivity of effective lamina transverse CTE to fiber volume fraction.	77
Figure 4.29. Interfacial stress states for assumed fiber transverse CTE values in a laminate	81
Figure 4.30. Unit cells for low and high volume fraction areas.....	83
Figure 4.31. Interfacial stresses of a fiber in high volume fraction area.....	86
Figure 4.32. Flowchart of back calculation for predicting the fiber transverse CTE.....	88

LIST OF TABLES

	Page
Table 2.1. Material properties of IM7/977-2 [19, 26] and HTA/#113	13
Table 3.1. The effective thermal-elastic properties (60% fiber volume fraction).....	25
Table 3.2. The ply stresses and strains of each layer of inner facesheet in the material coordinate system	27
Table 3.3. The ply stresses and strains of each layer of outer facesheet in the material coordinate system	28
Table 4.1. Interfacial stresses induced by thermal of square array unit cell	33
Table 4.2. Interfacial stresses induced by thermal of hexagonal array unit cell	34
Table 4.3. Interfacial stresses induced by ply stresses of square array unit cell	37
Table 4.4. Interfacial stresses induced by ply stresses of hexagonal array unit cell	38
Table 4.5. Comparing one fiber missed cases with hexagonal case	50
Table 4.6. Ranking of interfacial stresses of 8 fibers caused by thermal loading of a laminate	69
Table 4.7. Ranking of interfacial stresses of 8 fibers caused by thermal loading of unidirectional lamina.....	70
Table 4.8. Ranking of interfacial stresses of 8 fibers caused by mechanical loading of unidirectional lamina in transverse direction	70
Table 4.9. CTE values of IM7 carbon fiber in literatures	72
Table 4.10. Variations of difference between fiber and matrix CTE values.....	72
Table 4.11. Sensitivity of effective lamina transverse CTE to fiber volume fraction.....	78

	Page
Table 4.12. Ply level stresses for smallest and largest fiber transverse CTE values in [90/±45/0] _s composite	79
Table 4.13. Variation of radial stresses for fiber transverse CTE values.....	82
Table 4.14. Average stresses of low and high volume fraction areas	85
Table 4.15. Stress variation for scattered fiber transverse CTE values.....	86
Table 4.16. Results of back calculation for fiber transverse CTE values	90

1. INTRODUCTION

1.1. Background and motivation

One of the most critical issues in space vehicle technology is to reduce the cost of space vehicle. One way of reducing costs is to manufacture reusable light weight space vehicles. In order to achieve this, NASA researchers have tried to manufacture single-state-to-orbit (SSTO) reusable launch vehicles (RLVs) where the total payload of the vehicle is reduced by fabricating it from composite materials. Composite materials have been used for aircraft manufacture because of their high stiffness and light weight. The advantages of composite materials should make them widely used in the space vehicle industry. For reusability, the choice of RLV propellant was liquid hydrogen fuel instead of solid propellant, and its fuel tank must be made of composite materials instead of metallic materials to reduce the total weight of the RLV.

Liquid hydrogen (LH_2) fuel tanks are the single largest structural component of an RLV. So the design of light weight fuel tanks is critical for reducing the cost of space access. Carbon fiber reinforced polymer (CFRP) composite tanks have been proposed to reduce the weight of the RLV [1]. It is known that CFRP composite fuel tanks can reduce vehicle weight by 40% [2]. It seemed that CFRP composites were very suitable for fuel tanks of RLV because of its light weight. However, during its test, the liquid hydrogen fuel tanks showed serious problems.

NASA's researchers found out that microcracks caused by combined thermal and mechanical loadings lead to failure of the fuel tank. Since the RLV uses liquid hydrogen and liquid oxygen for propulsion, the fuel needs to be stored at a cryogenic temperature around 20K [3]. When the RLV re-enters the atmosphere with empty tanks, the fuel tank reaches around 400K [3]. Since composite materials are composed of anisotropic layers oriented in different directions, each layer may have a different coefficient of thermal expansion (CTE), and the CTE mismatch of the layers will cause thermal stresses in the laminate. Also since the CTE values of the fiber and matrix are different, additional thermal stress due to the mismatch of CTE between fiber and matrix will arise. These thermal stresses produce high strain energy that is relieved when microcracks form. If the microcracks connect to form a leakage path, the small molecules of liquid hydrogen can pass through the laminate [3]. According to the final report regarding the X-33 [4], it is known that most composite materials will form microcracks at cryogenic temperature due to large transverse thermal stresses, large ply stresses, and low transverse matrix strength.

1.2. Literature review

The purpose of this literature review is to provide sufficient background information for this research and to identify the difference between our work and what the others have done. Extensive research about many aspects of the interfacial stress states between fiber and matrix have been done by many researchers. Various materials for reinforcements and matrix have been used, various loading conditions and situations

have been considered, and several kinds of fiber distribution assumptions have been considered. Before the literature survey is started, it is needed to organize these various works done by many researchers in order to explain them efficiently.

The methods that other researchers have used for micromechanics will be investigated. There are three methods; analytical method, experimental method, and numerical methods such as Boundary Element Method (BEM) and Finite Element Method (FEM).

In 2003, F. Paris [5] employed the BEM for a square array model that permits the development of contact zone between the debonded surfaces of the fiber and the matrix, and their results have been checked experimentally by means of the performance of a series of two dimensional loading tests.

Kouris et al. in 1991 [6] modeled two inhomogeneities that sustain an eigenstrain loading, and solved the plane strain problem analytically. They considered two circular inhomogeneities embedded in an infinite elastic region. In 1996, George [7] used the Mori-Tanaka method to derive stress concentration factors and determine the interfacial stress fields for coated and uncoated fiber. In 2001, H. S Choi et al. [8] used the boundary element method for a hexagonal array model. They compared their numerical results with the elastic solution of a three-phase cylindrical model.

It seems that the Finite Element method is more popular than the other method for micromechanics. Many researchers [9, 10, 11, 12, 13, 14, 15, 16, 17, 18, 19, 20, 21, 22, 23, 24, 25] have used FEM to determine the interfacial stress states.

In 1991, David E. Bowles [9] obtained the interfacial stresses caused by different CTE values of fiber and matrix due to thermal loading and macro level stresses due to laminate effects for fibers arranged in a perfect square array case. His results indicate that matrix stresses varied with laminate orientation and circumferential position around the fiber. He also found that the fiber thermal-elastic properties of fibers have a minimal effect on the overall magnitudes of thermally induced stresses.

In 1991, H. Zhu et al. [10] investigated radial matrix cracking and interface failure for transverse loading of a hexagonal array fiber composite. They modeled the interphase by a layer of radial and circumferential spring elements, adopting a tensile stress criterion for initiation of matrix cracking, and employed a strain-energy density criterion for interphase failure.

B. F. Sorensne and R. Talreja [11] in 1993 investigated interfacial stresses for square and hexagonal periodic unit cells, when composites are in cool-down process. They studied the effect of distance between fibers on interfacial stresses, while the distance of fibers is closed. They used the maximum stress criterion to determine initial failure. They tried to explain the failure initiation by using the maximum stress criterion.

In 1994 N. Chander [12] studied thermally induced residual stresses for two classes of composites, metal matrix composite Ti-6Al-4V/SCS-6 and intermetallic matrix composite Ti-24A-11Nb/SCS-6. By studying regular rectangular and diagonal arrays, they found that stress distributions, the magnitude, and the location of maximum stress depend on fiber arrangements.

In 1996, George and Michal [7] proposed initial failure maps for ceramic and metal matrix composite laminates for coated and uncoated fibers and proposed the initial failure maps which were constructed for several symmetric laminates and composite systems loaded by uniform membrane stresses.

In 1997, A. Thiounet et al. [25] studied that the debonding phenomena between fiber and matrix of a long fiber Sic/Ti metal matrix composites. Their work was carried out both with and without consideration of the manufacturing residual stresses. They used a quadratic form criterion proposed by Wisnom [13] to predict interface failure, but they assumed the value of interface strength.

B. Feldler [14] in 2001 used FEA to calculate interfacial stress fields and determined the initial matrix failure in CFRP under static transverse tensile load. Considering the effect of neighboring fibers, they modeled a hexagonal unit cell, and made plots of stress distributions as a function of the arc distance. They insisted that the Von Mises criterion is not suitable to predict the initial matrix failure in fiber-reinforced composites. They obtained interfacial strength of the composite by experimental test in 2002 [15].

In 2001, H. S Choi et al. [8] used the boundary element method for a hexagonal array model to study the effects of changes in interphase stiffness, cooling temperatures, fiber volumes, and loads on stress distributions in the interphase and the load-displacement behaviors of silicon carbide/aluminum composite lamina, while the silicon carbide/aluminum composite with hexagonal fiber array and thermal stresses are

subjected to monotonically increasing transverse tensile loads. They compared their numerical results with elastic solution of a three-phase cylindrical model.

In 2002 W. Ding [16] studied factors affecting transverse properties of the composites, such as thermal residual stresses caused by cooling from the composite processing temperatures, fiber/matrix interface conditions, fiber volume fractions, fiber spacing, and test temperature. They employed a hexagonal fiber packing model with a weak fiber/matrix interfacial strength to predict the transverse tensile behavior of the Ti-6-4/SM1140 composite.

Wen et al. [17] in 2002 obtained the effective lamina properties for a quarter square unit cell and interfacial stress fields for longitudinal and transverse tensile load and combined tensile and thermal load. They also calculated strain energy release rate for various degrees of fiber/matrix debonding under transverse tension, thermal and combined loading conditions. They finally predicted the loss in stiffness due to the aforementioned load.

In 2004, M. M Agbdam [18] developed three-dimensional FEM to study effects of thermal residual stress, fiber coating and interface bonding on the transverse behavior of a unidirectional Sic/Ti-6Al-4V metal composite. He used two different failure criterion, which accounted for normal and shear stresses across the interfaces, to predict the failure of the fiber/coating and coating/matrix interfaces.

1.3. Objectives of this study

Various methods have been used by many researchers to investigate interfacial stress states that can cause interfacial debonding. The majority of these researches are related to periodic fiber distribution. However, since actual composites have randomly distributed fiber arrangements, these perfect regular arrangement assumptions have limitations to predict exact phenomena of real composites because the interfacial stresses are affected by the location of neighboring fibers. Also some researchers performed randomly distributed fiber cases. However, even though analysis of random cases for certain composites is performed, the same fiber arrangement cases can not be expected for different composites. The objective of this thesis is to approximate irregularity of fiber distributions and model irregular fiber arrangements, and find out the characteristic of thermally induced interfacial stresses. The worst case of fiber distributions that can have serious stress states will be investigated by extensive parametric studies.

The fiber transverse CTE values were measured by experimental tests [26], and the scattered measurement values for the average fiber CTE value were noted. The scattered test results cause an uncertainty problem for fiber transverse CTE. For this work, systematic studies will be carried out to understand the effect of CTE variation. In this paper, using the known range of measurement values, it will be investigated how much the scattered measurement errors will make different results for effective properties of composite and local stresses. Also, in order to determine fiber transverse CTE values by numerical approach, a back calculation method is used for various composite systems.

2. INTERFACIAL STRESS

2.1. Interfacial stresses

A composite material consists of a combination of two or more constituents, in which the individual components retain their separate identities. The term composite often implies that the physical properties are improved since the main interest technologically is in obtaining materials with superior physical (usually mechanical) properties to those of the composite's component materials. The interface in a composite material can be defined as a surface that forms a boundary between two constituents such as fiber and matrix. When a composite material is subjected to thermal loads, local stresses develop within the composite due to mismatch between the coefficients of thermal expansion (CTE). The local stresses caused at the interface are called as interfacial stresses. Figure 2.1 defines the interfacial stress components in a cylindrical coordinate system.

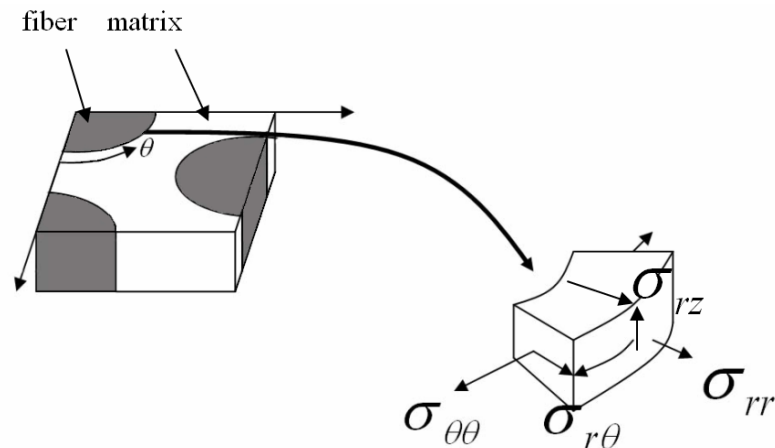


Figure 2.1. Interfacial stress components

2.2. Microcrack failure mechanism at interface

In this section, possible damage modes which can be caused at the micro level are described. The four schematic microcrack illustrations of cracks initiating from the interface are shown in Figure 2.2. Based on the maximum stress criterion, the radial stress σ_{rr} will cause opening mode, the shear stress $\sigma_{r\theta}$ will cause a torsional sliding mode, another shear stress σ_{rz} will cause an axial sliding mode, and the tangential stress $\sigma_{\theta\theta}$ will cause circumferential matrix crack mode. Also it is possible that a combination of the stress components can cause microcracks.

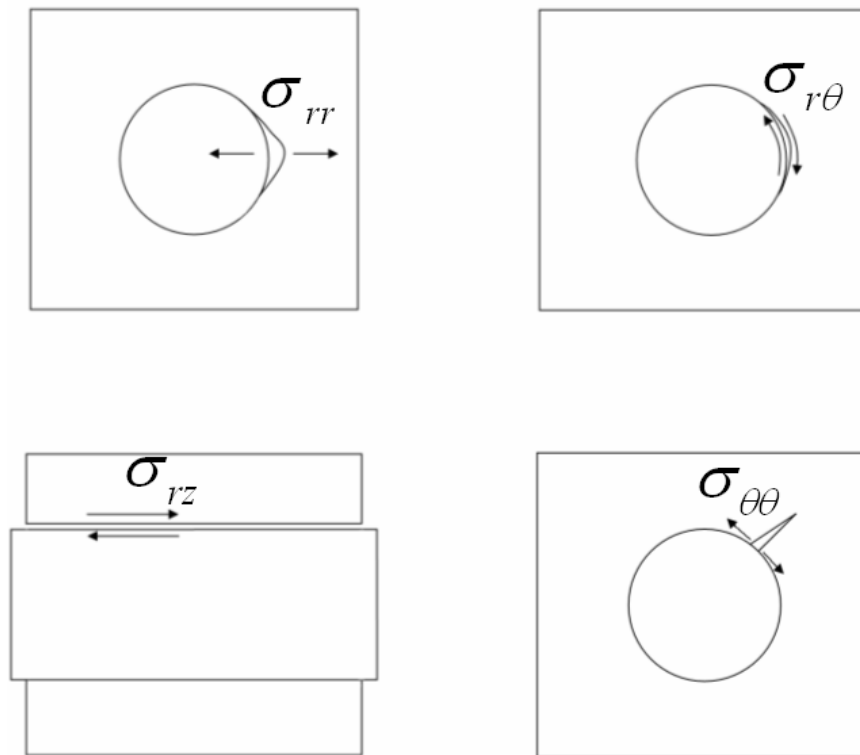


Figure 2.2. Opening and sliding modes

2-3. Failure scenario

It is known that fiber-matrix debonding running circumferentially caused by the radial and shear stresses is the first step of failure at micromechanical level, because of the poor interface bonding [5]. After these cracks have grown to a certain length, they are linked to each other by a matrix crack caused by tangential stress. Finally, these microcracks, which are caused locally, are connected and transverse matrix cracks (TMC) are formed. This TMC reduces the stiffness of the composite and the load carrying capacity in the transverse direction. When these TMCs and delaminations between layers are connected, damage networks form. Figure 2.3 shows the initiation of fiber/matrix debonding and their growth.

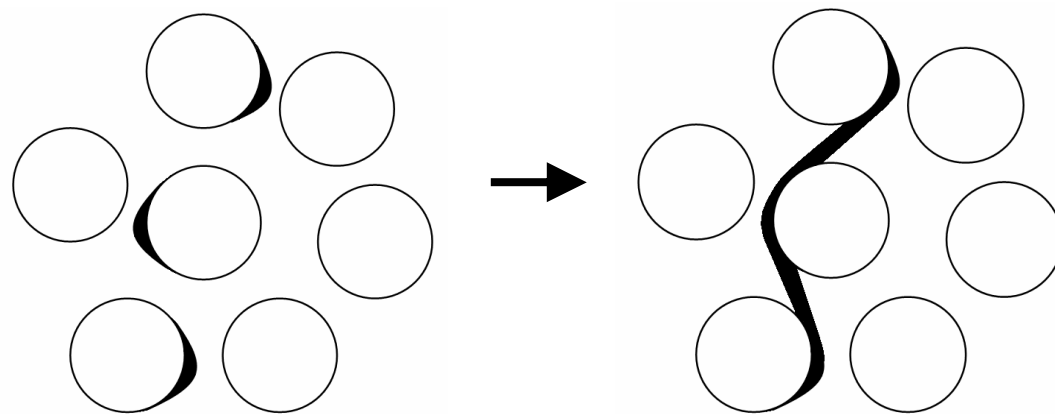


Figure 2.3. Microcrack initiation and growing scenario

2.4. Interface strength

For a homogeneous material, if applied stresses are higher than the critical strength of the material, it is said that the material has failed, and the critical strength can be measured by experimental tests. However, if the scale of interest is micro level having interface consisting of two different materials, the failure problem becomes very difficult, because of the difficulty for measuring interface strengths in micro level. It is known that the interface strengths are less than those of the composite constituents [14]. When considering that the tensile strength of 977-2 epoxy resin is 77Mpa, it can be assumed that the interface strength between IM7 carbon fiber and 977-2 epoxy resin is less than 77Mpa. Unfortunately the interfacial strengths of the IM7/977-2 composite are not known yet. Since the interfacial strength of carbon epoxy HTA/# 113 composite, whose thermal-elastic properties are similar with the IM7/977-2, were obtained by Fiedler et al. [14], the interfacial strength of the IM7/977-2 will be assumed to predict the interfacial failure problem for this work.

2.5. Failure criterion

Once the interface strengths are defined and interfacial stresses are obtained, an applicable interface failure criterion will be needed to determine failure possibility. Many criteria have been proposed. The simplest criterion is the maximum stress criterion, i.e., crack initiates when the maximum value of the tensile stress normal to the crack plane reaches a critical value. Li and Wisnom [13] proposed the following criterion,

$$\frac{\sigma_{rr}}{S} + \left(\frac{\sigma_{r\theta}}{S} \right)^2 = 1 \quad (2.1)$$

where σ_{rr} and $\sigma_{r\theta}$ are the interfacial radial and shear stress, respectively and S is the interface tensile strength. This failure criterion was used for a simple SiC/Ti system without coating. They denoted that this criterion is an empirical equation with no rigorous theoretical basis. Li and Wisnom proposed another criterion based on the maximum principle stress for coated fiber later. The failure criterion can be expressed as,

$$S = \frac{\sigma_{rr} + \sigma_{\theta\theta}}{2} + \sqrt{\left(\frac{\sigma_{rr} - \sigma_{\theta\theta}}{2} \right)^2 + \sigma_{r\theta}^2} \quad (2.2)$$

where σ_{rr} , $\sigma_{r\theta}$, and $\sigma_{\theta\theta}$ are the interfacial radial, shear stress, and hoop stresses, respectively and S is the interface tensile strength. Other criterion, e.g. Von Mises criterion and strain energy density criterion were used by many researchers to determine interfacial failure. Unfortunately there is no universally accepted criterion for fiber debonding. In this study, the maximum stress criterion will be assumed to control the crack initiation.

2.6. Composite systems

2.6.1. Material properties of fiber and matrix

Carbon/epoxy IM7/977-2 composite system, which is used for the LH2 fuel tank, is studied for this research. The thermal-elastic material properties of each constituent are noted in Table 2.1. In order to apply the maximum stress criterion for predicting

interfacial failure, interfacial strengths of the IM7/977-2 are assumed. Carbon epoxy HTA/#113, whose thermal-elastic properties are similar with the IM7/977-2, were obtained by Fiedler et al. [14]. The material properties and interfacial strengths of carbon epoxy HTA/#113 are also presented in Table 2.1. Since the IM7/977-2 and HTA/#113 have similar thermal-elastic properties of each constituent, it is assumed that the interfacial tensile strength of the IM7/977-2 is 64 MPa, and the interfacial shear strength is 33 MPa.

Table 2.1. Material properties of IM7/977-2 [19, 26] and HTA/#113 [15]

	IM7 carbon fiber	977-2 epoxy	HTA carbon fiber	#113 epoxy
E_{11} (GPa)	263.7	3.32	235	3.9
E_{22}, E_{33} (GPa)	19.0	3.32	19.1	3.9
ν_{12}, ν_{13}	0.2	0.35	0.28	0.39
ν_{23}	0.35	0.35	0.33	0.39
G_{12}, G_{13} (GPa)	27.6	1.23	24	1.45
G_{23} (GPa)	6.89	1.23	7.2	1.45
$\alpha_{11} (\times 10^{-6} / C^{\circ})$	-0.4	57.6	0.4	57
$\alpha_{22}, \alpha_{33} (\times 10^{-6} / C^{\circ})$	5.63	57.6	10	57
Tensile Strength (MPa)	2850	77	NA	95.5
Shear Strength (MPa)	NA	86.9	NA	71
	Interface		Interface	
Interfacial tensile Strength (MPa)	64 (assumed)		64	
Interfacial Shear Strength (MPa)	33 (assumed)		33	

NA: Not available

2.6.2. Laminate description

The liquid hydrogen tank is a honeycomb composite sandwich structure consisting of an outer facesheet, honeycomb core, and inner facesheet shown in the Figure 2.4 [4]. The outer facesheet is a 7-ply, IM7/977-2 laminate (0.034 in. thick) with stacking sequence $[65/0/-65/90/-65/0/65]_T$. The core is a honeycomb Korex 3/16 -3.0 (1.5 in. thick). The inner facesheet is a 13-ply, IM7/977-2 laminate (0.066 in. thick) with stacking sequence $[45/90_3/-45/0_3/-45/90_3/45]_T$.

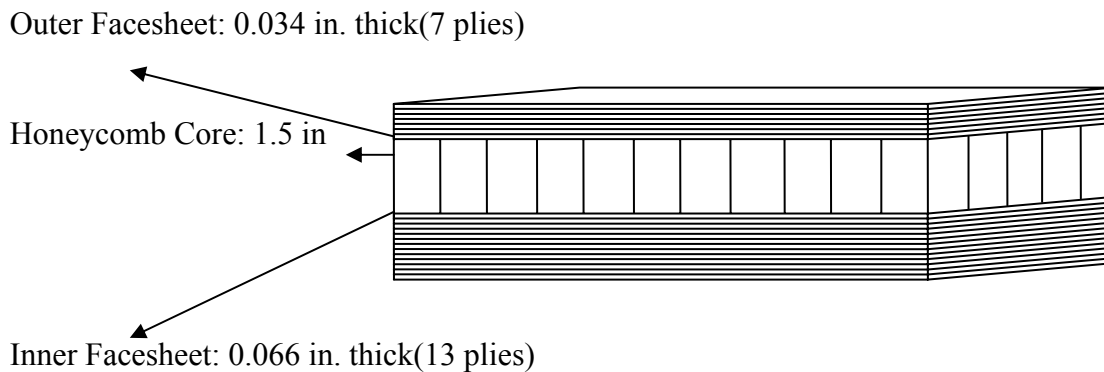


Figure 2.4. Segment of sandwich structure of X-33 fuel tank

3. METHODOLOGY

3.1. Introduction

When a fuel tank of the X-33 is subjected to cryogenic temperature, the composite material of the tank induces two kinds of thermal stresses. One is caused by the mismatch of CTE between fiber and matrix, and the other is caused by the mismatch of CTE of plies with different fiber orientations described in Figure 3.1. The macro level loading caused by the mismatch of CTE of plies with different fiber orientations will be called indirect mechanical loading caused by laminate effect in this study. Since there exist the macro (or ply) level stress due to laminate effects, these macro level stresses and strains will affect the interfacial stress fields. Figure 3.2 describes the study processes. For the micro level analysis, three-dimensional finite element methods are employed to estimate the effective thermal-elastic properties in Figure 3.2 (a). For the second step, macro level analysis is studied to obtain thermal stresses and strains caused by different CTE values of each layer by using Classical Laminate Plate Theory (CLPT) in Figure 3.2 (b).

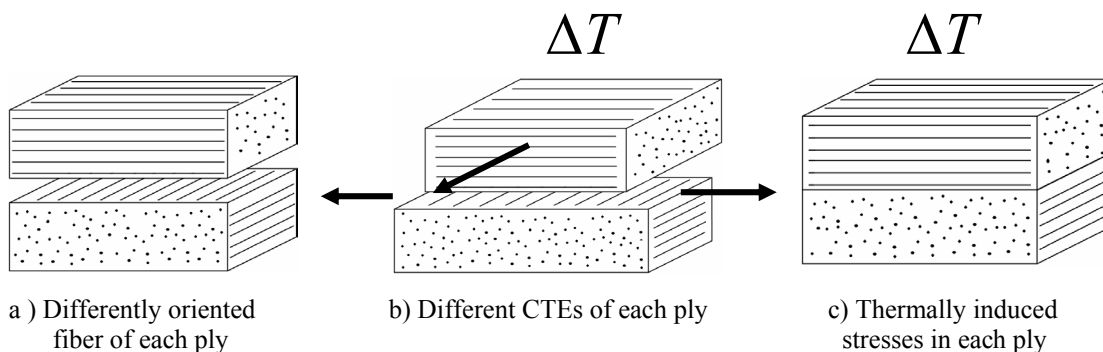


Figure 3.1. Mechanism of thermally induced indirect mechanical loading

For the third step, FEM is employed again to determine the interfacial stress states between fiber and matrix in Figure 3.2 (c).

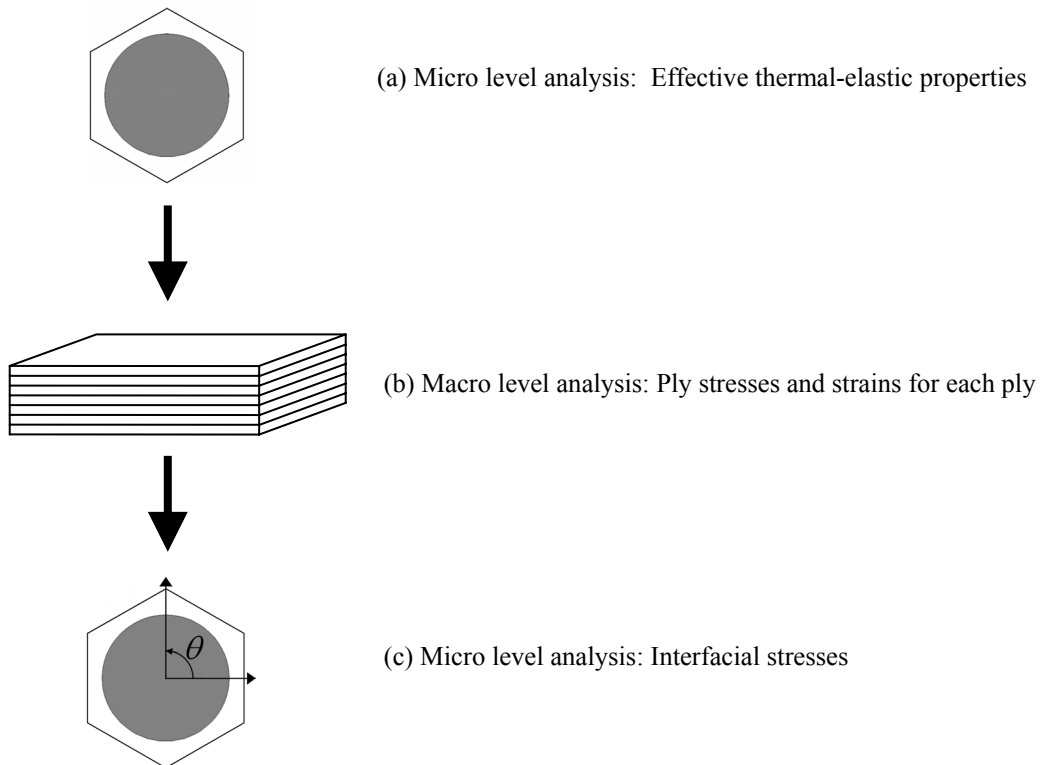


Figure 3.2. Three Steps to obtain thermally induced interfacial stress states

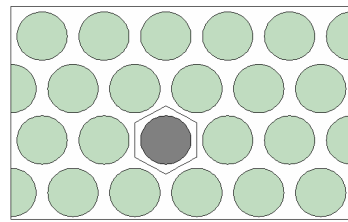
3.2. Micro level analysis

3.2.1. Representative volume element (RVE)

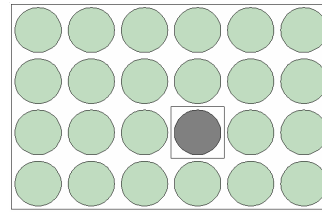
A unidirectional fiber reinforced composite has randomly distributed fibers in matrix over the cross section perpendicular to the fibers. It is not easy to model the composite behavior with the real constituent geometry. Therefore, it is often assumed

that the fibers are uniformly distributed in a periodic pattern for purpose of analysis. This step of defining a periodic pattern is to select the smallest repeating area. Common packing patterns are square array and hexagonal array in Figure 3.3 (a) and (b). These perfectly periodic arrangements have been used for micromechanics. However, these perfect regular assumptions have limitation to predict exact phenomena of real composites. In order to approximate irregularly distributed fiber arrangements, the unit cells c), d), e), f), g), and h) in Figure 3.3 are constructed for extended studies of randomly distributed fiber arrangements. These types of unit cells are called large pattern array in this study. These large pattern arrays contain several fibers, and are repeated periodically, but they will more represent irregularly distributed fiber arrays than perfect array unit cells such as square and hexagonal unit cells. The large pattern c), d), e), and f) will be used for studying the effect of matrix rich zones on interfacial stresses, and the large pattern g) and h) will be used for studying the effect of low fiber volume fraction areas and high fiber volume fraction areas on averaged stresses and interfacial stresses in section 4.

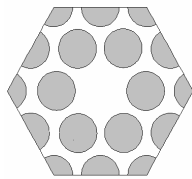
For the micro level analysis step, perfect square and hexagonal array unit cells, and large pattern unit cells are used to estimate the effective thermal-elastic. The basic assumptions regarding geometry, material properties, and loading conditions are presented below.



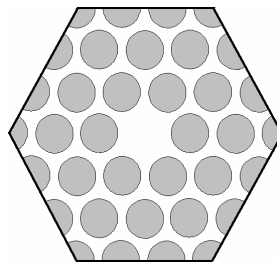
a) Perfect hexagonal array



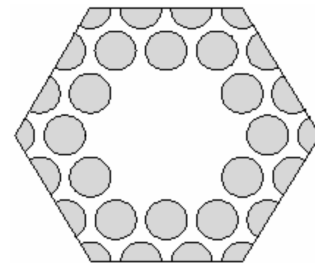
b) Perfect square array



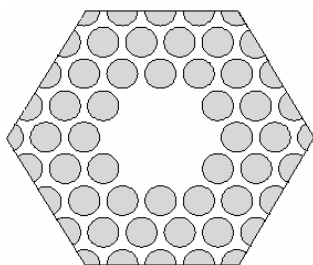
c) Large pattern 1



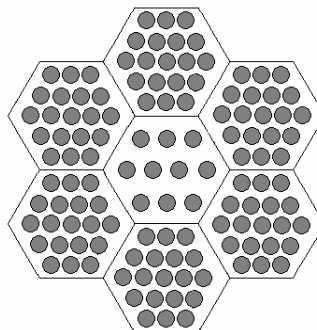
d) Large pattern 2



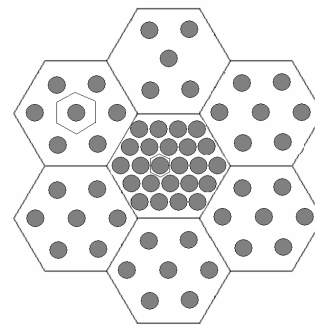
e) Large pattern 3



f) Large pattern 4



g) Large pattern 5



h) Large pattern 6

Figure 3.3. Various unit cells

1. The fibers are circular in cross-section and continuous, straight, and infinitely long in the longitudinal direction.
2. The fibers are arranged in periodic patterns.
3. The fibers are homogeneous, linearly elastic and transversely isotropic.
4. The matrix is homogeneous, linearly elastic and isotropic.
5. The fiber and matrix are perfectly bonded at the interface.
6. The temperature is uniform throughout the body.
7. The mechanical loadings are applied at infinity.

3.2.2. Periodic unit cells and boundary conditions

Once periodicity pattern is defined, the boundary conditions for the unit cell should be constructed. For two kinds of basic unit cells such as square and hexagonal arrangements in Figure 3.4, their correct boundary conditions are presented below [27, 28]. Note that the origins of coordinate system are located in the center of the unit cells.

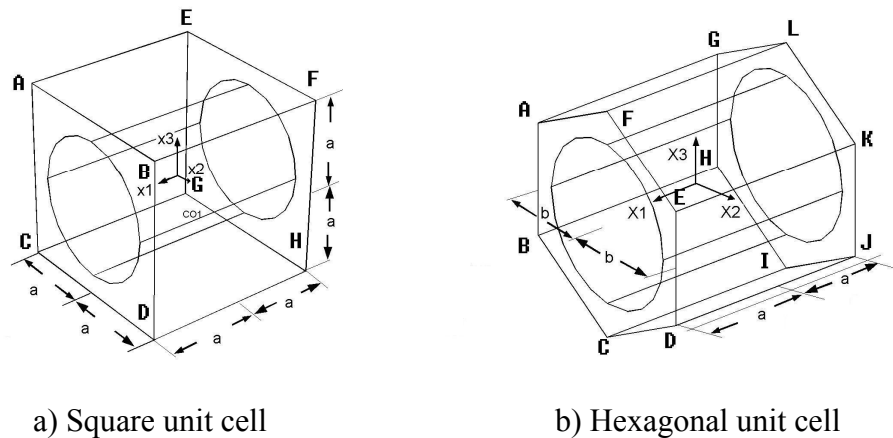


Figure 3.4. Square and hexagonal unit cells

Boundary conditions for the square unit cell

Between ABCD and EFGH

$$\begin{aligned}
 u_1(a, x_2, x_3) &= u_1(-a, x_2, x_3) + \left\langle \frac{\partial u_1}{\partial x_1} \right\rangle 2a \\
 u_2(a, x_2, x_3) &= u_2(-a, x_2, x_3) + \left\langle \frac{\partial u_2}{\partial x_1} \right\rangle 2a \\
 u_3(a, x_2, x_3) &= u_3(-a, x_2, x_3) + \left\langle \frac{\partial u_3}{\partial x_1} \right\rangle 2a
 \end{aligned} \tag{3.1}$$

Between ABEG and CDFH

$$\begin{aligned}
 u_1(x_1, x_2, a) &= u_1(x_1, x_2, -a) + \left\langle \frac{\partial u_1}{\partial x_3} \right\rangle 2a \\
 u_2(x_1, x_2, a) &= u_2(x_1, x_2, -a) + \left\langle \frac{\partial u_2}{\partial x_3} \right\rangle 2a \\
 u_3(x_1, x_2, a) &= u_3(x_1, x_2, -a) + \left\langle \frac{\partial u_3}{\partial x_3} \right\rangle 2a
 \end{aligned} \tag{3.2}$$

Between ADEF and BCGH

$$\begin{aligned}
 u_1(x_1, x_2, a) &= u_1(x_1, x_2, -a) + \left\langle \frac{\partial u_1}{\partial x_3} \right\rangle 2a \\
 u_2(x_1, x_2, a) &= u_2(x_1, x_2, -a) + \left\langle \frac{\partial u_2}{\partial x_3} \right\rangle 2a \\
 u_3(x_1, x_2, a) &= u_3(x_1, x_2, -a) + \left\langle \frac{\partial u_3}{\partial x_3} \right\rangle 2a
 \end{aligned} \tag{3.3}$$

Boundary conditions for the hexagonal Array

Between ABCDEF and GHIJKL

$$\begin{aligned}
 u_1(a, x_2, x_3) &= u_1(-a, x_2, x_3) + \left\langle \frac{\partial u_1}{\partial x_1} \right\rangle 2a \\
 u_2(a, x_2, x_3) &= u_2(-a, x_2, x_3) + \left\langle \frac{\partial u_2}{\partial x_1} \right\rangle 2a \\
 u_3(a, x_2, x_3) &= u_3(-a, x_2, x_3) + \left\langle \frac{\partial u_3}{\partial x_1} \right\rangle 2a
 \end{aligned} \tag{3.4}$$

Between BCHI and FELK

$$\begin{aligned}
 u_1(x_1, b, x_3) &= u_1(x_1, -b, x_3) + \left\langle \frac{\partial u_1}{\partial x_2} \right\rangle 2a \\
 u_2(x_1, b, x_3) &= u_2(x_1, -b, x_3) + \left\langle \frac{\partial u_2}{\partial x_2} \right\rangle 2a \\
 u_3(x_1, b, x_3) &= u_3(x_1, -b, x_3) + \left\langle \frac{\partial u_3}{\partial x_2} \right\rangle 2a
 \end{aligned} \tag{3.5}$$

Between ABHG and EDJK

$$\begin{aligned}
 u_1(x_1, -y + \sqrt{3}z = 2b) &= u_1(x_1, -y + \sqrt{3}z = -2b) + \left\langle \frac{\partial u_1}{\partial x_2} \right\rangle b - \left\langle \frac{\partial u_1}{\partial x_3} \right\rangle \sqrt{3}b \\
 u_2(x_1, -y + \sqrt{3}z = 2b) &= u_2(x_1, -y + \sqrt{3}z = -2b) + \left\langle \frac{\partial u_2}{\partial x_2} \right\rangle b - \left\langle \frac{\partial u_2}{\partial x_3} \right\rangle \sqrt{3}b \\
 u_3(x_1, -y + \sqrt{3}z = 2b) &= u_3(x_1, -y + \sqrt{3}z = -2b) + \left\langle \frac{\partial u_3}{\partial x_2} \right\rangle b - \left\langle \frac{\partial u_3}{\partial x_3} \right\rangle \sqrt{3}b
 \end{aligned} \tag{3.6}$$

Between CDJI and AFGL

$$\begin{aligned}
 u_1(x_1, y + \sqrt{3}z = 2b) &= u_1(x_1, y + \sqrt{3}z = -2b) + \left\langle \frac{\partial u_1}{\partial x_2} \right\rangle b + \left\langle \frac{\partial u_1}{\partial x_3} \right\rangle \sqrt{3}b \\
 u_2(x_1, y + \sqrt{3}z = 2b) &= u_2(x_1, y + \sqrt{3}z = -2b) + \left\langle \frac{\partial u_2}{\partial x_2} \right\rangle b + \left\langle \frac{\partial u_2}{\partial x_3} \right\rangle \sqrt{3}b \\
 u_3(x_1, y + \sqrt{3}z = 2b) &= u_3(x_1, y + \sqrt{3}z = -2b) + \left\langle \frac{\partial u_3}{\partial x_2} \right\rangle b + \left\langle \frac{\partial u_3}{\partial x_3} \right\rangle \sqrt{3}b
 \end{aligned} \tag{3.7}$$

3.2.3. Calculating effective thermal-elastic composite properties

The determination of effective thermal-elastic properties of a composite using three-dimensional finite element analysis requires the determination of volume averaged stresses and strains under the appropriate periodic boundary conditions. The stresses and strains are averaged over the volume of the RVE. The effective stiffness tensor C_{ijkl}^* and coefficient of thermal expansion tensor α_{kl}^* of the composite are calculated from the tensor relation

$$\int_V \sigma_{ij} dV = C_{ijkl}^* \int_V (\varepsilon_{kl} - \alpha_{kl}^* \Delta T) dV \quad (3.8)$$

where σ_{ij} are the stresses, ε_{kl} are the strains, and ΔT is the difference in temperature.

Since stiffness, stress, and strain are symmetric, Equation (3.8) can be expressed in contracted (Voigt) notation as

$$\begin{Bmatrix} \langle \sigma_{11} \rangle \\ \langle \sigma_{22} \rangle \\ \langle \sigma_{33} \rangle \\ \langle \sigma_{23} \rangle \\ \langle \sigma_{13} \rangle \\ \langle \sigma_{12} \rangle \end{Bmatrix} = \begin{pmatrix} C_{11}^* & C_{12}^* & C_{12}^* & 0 & 0 & 0 \\ C_{12}^* & C_{22}^* & C_{23}^* & 0 & 0 & 0 \\ C_{12}^* & C_{23}^* & C_{22}^* & 0 & 0 & 0 \\ 0 & 0 & 0 & \frac{C_{22}^* - C_{23}^*}{2} & 0 & 0 \\ 0 & 0 & 0 & 0 & C_{66}^* & 0 \\ 0 & 0 & 0 & 0 & 0 & C_{66}^* \end{pmatrix} \begin{Bmatrix} \langle \varepsilon_{11} \rangle \\ \langle \varepsilon_{22} \rangle \\ \langle \varepsilon_{33} \rangle \\ \langle \varepsilon_{23} \rangle \\ \langle \varepsilon_{13} \rangle \\ \langle \varepsilon_{12} \rangle \end{Bmatrix} - \begin{Bmatrix} \alpha_1^* \Delta T \\ \alpha_2^* \Delta T \\ \alpha_3^* \Delta T \\ 0 \\ 0 \\ 0 \end{Bmatrix} \quad (3.9)$$

The brackets denote the volume average, $\langle \bullet \rangle = \frac{1}{V} \int \bullet dV$, where V is the volume of representative volume element. The effective thermal-elastic properties are calculated by applying a specified average strain or unit temperature for each direction (with all other strains set to zero) [28]. For example, if $\langle \varepsilon_{11} \rangle$ for one of the independent boundary condition equations is specified and all other average strains, and ΔT are set to zero, then equation (3.9) yields

$$\begin{Bmatrix} \langle \sigma_{11} \rangle \\ \langle \sigma_{22} \rangle \\ \langle \sigma_{33} \rangle \\ \langle \sigma_{23} \rangle \\ \langle \sigma_{13} \rangle \\ \langle \sigma_{12} \rangle \end{Bmatrix} = \begin{pmatrix} C_{11}^* & C_{12}^* & C_{12}^* & 0 & 0 & 0 \\ C_{12}^* & C_{22}^* & C_{23}^* & 0 & 0 & 0 \\ C_{12}^* & C_{23}^* & C_{22}^* & 0 & 0 & 0 \\ 0 & 0 & 0 & \frac{C_{22}^* - C_{23}^*}{2} & 0 & 0 \\ 0 & 0 & 0 & 0 & C_{66}^* & 0 \\ 0 & 0 & 0 & 0 & 0 & C_{66}^* \end{pmatrix} \begin{Bmatrix} \langle \varepsilon_{11} \rangle \\ 0 \\ 0 \\ 0 \\ 0 \\ 0 \end{Bmatrix} \quad (3.10)$$

If $\langle \varepsilon_1 \rangle$ is a unit strain, the following can be obtained,

$$C_{11}^* = \langle \sigma_{11} \rangle, \quad C_{12}^* = \langle \sigma_{22} \rangle, \quad C_{12}^* = \langle \sigma_{33} \rangle \quad (3.11)$$

Using this method, the following 6×6 stiffness matrix can be obtained.

$$\begin{pmatrix} \langle \sigma_{11} \rangle & \langle \sigma_{11} \rangle \\ \langle \sigma_{22} \rangle & \langle \sigma_{22} \rangle \\ \langle \sigma_{33} \rangle & \langle \sigma_{33} \rangle \\ \langle \sigma_{23} \rangle & \dots & \langle \sigma_{23} \rangle \\ \langle \sigma_{13} \rangle & \langle \sigma_{13} \rangle \\ \langle \sigma_{12} \rangle & \langle \sigma_{12} \rangle \end{pmatrix}^{6 \times 6} = \begin{pmatrix} C_{11}^* & C_{12}^* & C_{12}^* & 0 & 0 & 0 \\ C_{12}^* & C_{22}^* & C_{23}^* & 0 & 0 & 0 \\ C_{12}^* & C_{23}^* & C_{22}^* & 0 & 0 & 0 \\ 0 & 0 & 0 & \frac{C_{22}^* - C_{23}^*}{2} & 0 & 0 \\ 0 & 0 & 0 & 0 & C_{66}^* & 0 \\ 0 & 0 & 0 & 0 & 0 & C_{66}^* \end{pmatrix} \begin{pmatrix} \langle \varepsilon_{11} \rangle & 0 \\ 0 & 0 \\ 0 & 0 \\ 0 & \dots & 0 \\ 0 & 0 \\ 0 & \langle \varepsilon_{12} \rangle \end{pmatrix}^{6 \times 6} \quad (3.12)$$

From equation (3.12), the effective stiffness matrix C_{ij}^* can be obtained, and the effective thermal-elastic properties can be calculated from its compliance matrix.

$$C_{ij}^{*-1} = S_{ij}^* \quad (3.13)$$

It can be expressed in terms of engineering constants.

$$\begin{pmatrix} S_{11}^* & S_{12}^* & S_{12}^* & 0 & 0 & 0 \\ S_{12}^* & S_{22}^* & S_{23}^* & 0 & 0 & 0 \\ S_{12}^* & S_{23}^* & S_{22}^* & 0 & 0 & 0 \\ 0 & 0 & 0 & S_{44}^* & 0 & 0 \\ 0 & 0 & 0 & 0 & S_{66}^* & 0 \\ 0 & 0 & 0 & 0 & 0 & S_{66}^* \end{pmatrix} = \begin{pmatrix} \frac{1}{E_1^*} & \frac{-\nu_{12}^*}{E_1^*} & \frac{-\nu_{12}^*}{E_1^*} & 0 & 0 & 0 \\ \frac{-\nu_{12}^*}{E_1^*} & \frac{1}{E_2^*} & \frac{-\nu_{23}^*}{E_2^*} & 0 & 0 & 0 \\ \frac{-\nu_{12}^*}{E_1^*} & \frac{-\nu_{23}^*}{E_2^*} & \frac{1}{E_2^*} & 0 & 0 & 0 \\ 0 & 0 & 0 & \frac{2(1+\nu_{23}^*)}{E_2^*} & 0 & 0 \\ 0 & 0 & 0 & 0 & \frac{1}{G_{12}^*} & 0 \\ 0 & 0 & 0 & 0 & 0 & \frac{1}{G_{12}^*} \end{pmatrix} \quad (3.14)$$

From the relationships, the effective elastic properties are obtained.

$$\begin{aligned} E_{11}^* &= \frac{1}{S_{11}^*}, & E_{22}^* &= \frac{1}{S_{22}^*} \\ \nu_{12}^* &= S_{12}^* * E_{11}^*, & \nu_{23}^* &= S_{23}^* * E_{22}^* \\ G_{23}^* &= \frac{1}{S_{44}^*}, & G_{12}^* &= \frac{1}{S_{66}^*} \end{aligned} \quad (3.15)$$

In order to obtain the effective CTE, a temperature difference is applied and the effective CTE can be obtained by dividing the average strains by the temperature difference. This can be expressed in the equation

$$\begin{pmatrix} \alpha_1^* \\ \alpha_2^* \\ \alpha_3^* \end{pmatrix} = \begin{pmatrix} \langle \varepsilon_{11} \rangle / \Delta T \\ \langle \varepsilon_{22} \rangle / \Delta T \\ \langle \varepsilon_{33} \rangle / \Delta T \end{pmatrix} \quad (3.16)$$

where α_i^* are the effective coefficients of thermal expansion, $\langle \varepsilon_{kl} \rangle$ are the volume averaged strains, and ΔT is the temperature difference.

The finite element meshes, consisting of 20 node solid elements, are generated by using ANSYS and the stress analysis is conducted with a in-house program called ALPHA to solve the field equations for periodic unit cells.

Table 3.1 shows the effective thermal-elastic properties for perfect square and hexagonal unit cells.

Table 3.1. The effective thermal-elastic properties (60% fiber volume fraction)

	IM7 carbon fiber	977-2 epoxy	Effective Properties (square)	Effective Properties (hexagonal)
E_{11} (GPa)	263.7	3.32	159.6	159.5
E_{22}, E_{33} (GPa)	19.0	3.32	9.43	8.48
ν_{12}, ν_{13}	0.2	0.35	0.2526	0.2535
ν_{23}	0.35	0.35	0.382	0.439
G_{12}, G_{13} (GPa)	27.6	1.23	4.47	4.24
G_{23} (GPa)	6.89	1.23	2.57	2.926
$\alpha_{11} (\times 10^{-6} / C^{\circ})$	-0.4	57.6	0.159	0.15
$\alpha_{22}, \alpha_{33} (\times 10^{-6} / C^{\circ})$	5.63	57.6	30.83	31.3

3.3. Macro level analysis

For thermal loading, stresses are induced at ply level due to expansion or contraction and constraining effects of adjacent plies that prevent a free expansion or contraction. The thermally induced stresses in ply level are obtained using Classical Laminate Plate Theory [29]. For the inner and outer facesheets, two laminate composites are modeled. In order to represent a cryogenic environment, thermal loading of $-300^{\circ}C$ is applied to the laminate models and the ply stresses and strains of each layer in ply

level are calculated. For the laminated composite in Figure 3.5, a laminate X-Y-Z coordinate system is taken.

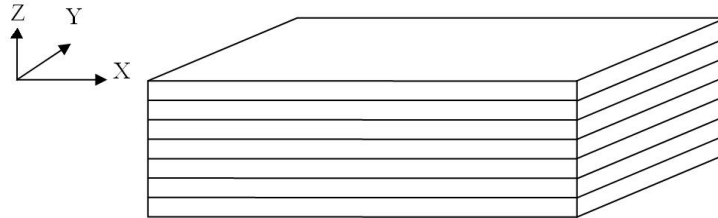
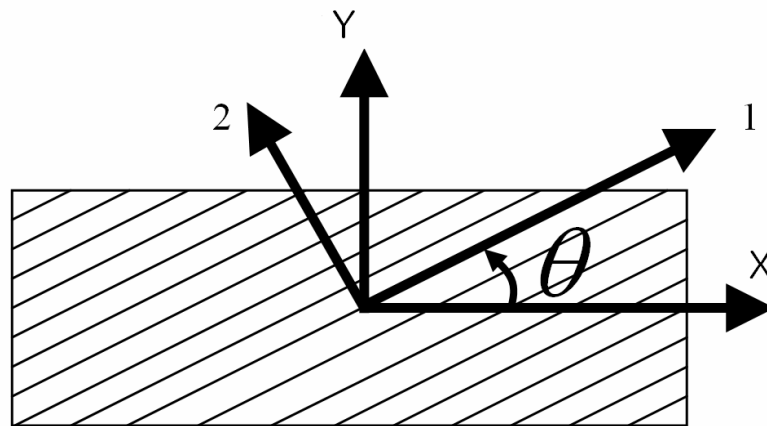


Figure 3.5. Laminate composite



1, 2: Material coordinate
X, Y: Laminate or arbitrary coordinate

Figure 3.6. Coordinate systems

As in Figure 3.6, two sets of coordinate systems are depicted. The 1-2 coordinate system corresponds to the material directions for a lamina, while the X-Y coordinates are arbitrary and related to the 1-2 coordinates through a rotation about the axis out of the plane of the figure. The angle θ is defined as the rotation angle between the arbitrary X-Y system and the 1-2 material system.

For the macro level analysis step, the above two laminated composites are constructed and the ply stresses and strains thermally induced in the laminates are obtained. They are transformed to the material coordinate system. Table 3.2 and 3.3 show the ply stresses and strains in the material coordinate system for each layer of outer face sheet and inner face sheet. For the lamina properties, perfect hexagonal unit cell is used in these tables.

Table 3.2. The ply stresses and strains of each layer of **inner facesheet** in the material coordinate system.

Ply	σ_1 (MPa)	σ_2 (MPa)	σ_{12} (MPa)	ε_1	ε_2	ε_{12}
65°	-52.2	71.5	1.98	-0.000486	-0.000877	0.0004665
0°	-131.2	74.7	0	-0.000986	-0.000377	0
-65°	-52.2	71.5	-1.98	-0.000486	-0.000877	-0.000467
90°	-35	70.8	0	-0.000377	-0.000986	0
-65°	-52.2	71.5	-1.98	-0.000486	-0.000877	-0.000467
0°	-131.2	74.7	0	-0.000986	-0.000377	0
65°	-52.2	71.5	1.98	-0.000486	-0.000877	0.0004665

Table 3.3. The ply stresses and strains of each layer of **outer facesheet** in the material coordinate system.

Ply	σ_1 (MPa)	σ_2 (MPa)	σ_{12} (MPa)	ε_1	ε_2	ε_{12}
45°	-83.3	72.7	2.6	-0.000683	-0.000683	0.0006055
90°	-35.5	70.8	0	-0.00038	-0.000986	0
90°	-35.5	70.8	0	-0.00038	-0.000986	0
90°	-35.5	70.8	0	-0.00038	-0.000986	0
-45°	-83.3	72.7	-2.6	-0.000683	-0.000683	-0.000606
0°	-131.1	74.6	0	-0.000986	-0.00038	0
0°	-131.1	74.6	0	-0.000986	-0.00038	0
0°	-131.1	74.6	0	-0.000986	-0.00038	0
-45°	-83.3	72.7	-2.6	-0.000683	-0.000683	-0.000606
90°	-35.5	70.8	0	-0.00038	-0.000986	0
90°	-35.5	70.8	0	-0.00038	-0.000986	0
90°	-35.5	70.8	0	-0.00038	-0.000986	0
45°	-83.3	72.7	2.6	-0.000683	-0.000683	0.0006055

1: fiber direction

2: direction perpendicular to fibers

The $\pm 65^\circ$ layers of inner facesheet and $\pm 45^\circ$ layers of outer facesheet have in-plane shear stresses, but the magnitudes are so small that interfacial stresses caused by the in-plane shear stresses can be neglected. Since 0° layers of both laminate composites have the maximum ply stresses σ_1 , and σ_2 , these 0° layers might have the highest possibility of macro level and micro level failure. These amounts of ply stresses of 0° layers are applied to the unit cell with thermal loading to investigate the effect of ply level stresses on interfacial stress fields. For this work, no extra mechanical load is considered. Therefore only the effect of thermal loading on interfacial failure between fiber and matrix will be studied.

3.4. Interfacial stress state analysis

After the effective thermal-elastic properties and macro level ply stresses and strains are obtained, one more micro level analysis is conducted using FEM. The ply stresses and thermal loading are applied to the unit cells, and the interfacial stress components are obtained in Cartesian coordinate system. These stresses are transformed to the cylindrical coordinate system to form the radial, shear, and tangential stresses. As in Figure 3.7, two sets of coordinate systems are depicted. The transformation equation is as follows,

$$\{\sigma\}^{cylindrical} = \{T\}\{\sigma\}^{Cartesian} \{T\}^T \quad (3.17)$$

The transformation tensor is defined as the followings

$$\{T\} = \begin{bmatrix} 1 & 0 & 0 \\ 0 & \cos \theta & \sin \theta \\ 0 & -\sin \theta & \cos \theta \end{bmatrix} \quad (3.18)$$

From the above relation, the interfacial stresses in cylindrical coordinate system can be obtained as following,

$$\begin{bmatrix} \sigma_{zz} & \sigma_{\theta z} & \sigma_{rz} \\ \sigma_{\theta z} & \sigma_{\theta\theta} & \sigma_{r\theta} \\ \sigma_{rz} & \sigma_{r\theta} & \sigma_{rr} \end{bmatrix} = \begin{bmatrix} 1 & 0 & 0 \\ 0 & \cos \theta & \sin \theta \\ 0 & -\sin \theta & \cos \theta \end{bmatrix} \begin{bmatrix} \sigma_{11} & \sigma_{12} & \sigma_{13} \\ \sigma_{12} & \sigma_{22} & \sigma_{23} \\ \sigma_{13} & \sigma_{23} & \sigma_{33} \end{bmatrix} \begin{bmatrix} 1 & 0 & 0 \\ 0 & \cos \theta & -\sin \theta \\ 0 & \sin \theta & \cos \theta \end{bmatrix}^T \quad (3.19)$$

As a result,

$$\begin{aligned} \sigma_{rr} &= \sigma_{11} \cos^2 \theta + 2\sigma_{12} \sin \theta \cos \theta + \sigma_{13} \sin^2 \theta \\ \sigma_{r\theta} &= -\sigma_{11} \sin \theta \cos \theta + \sigma_{22} \sin \theta \cos \theta + \sigma_{12} (\cos^2 \theta - \sin^2 \theta) \\ \sigma_{\theta\theta} &= \sigma_{11} \sin^2 \theta - 2\sigma_{12} \sin \theta \cos \theta + \sigma_{22} \cos^2 \theta \end{aligned} \quad (3.20)$$

The continuous stress components, σ_{rr} and $\sigma_{r\theta}$ are obtained by averaging values at Gauss points surrounding the given nodes in fiber and matrix parts, and the discontinuous stress component $\sigma_{\theta\theta}$ is obtained by averaging from Gauss points in the only matrix parts.

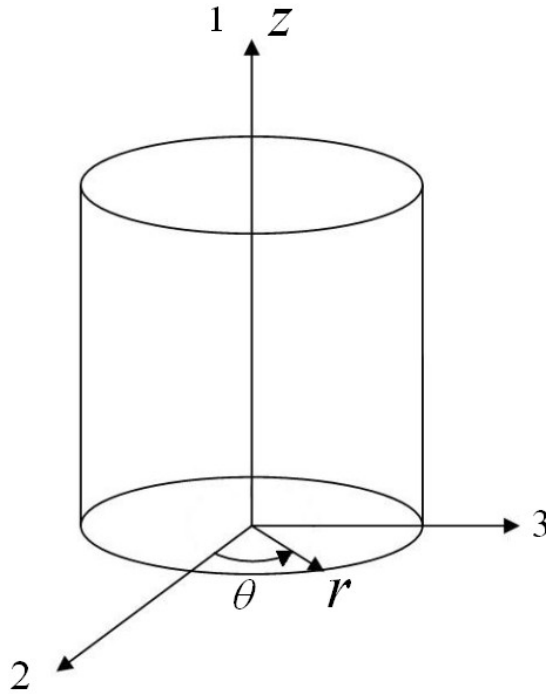


Figure 3.7. Cartesian and cylindrical coordinate systems

4. RESULTS AND DISCUSSION

4.1. Introduction

In this section, the effect of irregular fiber distribution and effect of the errors in assumed fiber transverse CTE values on thermally induced fiber/matrix interfacial stresses are presented.

Since interfacial stress states are affected by the location of neighboring fibers, if characteristics of the stress distribution patterns are known, the interfacial stresses of irregular fiber distribution can be predicted. As in Figure 4.1, typically two perfectly periodic arrangements have been used for studying interfacial stress analysis by many researchers. However, even though the two unit cells have the same volume fraction, their interfacial stresses have different patterns, because the fiber arrangements are different. For example, Figure 4.2 and 4.3 show the interfacial stress states for square and hexagonal unit cells under thermal loading of $-300^{\circ}C$ in a lamina. While the square array unit cell has the maximum radial stress at 45° point, the hexagonal unit cell has the maximum radial stress at 30° and 90° points. For two unit cell types, the locations of maximum stress values are not only different, but also the magnitudes of stresses are different. Like this, characteristics of interfacial stress patterns, which are affected by locations of neighboring fiber, will be studied from the perfect arrangement cases, and for extended studies, various large patterns, which can more represent irregularly distributed fiber arrangements as shown Figure 3.3, will be studied. Finally, the worst fiber arrangement case, which has the highest possibility of fiber/matrix debonding, will be suggested in this study.

4.2. Study of perfectly regular fiber arrangement cases

In this section, the interfacial stress states for perfect arrangements like square and hexagonal unit cells in Figure 4.1, and 4.2 are studied. As mentioned in the previous section 3.2.3, the effective thermal-elastic properties are obtained, and ply level ply stresses and strains are calculated by using CLPT for the given thermal loading condition. The interfacial stresses induced by thermal loading and indirect mechanical loading are presented. The complete solutions can be obtained by principle of superposition.

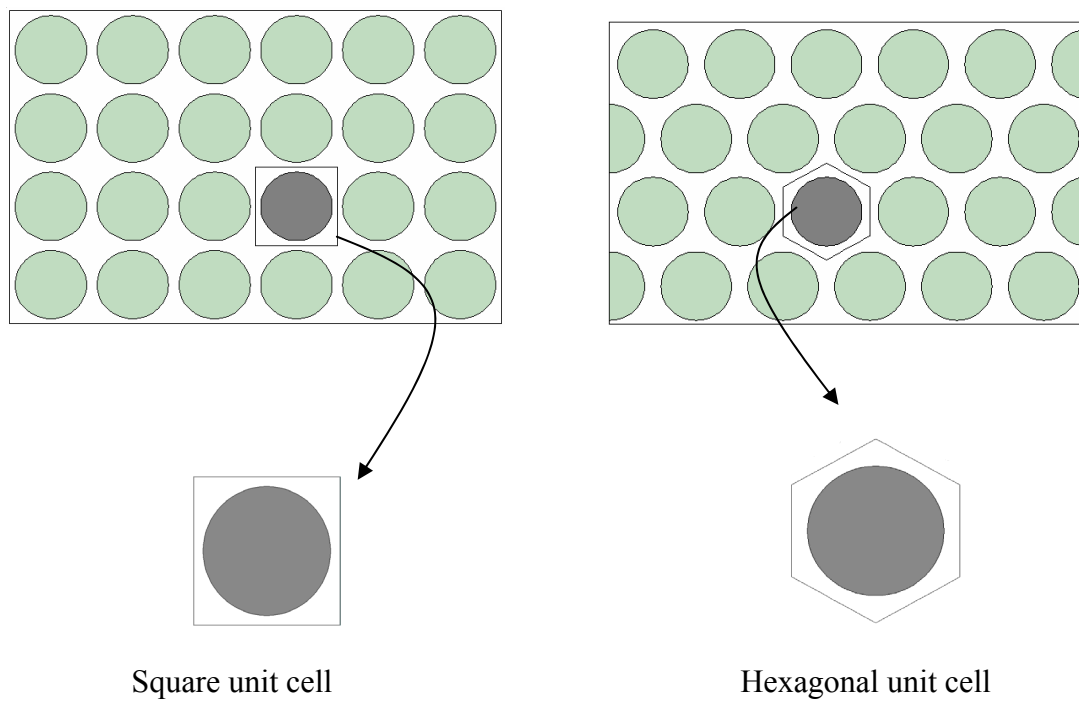


Figure 4.1. Perfect periodic arrangement unit cells

4.2.1. Interfacial stress states induced by thermal loading in a lamina

Thermal loading of -300°C is applied to the unit cells with the periodic boundary conditions for two perfect periodic unit cells. The interfacial radial, shear, and tangential stresses are plotted below in Figure 4.2, and 4.3. The fiber volume fractions for both cases are 60%.

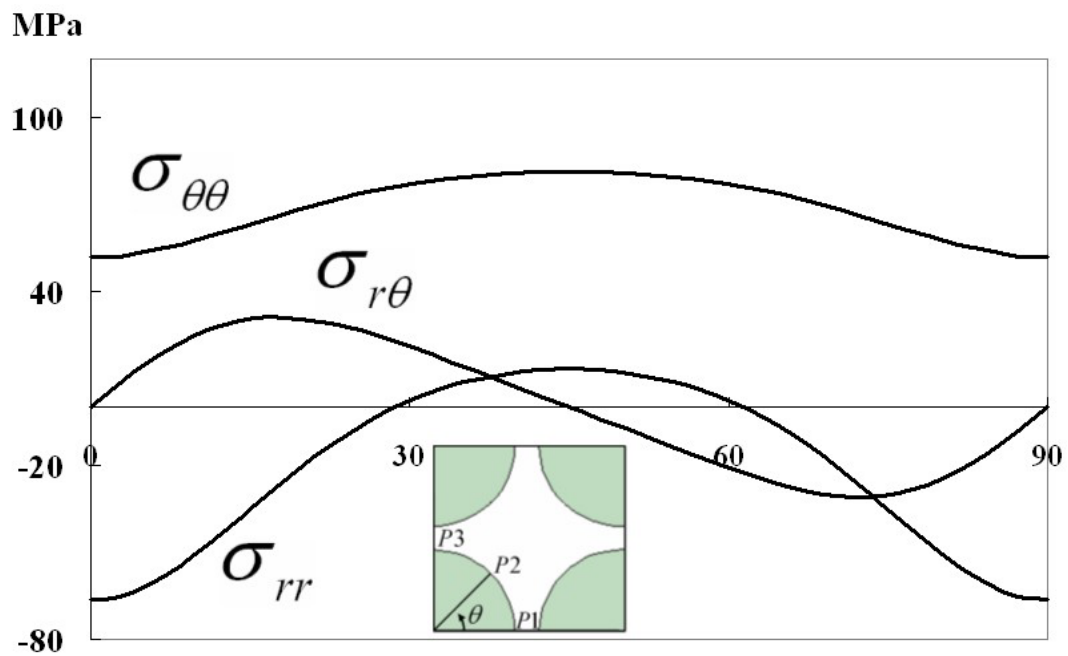


Figure 4.2. Interfacial stress states of square array induced by thermal loading in a lamina

Table 4.1. Interfacial stresses induced by thermal of square array unit cell

	Radial Stress	Tangential Stress
Max. Value	P2	P2
Min. Value	P1, P3	P1, P3

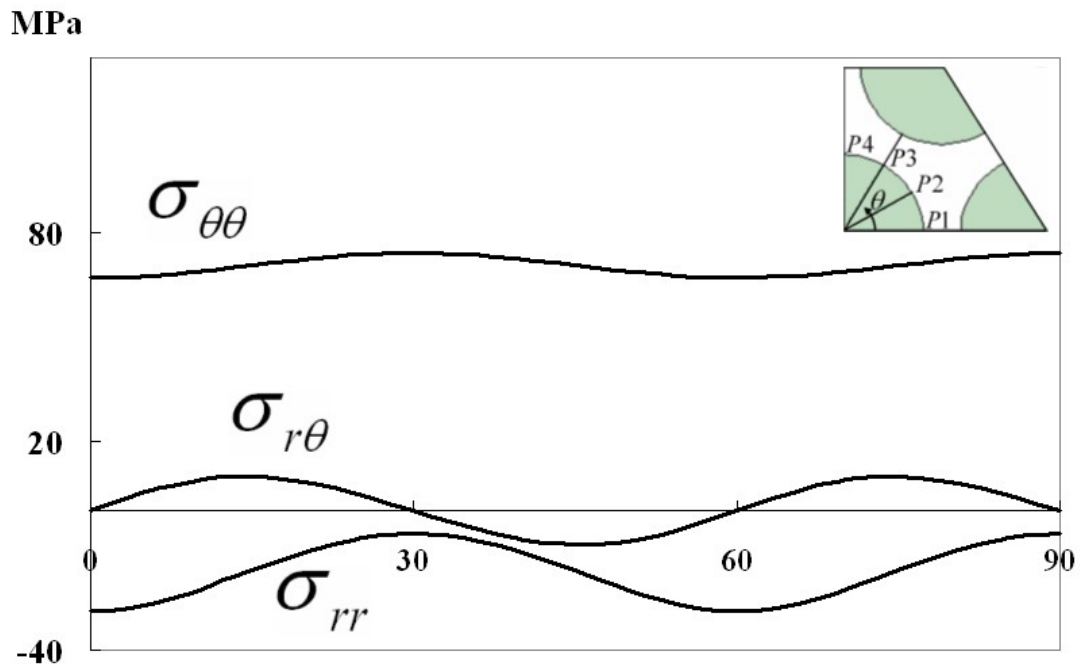


Figure 4.3. Interfacial stress states of hexagonal array induced by thermal loading in a lamina

Table 4.2. Interfacial stress states induced by thermal of hexagonal array unit cell

	Radial Stress	Tangential Stress
Max. Value	P2, P4	P2, P4
Min. Value	P1, P3	P1, P3

Radial stress

For hexagonal and square array cases, the maximum radial stresses induced by thermal loading occur at the points where the amounts of matrix are rich, as in Table 4.1, and 4.2. The points P2 in Figure 4.2 and P2 and P4 in Figure 4.3 are located near matrix-rich zones, and the radial stresses at the points have the maximum values. The intensity

of maximum radial stress depends on the amount of matrix-rich zone. For both cases, they have the same volume fraction, but their maximum radial stresses are different. While the hexagonal array has 6 neighboring fibers, the square array has 4 neighboring fibers (the diagonal fiber does not affect the reference fiber, because the distance is too far). Therefore the thermally induced stresses of the hexagonal unit cell are more distributed to the neighboring fibers than those of the square unit cell. In other words, matrix parts of hexagonal array are distributed more sparsely than those of square array. On the other hand, the matrix zones of square array are concentrated at 4 areas, while the matrix zones of hexagonal array are concentrated at 6 areas. For the hexagonal array case, the maximum radial stresses are compressive along the interface because of small matrix-rich zone, but for square array case, the maximum radial stresses become tensile because of large matrix-rich zone. It is concluded that the maximum radial stresses occur at the matrix-rich areas, and if there are enough matrix-rich zone near the fibers, the point near matrix-rich zones of the fiber has a tensile radial stress, and this tensile radial stresses will cause fiber/matrix debonding.

Shear stress: The shear stresses induced by thermal loading vanish at the line of symmetry for both cases. Also at the line of symmetry, the radial stresses become maximum and minimum. The maximum absolute values of shear stresses occur at the middle point between points where shear stresses become zero.

Tangential stress: The variations of tangential stresses induced by thermal loading are similar to those of radial stresses.

4.2.2 Interfacial stress states induced by ply stresses (indirect mechanical loading) in laminate

In this section, the effect of indirect mechanical loading is studied. For indirect mechanical loading, ply level ply stresses or strains of laminate composites, which are obtained in section 3.3, are applied to the unit cells. The ply level stresses of 0° layer, that has the maximum ply stresses, are considered for this study [Table 3.2, and 3.3].

For the two different periodic unit cells, the interfacial stress states show similar patterns under indirect mechanical loading, as shown in Figure 4.4, and 4.5, while the cases of only thermal loading resulted in different interfacial stress states for the two unit cells. It indicates that the interfacial stress pattern for indirect mechanical loading is not as sensitive to the fiber distributions as the thermal loading cases. Table 4.3 and 4.4 show the locations where have the maximum and minimum values for two models.

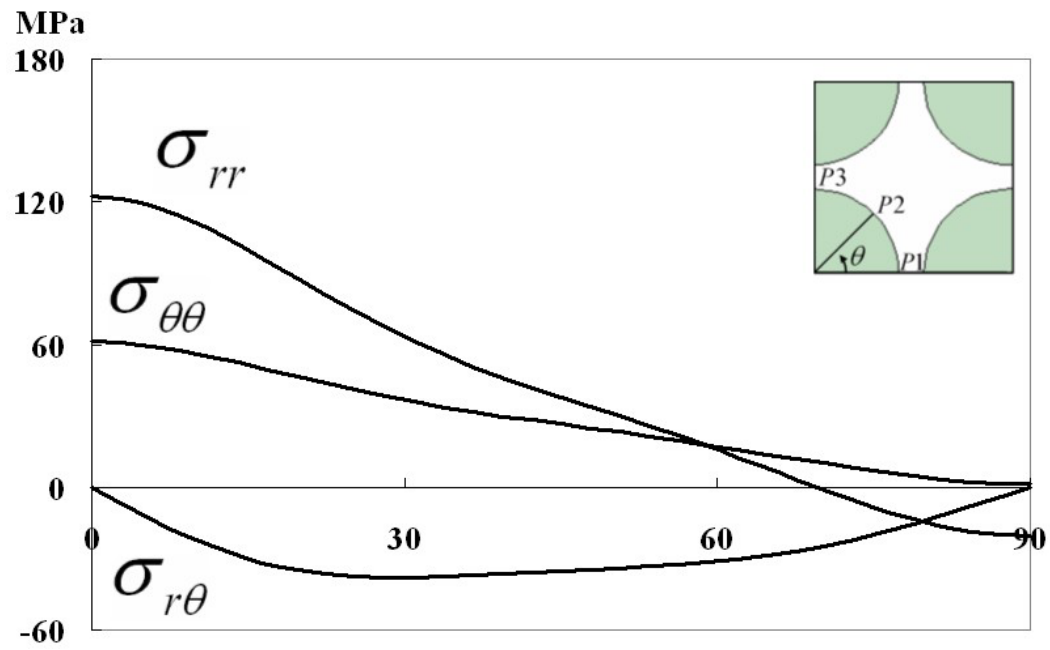


Figure 4.4. Interfacial stress states induced by indirect mechanical loadings of square unit cell

Table 4.3. Interfacial stresses induced by ply stresses of square array unit cell

	Radial Stress	Tangential Stress
Max. Value	P1	P1
Min. Value	P3	P3

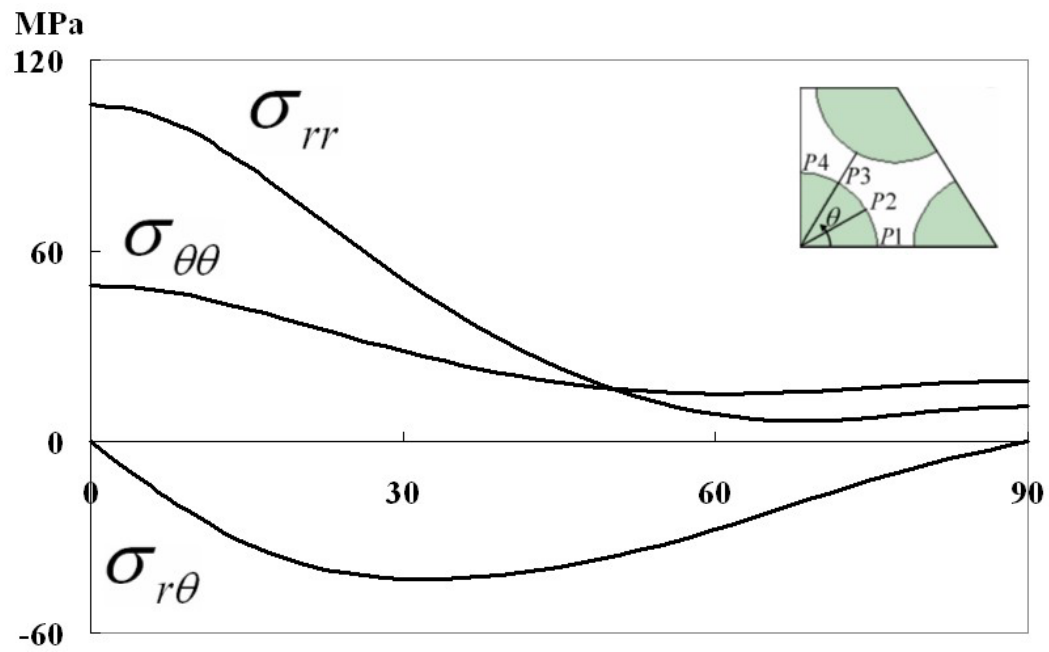


Figure 4.5. Interfacial stress states induced by indirect mechanical loadings of hexagonal unit cell

Table 4.4. Interfacial stresses induced by ply stresses of hexagonal array unit cell

	Radial Stress	Tangential Stress
Max. Value	P1	P1
Min. Value	P3	P3

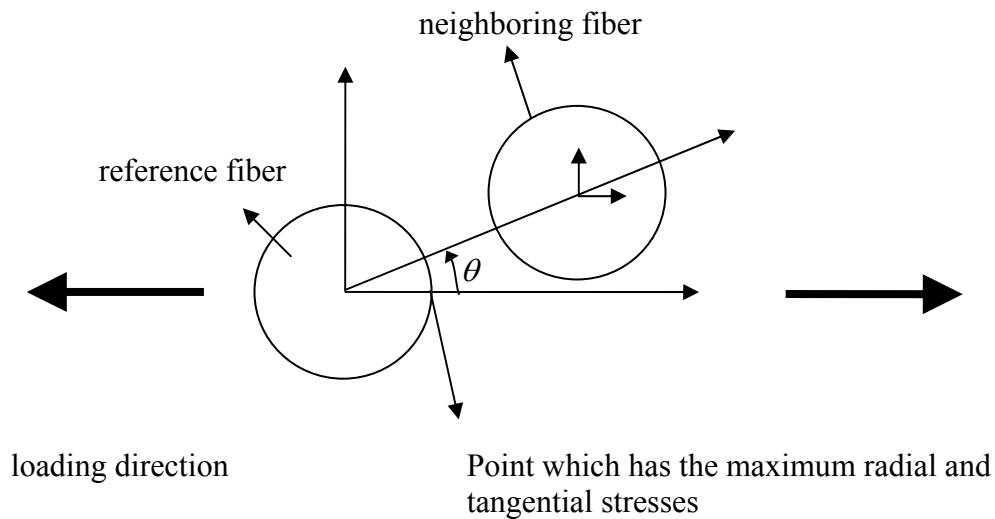


Figure 4.6. The relationship between interfacial stresses and loading direction

Radial stress: The intensity of the maximum radial and tangential stresses induced by transverse loading depends on the distance to neighboring fibers and the angle between the loading direction and the lines connecting to reference fiber with the neighboring fibers, as shown in Figure 4.6. When the angle is small (0° means parallel neighboring fiber case), the radial and tangential stresses of the point are increased, i.e. when the neighboring fiber is located in the same direction with the transverse loading, the 0° point of the reference fiber has the maximum radial and tangential stresses. At the 0° points, both unit cells have about 120MPa tensile radial stresses. When the magnitudes of the interfacial stresses and interfacial strength are considered, fiber/matrix debonding can be caused for the periodic unit cell cases, based on the maximum stress criterion.

Shear stress: The shear stresses induced by transverse loading vanish at 0° and 90° , and they have the maximum absolute values near 30° . Since the shear stress states for both fiber arrangement cases are almost identical, effect of fiber distributions on interfacial shear stresses are small.

Tangential stress: The tendency of tangential stresses induced by thermal loading is similar to those of radial stresses.

4.2.3 Interfacial stress states induced by combined loadings

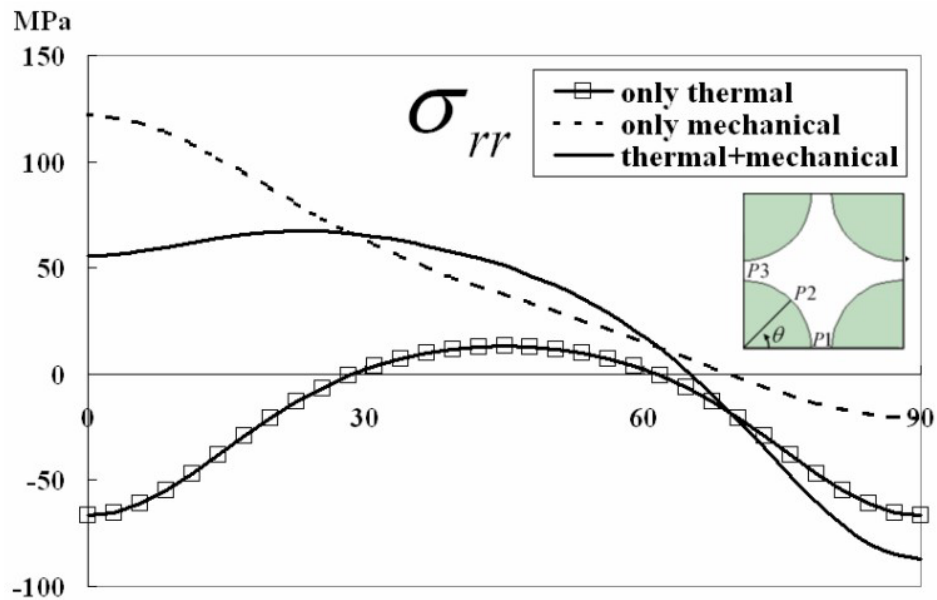
The complete interfacial stresses for the combined loading conditions can be obtained by superposition of the two independent loading conditions. In order to compare the difference between only thermal, only indirect mechanical, and complete loading cases, the following results are presented in Figure 4.7, and 4.8.

Radial stress: Figure 4.7 a) and 4.8 a) show the radial stress states for square and hexagonal fiber arrays. While the radial stress induced by only the thermal loadings are partially tensile (square case) or compressive (hexagonal case), the radial stress induced by only the indirect mechanical loadings are mostly high tensile and with higher magnitude throughout the area. For both cases, the interfaces between about 0° and 60° have high tensile radial stresses because of high tensile radial stresses induced by indirect mechanical loading. However, the interface of square array has lower radial stresses than the assumed interfacial strength $64MPa$. On the other hand, interface between 0° and 20° of hexagonal array has higher radial stresses than the assumed interfacial strength $64MPa$. Therefore, based on the maximum stress criterion, the

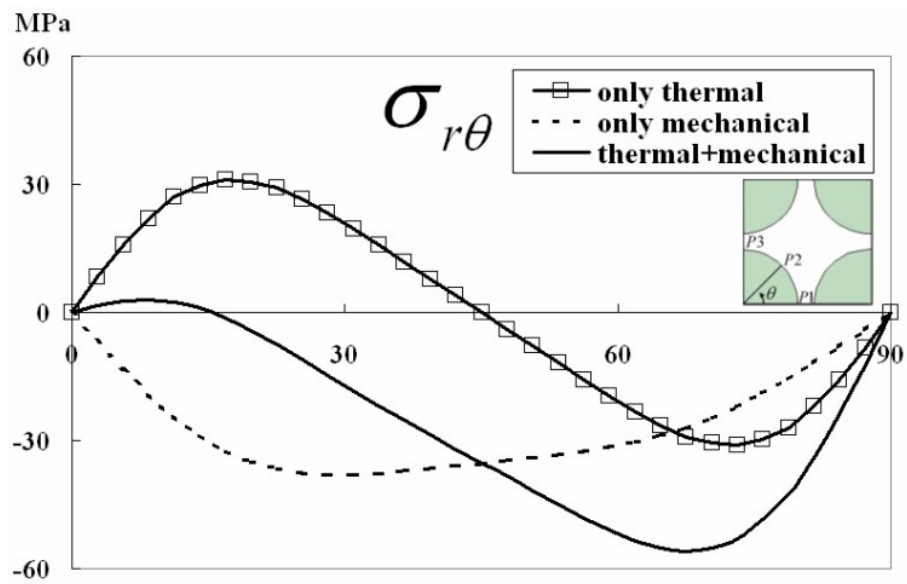
interfaces between 0° and 20° of hexagonal array have possibility of fiber/matrix debonding.

Shear stress: Figure 4.7 b) and 4.8 b) show the shear stress states. The absolute values of shear stress for combined loading condition occur near 70° in the square unit cell and 50° in the hexagonal unit cell. In some areas, the combined absolute values of shear stresses are decreased but in other areas, the values are higher because of superposition. The general tendency of combined shear stresses follows the mechanical loading, but the peak values and their locations are shifted because of the shear stresses caused by the thermal loading. If the interfacial shear strength is assumed as 33MPa , the square array will have possibility of torsional sliding mode between 40° and 80° , and the hexagonal array will have possibility of torsional sliding mode between 20° and 60° , based on the maximum criterion.

Tangential normal stress: While the effect of indirect mechanical loadings are dominant on the radial and shear stresses, the effect of thermal stress is more dominant on the tangential stresses than indirect mechanical loading. Figure 4.7 c) and 4.8 c) show the tangential stress states. Since the tangential stresses induced by thermal and indirect mechanical loadings are tensile, the superposition values have high tensile tangential stresses. Therefore, when the tensile strength of matrix is considered 77MPa , the square array will have matrix cracks between 0° and 60° , and the hexagonal array will have matrix cracks between 0° and 45° , based on the maximum stress criterion.

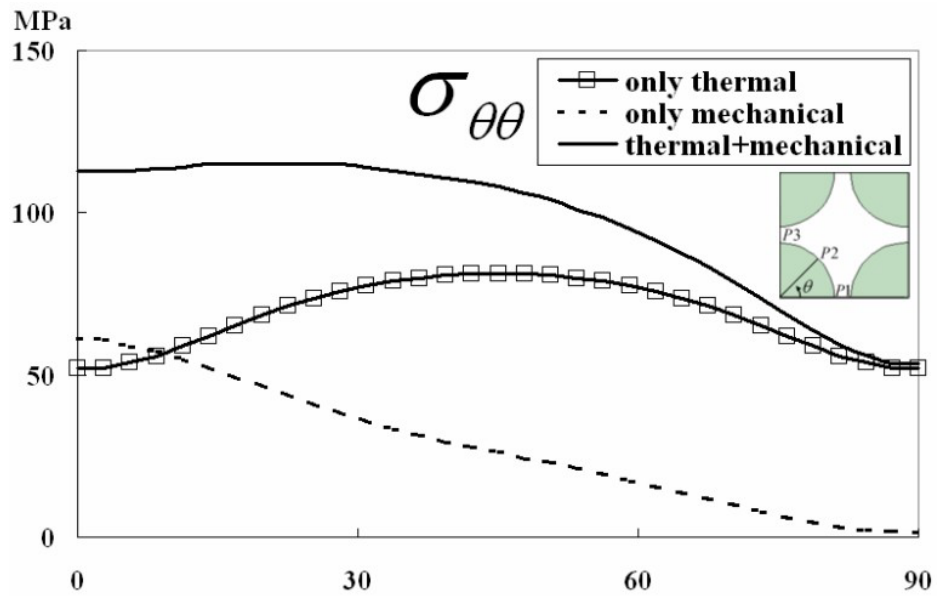


a) Radial stresses



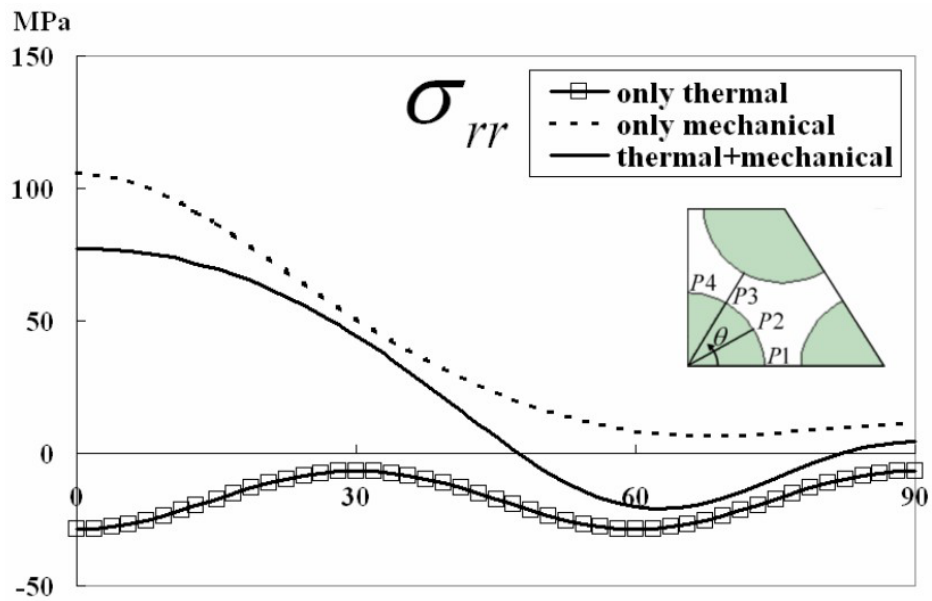
b) Shear stresses

Figure 4.7. Interfacial stress states induced by combined loadings of square unit cell



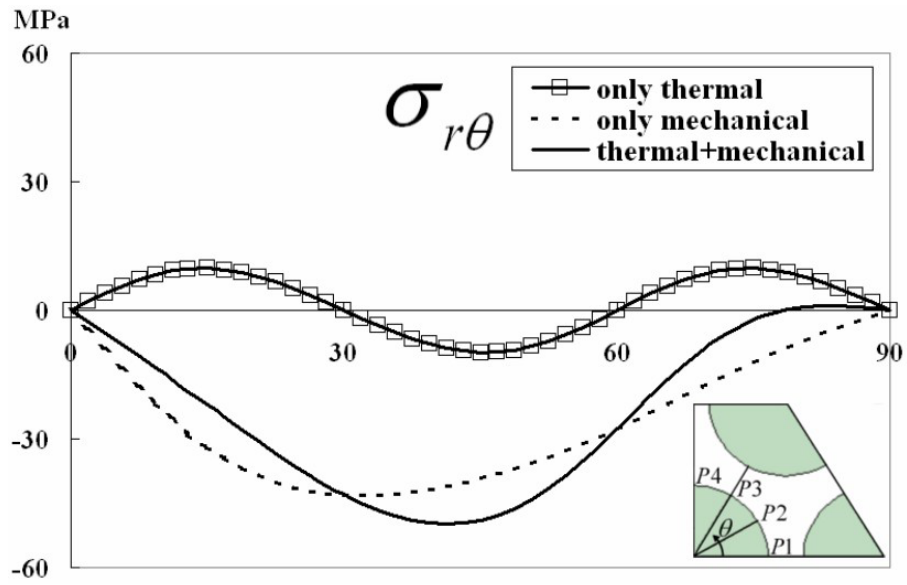
c) Tangential stresses

Figure 4.7. Continued

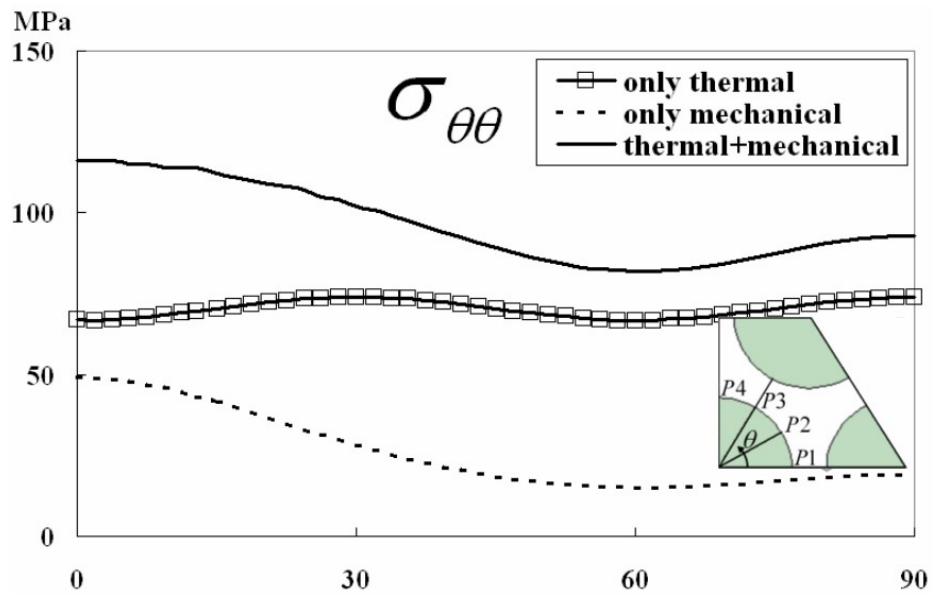


a) Radial stresses

Figure 4.8. Interfacial stress states induced by combined loadings of hexagonal unit cell



b) Shear stresses

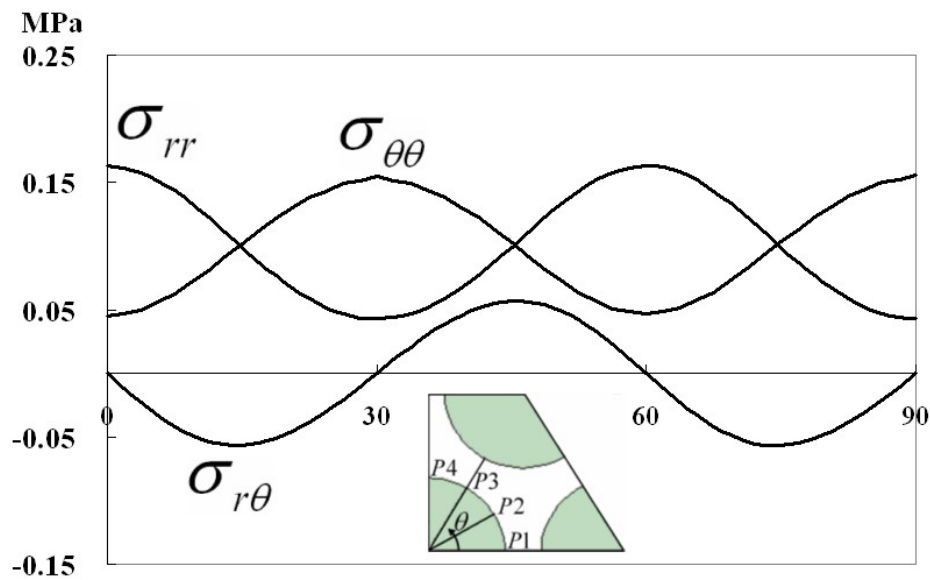


c) Tangential stresses

Figure 4.8. Continued

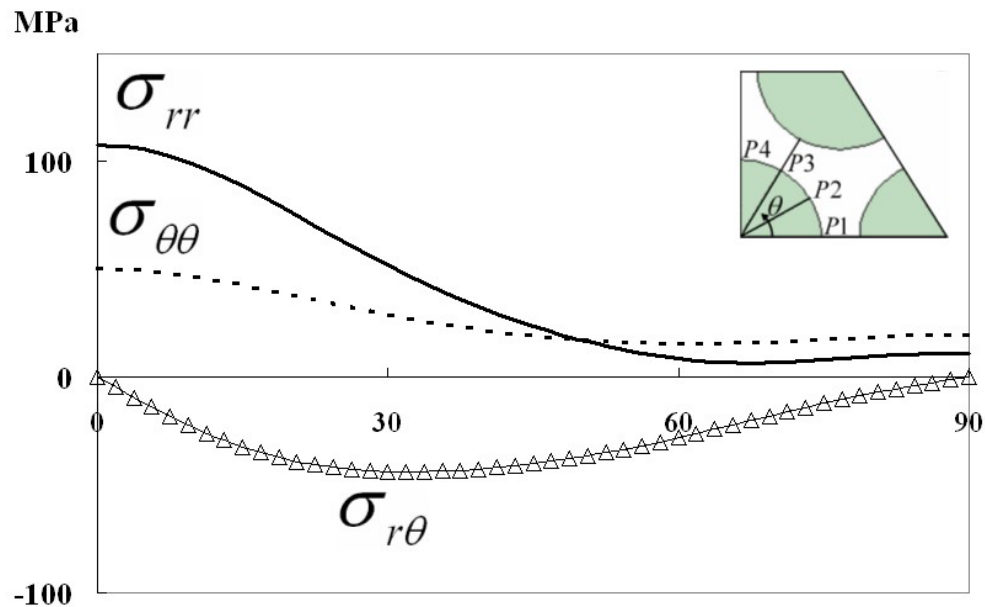
4.2.4 Effect of each component of ply stresses on the interfacial stresses

In section 4.2.2, the effect of ply stresses on interfacial stress states was studied. For the work, the longitudinal ply stress σ_1 and transverse ply stress σ_2 obtained in section 3.2.2 were applied to the unit cells. In this section, the ply stresses, σ_1 and σ_2 are applied to the hexagonal unit cell respectively to compare the effect of each ply stress component on interfacial stresses. The results are presented in Figure 4.9. The results show that the interfacial stresses induced by only longitudinal ply stress σ_1 are very small compared to those induced by only σ_2 . Therefore, the effect of transverse ply stress σ_2 is more significant than those of longitudinal ply stress σ_1 on the interfacial stress states.



a) Interfacial stresses due to ply stress σ_1

Figure 4.9. Effect of ply stresses σ_1 and σ_2 on the interfacial stress states



b) Interfacial stresses due to ply stress σ_2

Figure 4.9. Continued

4.3. Study of large pattern arrangement cases

4.3.1. Introduction

In section 4.2, the interfacial stress states of perfectly regular fiber arrangement like square and hexagonal arrays have been studied, and from the results, it was found that interfacial stresses of fibers located near matrix rich zones increased for thermal loading, and if laminate effect is added to interfacial stresses, the interfacial stresses are increased very highly. In this section, our interesting will be expended for large pattern

cases which can represent more irregularly distributed fiber arrangement described in section 3.2.1 to study the effect of matrix-rich zones.

4.3.2. Effect of matrix-rich zones on interfacial stress fields

In order to investigate the effect of matrix-rich zones on interfacial stress fields, the following unit cell is constructed in Figure 4.10. For this unit cell, one fiber is missed regularly. Thermal loading of -300°C is applied to the unit cell, and interfacial stresses of the fiber, which has the coordinate system, are obtained. Figure 4.11 shows the difference of interfacial stress fields between perfectly regular hexagonal case and one fiber missed case in the center.

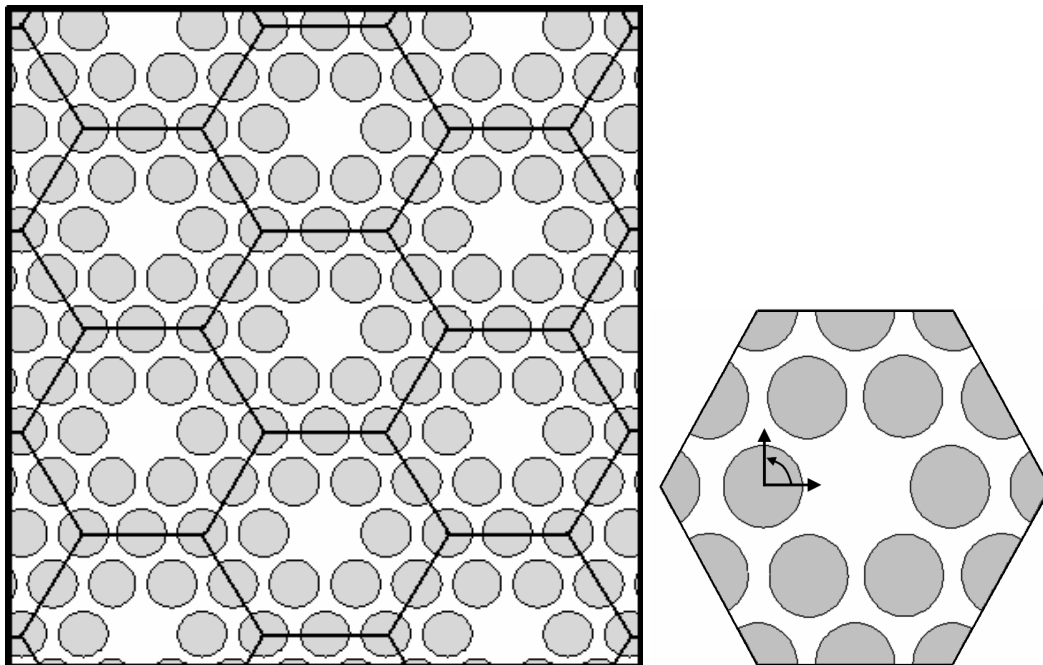
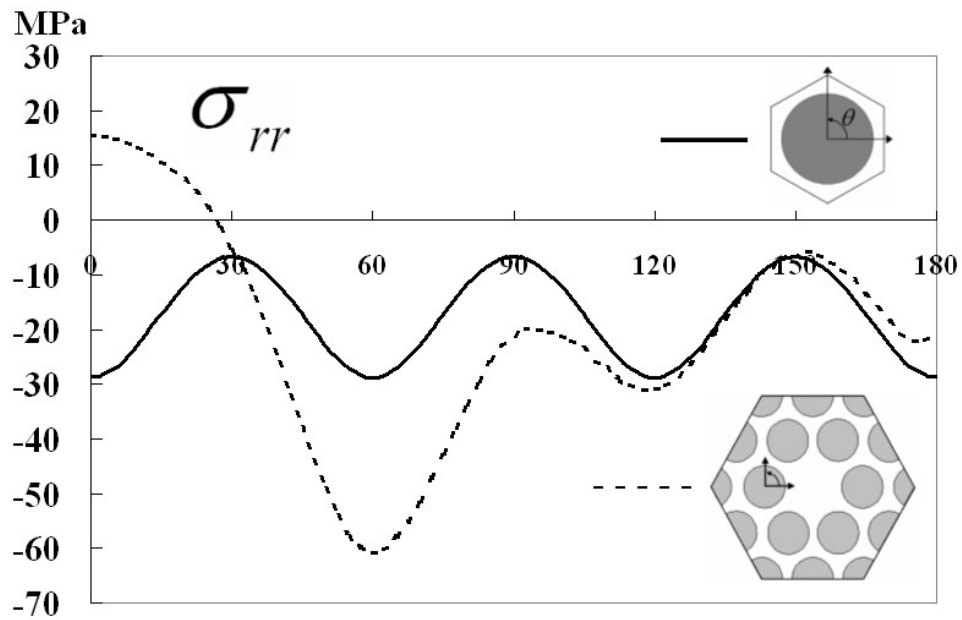
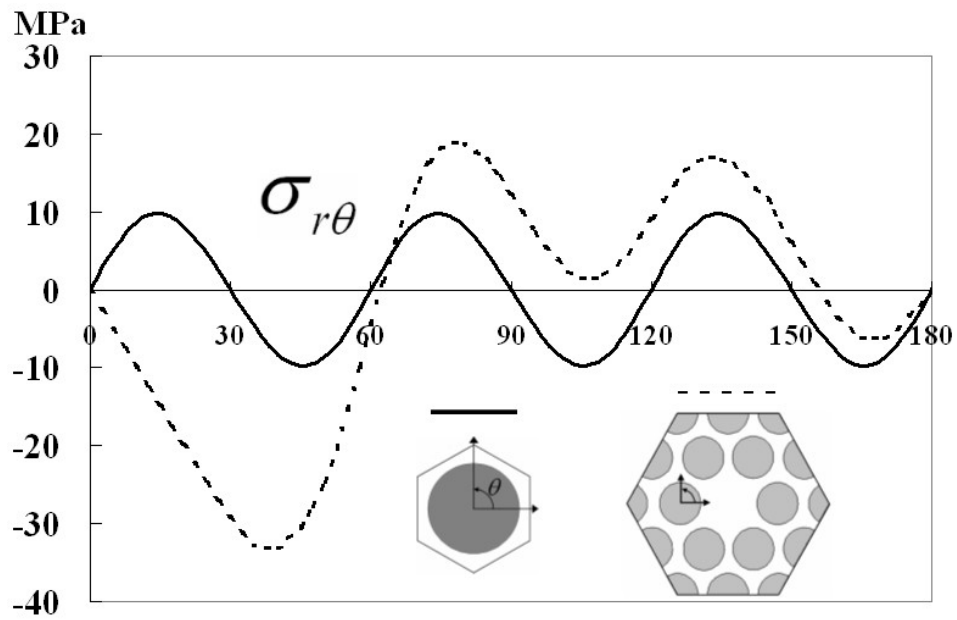


Figure 4.10. Unit cell having matrix-rich zone in center (one fiber missed case)

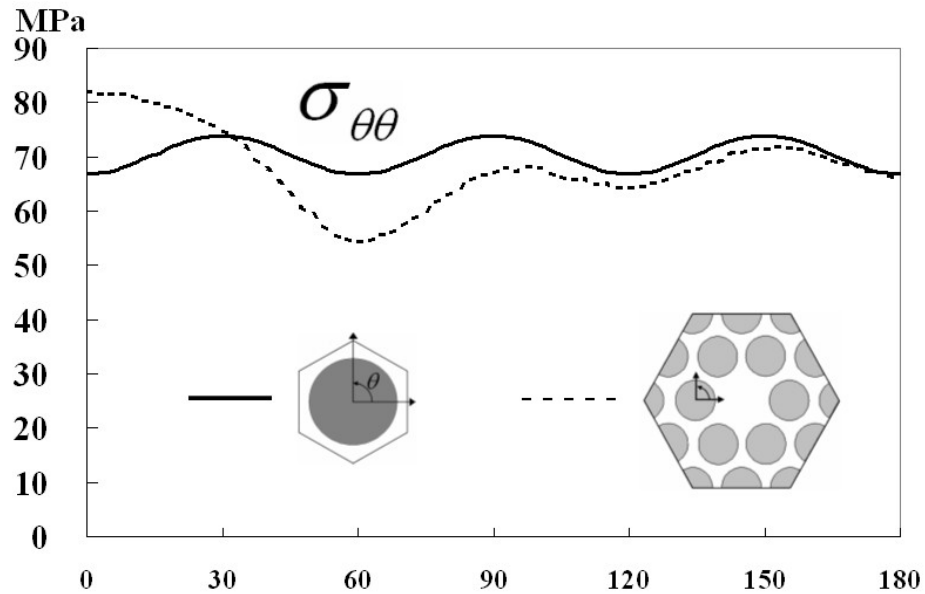


a) Radial stresses



b) Shear stresses

Figure 4.11. Interfacial stress fields of perfectly regular unit cell and one fiber missed unit cell



c) Tangential stresses

Figure 4.11. Continued

As in Figure 4.10 a), the unit cell, which is missing one fiber, has tensile radial stresses between 0° and 25° , while the radial stress of perfect hexagonal unit cell is compressive through the all interface. It is considered that the matrix-rich zones cause the tensile radial stresses, and as a result, the radial stresses of the fiber near matrix-rich zone are increased. The radial stress is not only increased, but also the tangential and shear stresses are increased in some areas. If mechanical loadings are added to these increased interfacial stresses, fibers near matrix-rich zones will have more critical debonding possibility. Table 4.5 shows the amount of increased stress compared with hexagonal unit cell cases.

Table 4.5. Comparing one fiber missed cases with hexagonal case

	Hexagonal case	One fiber missed case
Radial	All compressive	Partially tensile from 0° to 25° (near matrix-rich zone)
Shear	Maximum $10MPa$	Maximum $40MPa$
Tangential	Maximum $70MPa$	Maximum $90MPa$ (near matrix-rich zone)

H. S. Choi et al. [8] in 2001 and W. Ding et al. [16] in 2002 obtained the interfacial stress fields of perfect hexagonal unit cell for cooling process and found that radial stresses are compressive induced at the interface, and insisted that these thermal stresses are beneficial to the transverse strength. These results can be right partially, if fibers can be distributed perfectly and regularly. However, perfectly distributed fiber arrangement can not be expected in real situation, and there is always the possibility of matrix-rich zones in real composite. From this study, it is concluded that if there is matrix-rich zones, thermally induced interfacial stresses of fibers located near matrix-rich zones will have tensile interfacial stresses and these tensile interfacial stresses are harmful to the transverse strength.

Figure 4.12 shows the interfacial stress states of hexagonal unit cell and one fiber missed unit cell, when the laminate effect is considered. Basically both of them show high tensile radial stresses in some interfaces, and these higher tensile radial stresses can cause fiber/matrix debonding in the interfaces. However, one fiber missed case has higher tensile stress in some interface, especially from 0° to 30° and from 150° to 180° . In addition, one fiber missed case has higher shear stresses than those of perfect hexagonal case. It is a notable result that a fiber located near matrix-rich zones will be

more likely to experience for fiber/matrix debonding or microcracks than fibers in a regularly distributed arrangement.

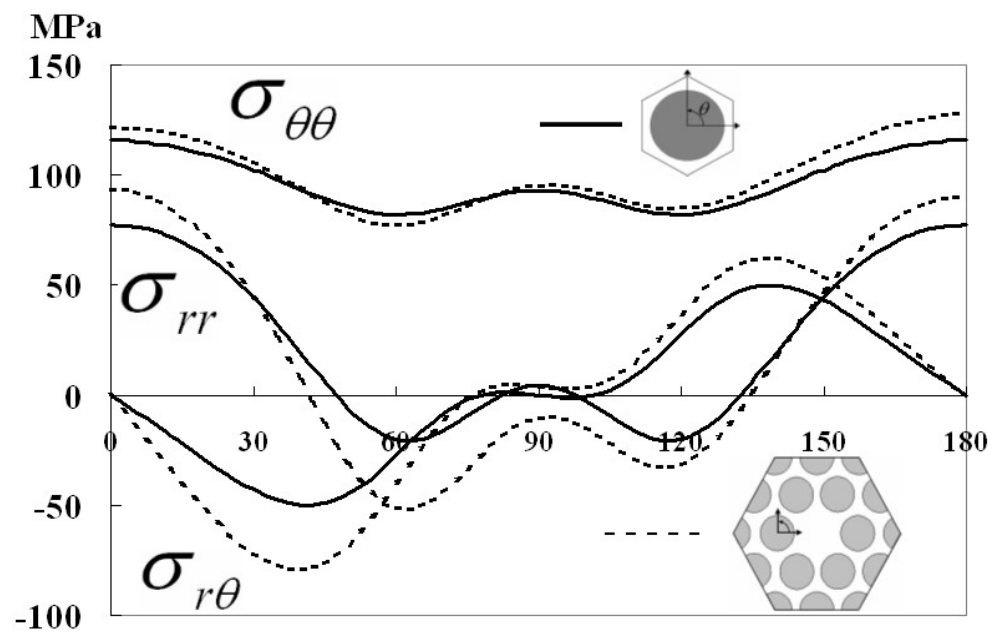
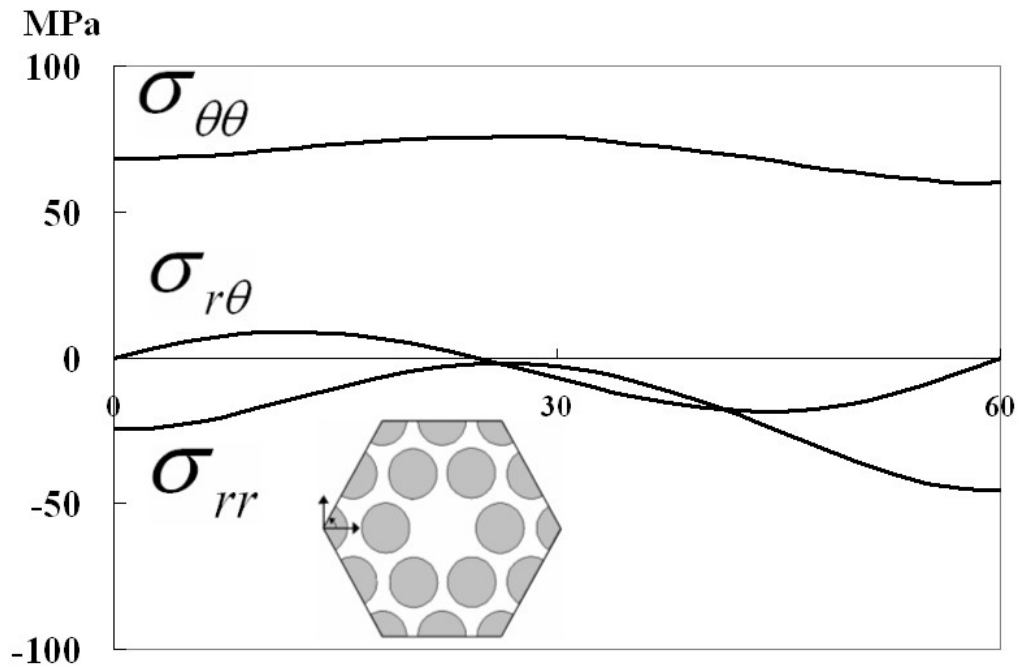


Figure 4.12. Interfacial stress states due to laminate effect of hexagonal and one fiber missed unit cell

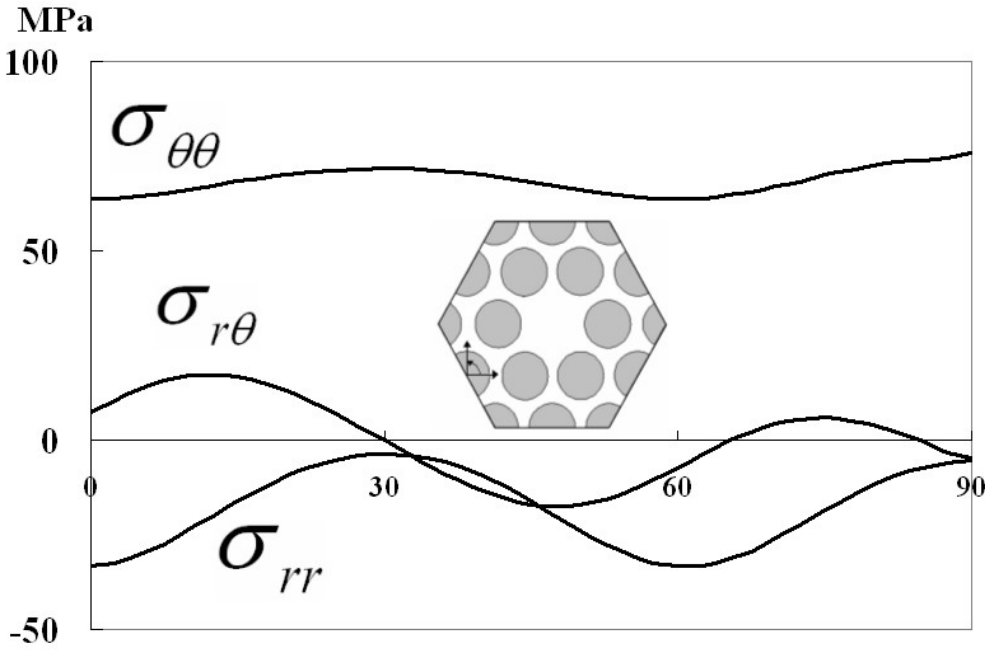
Since the large pattern unit cell in Figure 4.10 has other fibers located away from the matrix-rich zone, interfacial stresses of these fibers should be studied. Figure 4.13 shows the interfacial stress states of the other fibers. As shown in Figure 4.13, the fibers

away from the matrix-rich zone have lower interfacial stresses than the fibers located near the matrix-rich zone. Hence these fibers are less likely to debond.

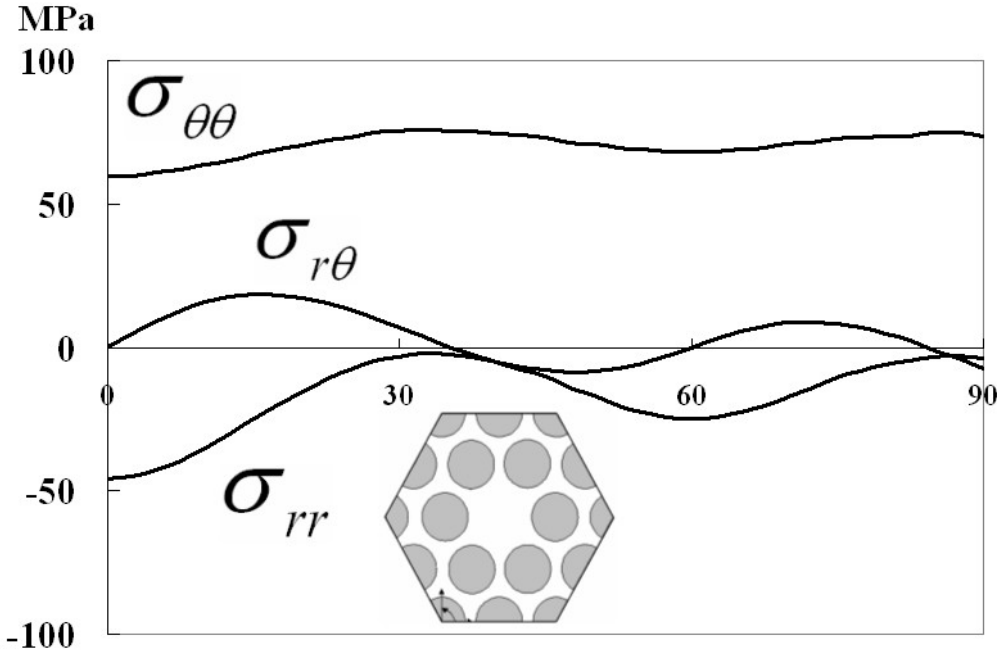


a) Outer fiber 1

Figure 4.13. Interfacial stress states of one fiber missed unit cell



b) Outer fiber 2

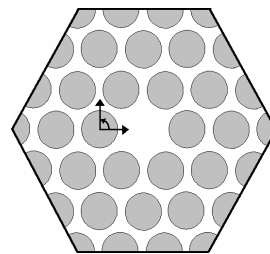
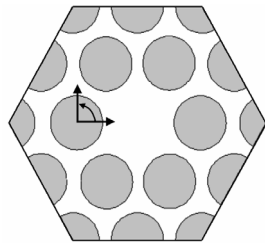
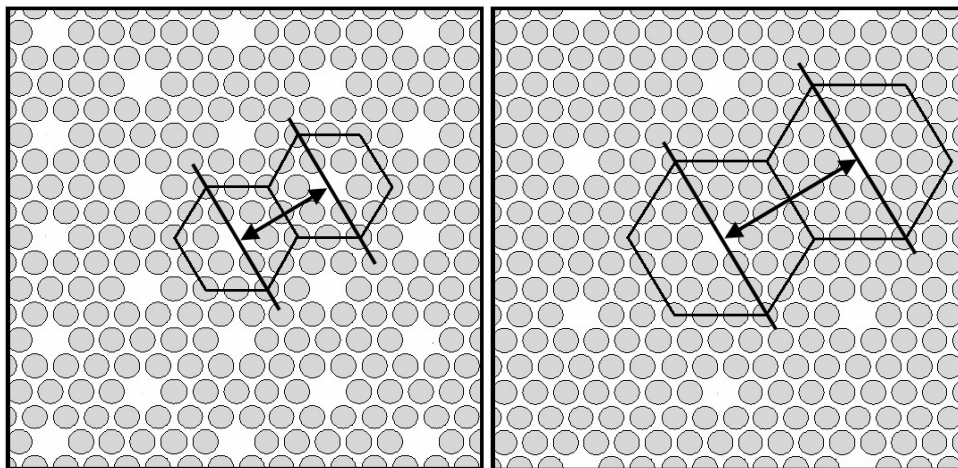


c) Outer fiber 3

Figure 4.13. Continued

4.3.3. Effect of spacing of matrix-rich zones on interfacial stress fields

In this section, the effect of size of matrix-rich zones on interfacial stress fields is studied. As in Figure 4.14, two kinds of fiber distribution patterns are assumed. Case (a) and (b) have the same amount of matrix pocket zone in the center of unit cells, and the matrix-rich zones are surrounded by fiber wall. The matrix-rich zones of case (b) are placed more sparsely than those of case (a). Thermal loadings of $-300^{\circ}C$ are applied to the both cases, and interfacial stresses for the reference fibers having coordinates are obtained. Since the reference fibers are located near at matrix-rich zones, the difference of their interfacial stresses will tell the effect of spacing of matrix-rich zones.



a) One fiber missed unit cell #1

b) One fiber missed unit cell #2

Figure 4.14. Unit cells that are missing one fiber in center

Figure 4.15 shows the difference of interfacial stress fields between two cases. As in Figure 4.15, there is not much difference for two cases. Therefore, it is concluded that the effect of spacing between matrix-rich zones on interfacial stresses is not significant.

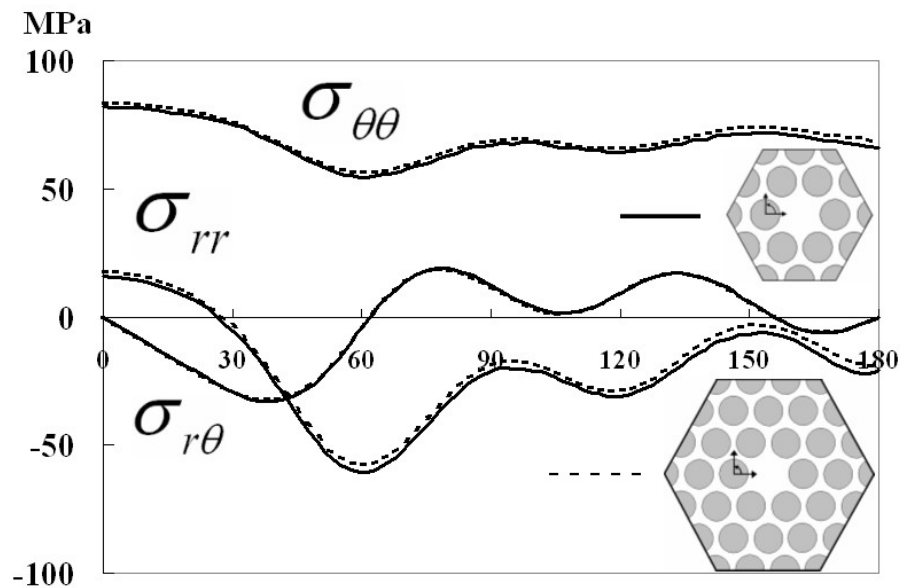
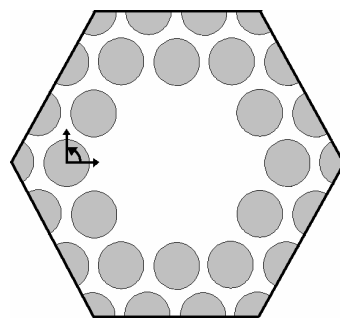
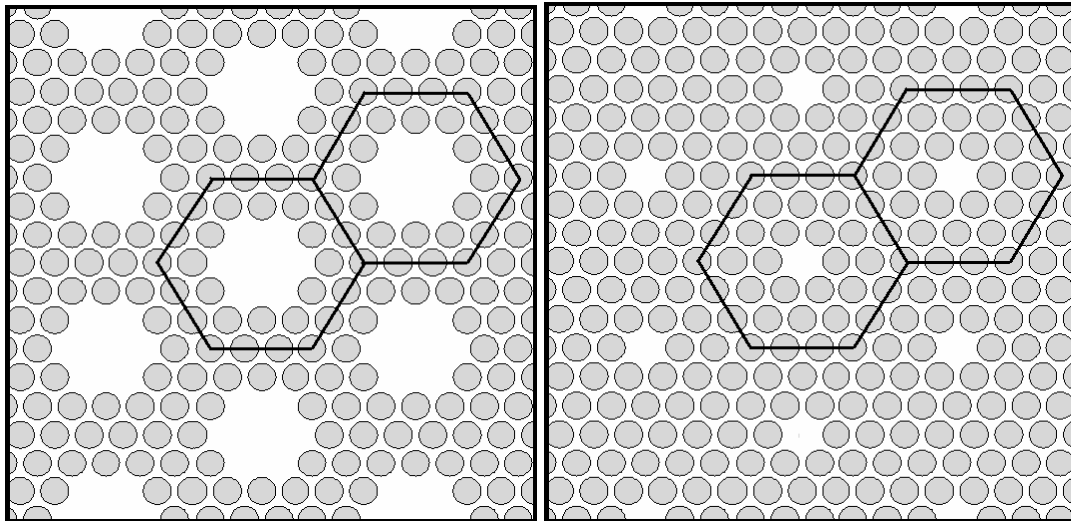


Figure 4.15. Interfacial stress state of one fiber missed unit cells

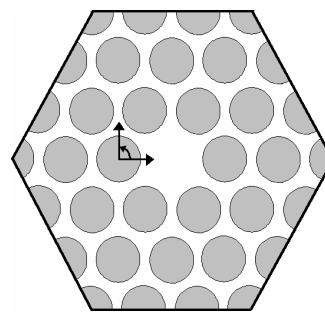
4.3.4. Effect of size of matrix-rich zones on interfacial stress fields

Figure 4.16 shows the unit cells have the same size, but have different size of matrix pockets. Since Figure 4.16 a) is missing 6 fibers in center, and Figure 4.16 b) is missing 1 fiber compared with perfect hexagonal unit cell, Figure 4.16 a) has larger

matrix pocket than that of Figure 4.16 b). Figure 4.17 shows the results for two unit cells under thermal loadings of -300°C .



a) 6 fibers missed unit cell



b) 1 fibers missed unit cell

Figure 4.16. Unit cells that are having different quantity of matrix

The interfacial stresses of the two fibers which have the coordinate systems in Figure 4.16a) and b) are compared, and the results are presented in Figure 4.17. As in Figure 4.17, the radial stresses of the fiber near matrix-rich zone (from 0° to 25°) of a)

shows values similar to those for b), but the other circumferential interface of a) between 25° and 180° shows lower radial stresses than those of b). It is likely that the larger amount of matrix pocket causes higher radial stresses for fibers located near the matrix pocket, but decreases radial stresses of the other circumferential interface of the fiber. For shear stress, the larger amount of matrix pocket of a) increase higher shear stresses than those of b). However, larger amount of matrix pocket decrease the tangential stresses.

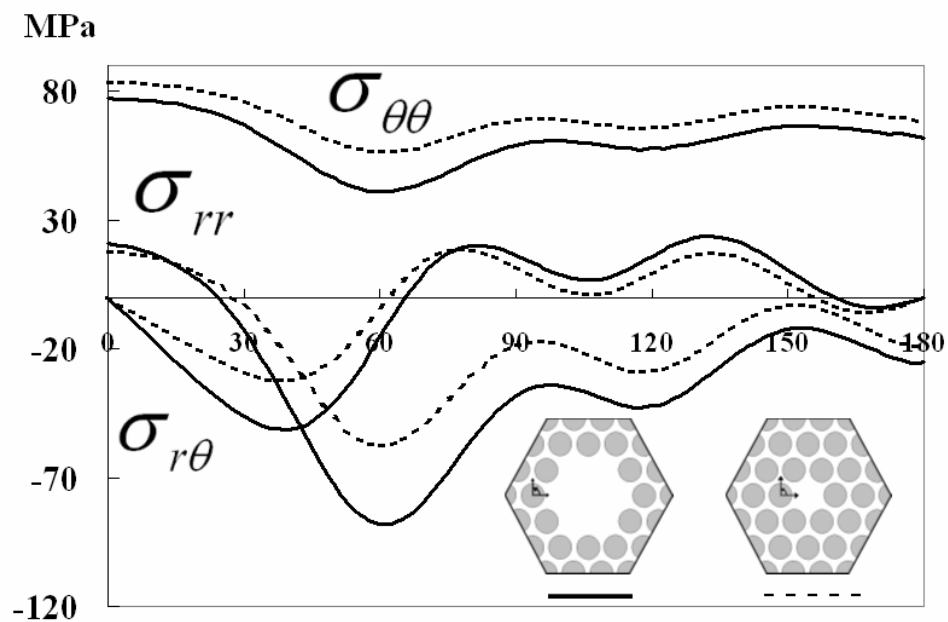


Figure 4.17. Interfacial stress states of 6 fiber missed and 1 fiber missed unit cells

4.3.5. Effect of low and high volume fraction areas

In section 3.3, it was assumed that one layer has uniformly averaged ply stresses. For example, as in Table 3.2 and 3.3, it is assumed that the ply stresses $\sigma_1 = -131.1$ MPa and $\sigma_2 = 74.6$ MPa are uniformly distributed through the 0° layer. However, since real composites have randomly distributed fiber arrangement, there can exist high fiber volume fraction zones or low fiber volume fraction zones, as shown in Figure 4.18, ply stresses will vary. In order to investigate this, large periodic unit cells can be extended to contain high volume fraction zones and low volume fraction zones. In this section, the effect of high volume fraction zones and low volume fraction zones on ply stress and interfacial stress fields are studied. In order to represent high volume fraction zones and low volume fraction zones, the unit cells can be constructed in Figure 4.19.

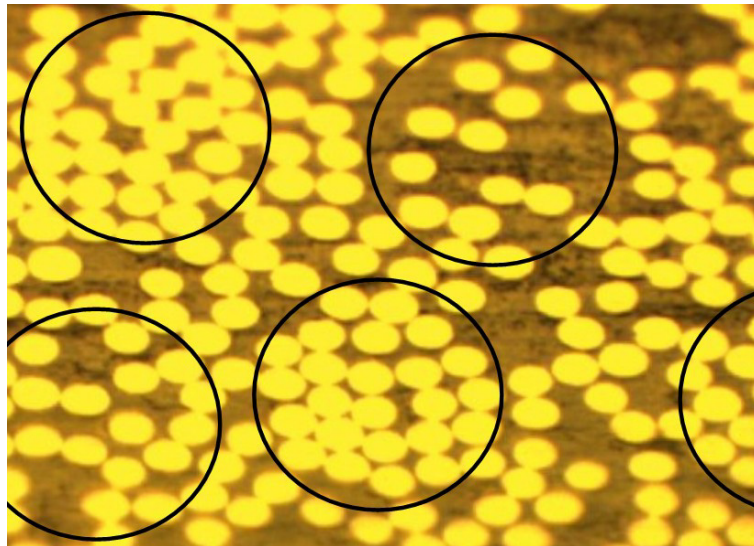


Figure 4.18. High volume fraction zones and low volume fraction zones

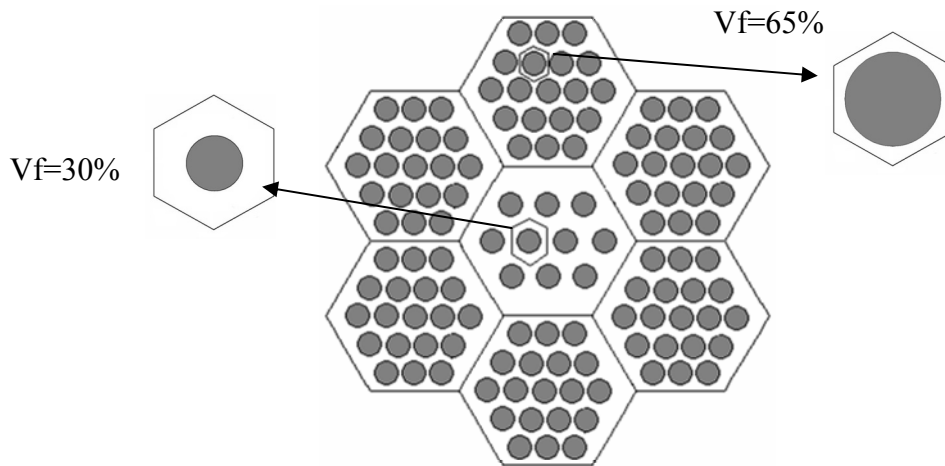


Figure 4.19. Unit cells to represent high and low volume fraction zones

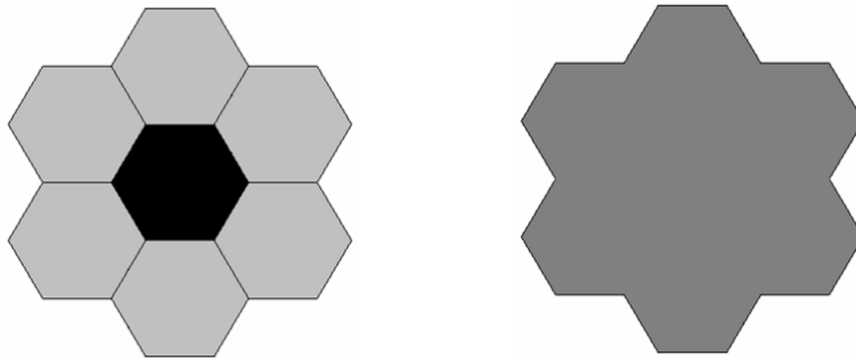
As in Figure 4.19, the center area has only 10 fibers, while the other each area has 19 fibers. Therefore, the center area can be considered a low volume fraction zone, and the other areas can be considered high volume fraction zones. Since the volume fraction of the unit cell of the center area is 30%, and the volume fraction of the unit cell of the other areas is 65% described in Figure 4.19, the total volume fraction of entire unit cell is 60%. In order to study the effect of volume fraction zones and low volume fraction zones on stress fields of each area, the following four step processes are considered:

1st step: As in Figure 4.20 a), the effective thermal-elastic properties are calculated from two unit cells.

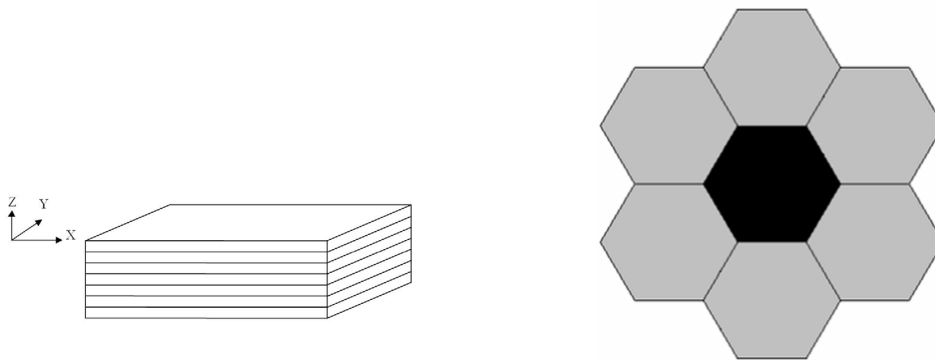
2nd step: Using the effective properties of the two unit cells, the total effective thermal-elastic properties are calculated for the entire areas in Figure 4.20 b).

3rd step: Using the total effective properties, laminates, which are shown in section 3.3.2, are constructed and thermal loading is applied to the laminates. Using CLPT code, ply stresses of the each layer are obtained in Figure 4.20 c).

4th step: The ply stresses are applied to the first homogenization stage, and average stresses of the each area are obtained in Figure 4.20 d).



a) 1st step: Effective properties of each area b) 2nd step: Effective properties of total area



c) 3rd step: ply level stresses

d) 4th step: averaged stresses of each area

Figure 4.20. Four step processes

As a result, the unit cell in Figure 4.20 b) has the same ply level stresses as $\sigma_1 = -131.1$ MPa and $\sigma_2 = 74.6$ MPa with the layer of 0° mentioned in section 3.2.2. However, the each area of the unit cell has different stresses. Figure 4.21 denotes the average stresses of each area. As in Figure 4.21, the low volume area has larger σ_2 and smaller σ_1 than the other areas. It is already studied in section 4.2.4 that σ_2 is more significant than σ_1 for damage of interface. Therefore the low volume fraction area will be more critical for composite damage. Also since it is known that the tensile strength of matrix is 77MPa, the first failure will be initiated at the low volume fraction zones.

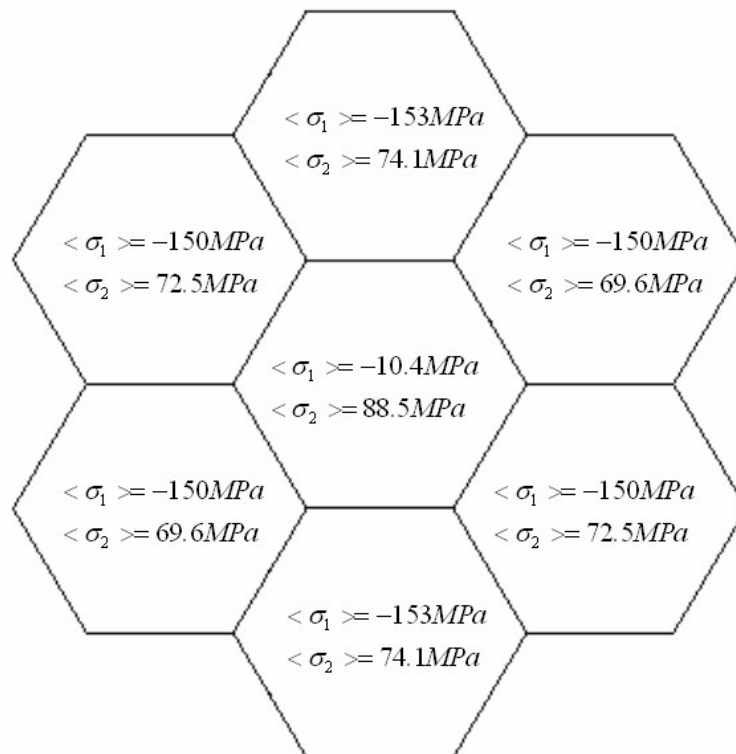


Figure 4.21. Non-uniformly distributed ply stresses

In order to study the effect of ply stresses of low volume fraction area on interfacial stresses, the ply stresses of low volume fraction area are applied to unit cell having 30% volume fraction, and the results are compared with interfacial stresses of perfectly periodic 60% volume fraction case in Figure 4.22. As in Figure 4.22, 30% volume fraction unit cell in low volume fraction area has higher interfacial stresses. Therefore, it can be considered that fibers located in low volume fraction areas will be more dangerous for fiber/matrix debonding than perfectly regular fibers.

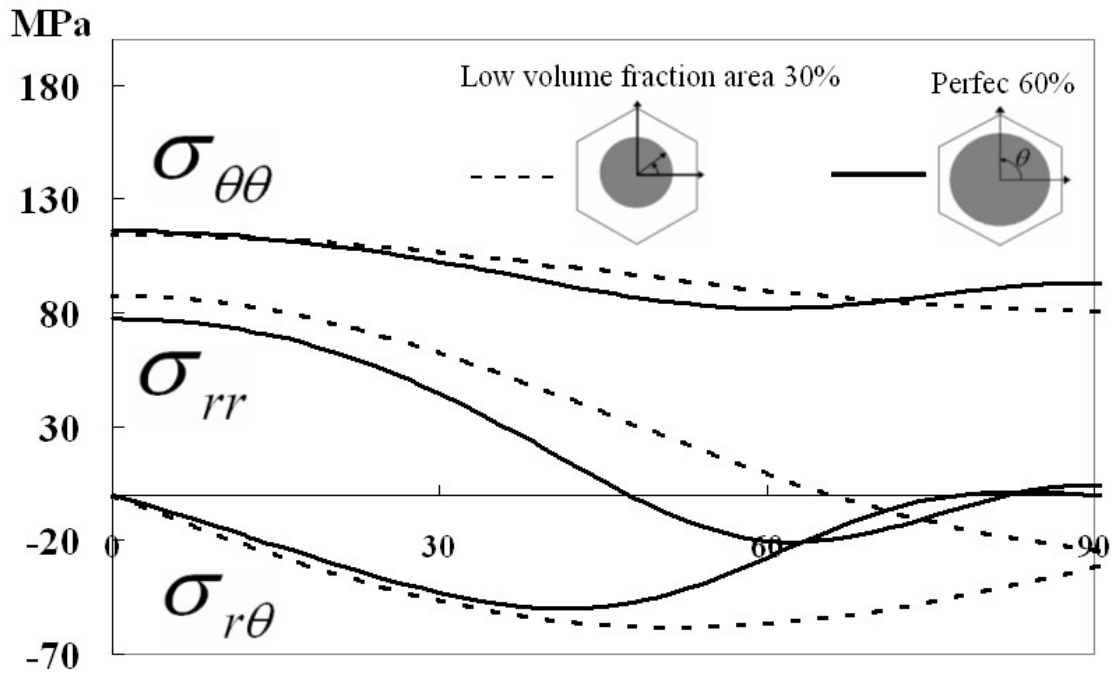


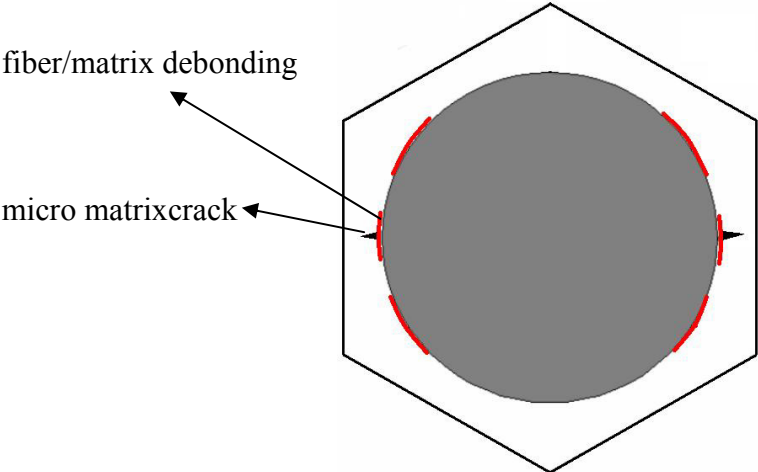
Figure 4.22. Interfacial stresses of a fiber located in low volume fraction area

4.4. The worst fiber distribution case

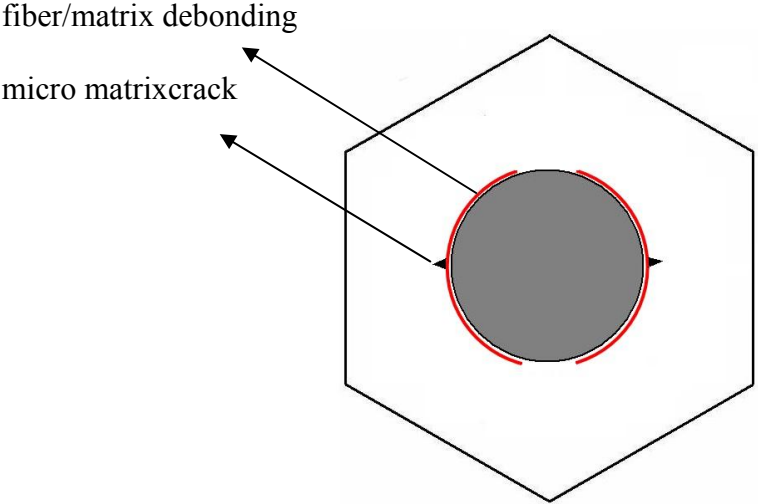
Various parametric studies have been studied for interfacial stress states. From the results, it was found that ply stresses are concentrated in low fiber volume fraction areas, and these concentrated ply stresses produce high interfacial stresses of fibers located in low fiber volume fraction areas. The fiber/matrix debonding interfaces caused by radial and shear stresses, and micro matrixcrack areas caused by tangential stresses are depicted for 60% volume fraction fiber in perfect array and 30% volume fraction fiber in low fiber volume fraction areas in Figure 4.23. The failure areas are predicted based on the maximum stress criterion. As in Figure 4.23, 30% volume fraction fiber in low fiber volume fraction areas has more possibility of debondings and micro matrixcracks than the case of 60% volume fraction fiber in perfect array.

Also it has been studied that existence of matrix-rich zones can increase interfacial stresses of fibers located near the matrix-rich zones. As shown in Figure 4.24 a), the model can be also suggested for one of the worst fiber distribution cases which can have high possibility of fiber/matrix debonding and micro matrixcracks. The thermal loading and ply stresses are applied to the unit cell which has matrix pocket in the center region, and the interfacial stresses for the 4 fibers are presented in Figure 4.24 b), c), d), and e). When compared to the interfacial stresses of perfect hexagonal case in Figure 4.8, the 4 fibers have higher interfacial stresses. Figure 4.24 a) shows the possible areas of fiber/matrix debonding caused by radial and shear stresses and micro matrixcracks caused by tangential stresses for the unit cell. As in Figure 4.24, the fibers located near

matrix-rich zones have more possibility of debonding and micro matrixcracks than perfect hexagonal case.

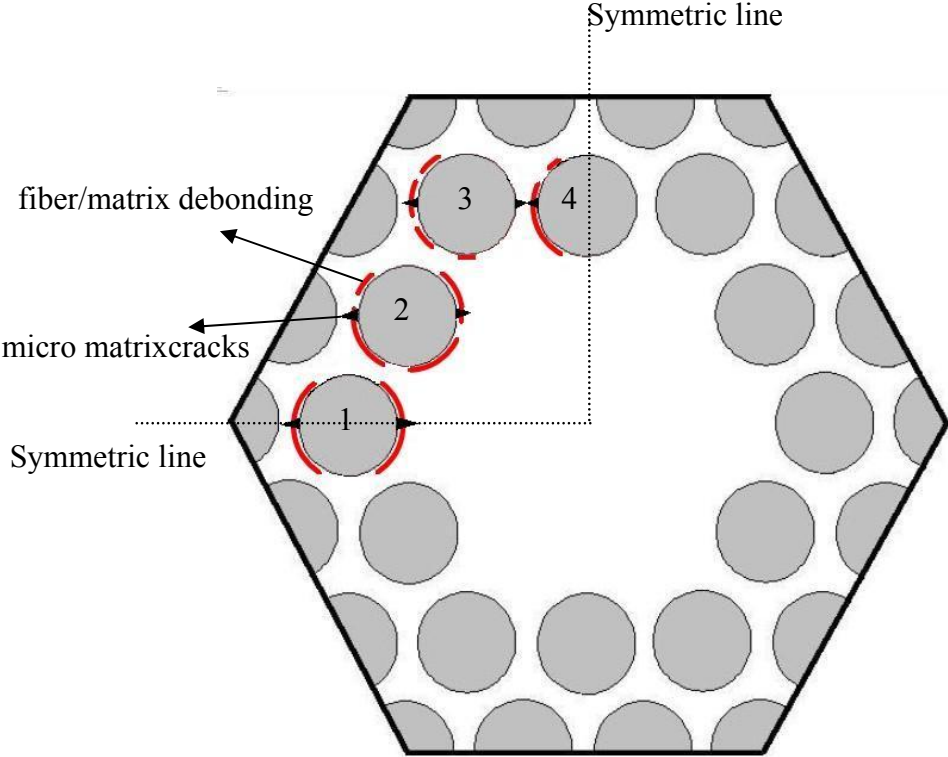


a) 60% Vf case in perfect hexagonal array



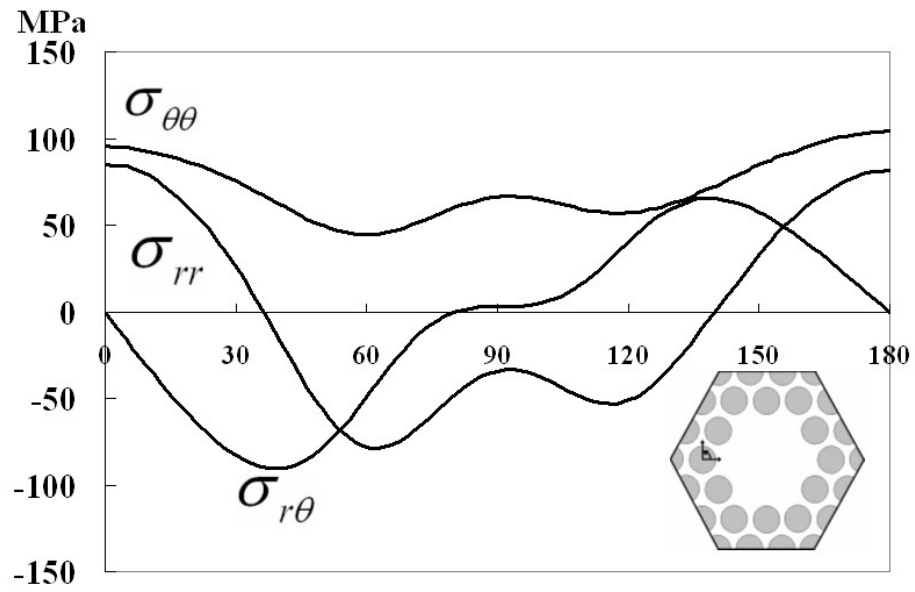
b) 30% Vf case in low fiber volume fraction area

Figure 4.23. Debonding and microcrack areas

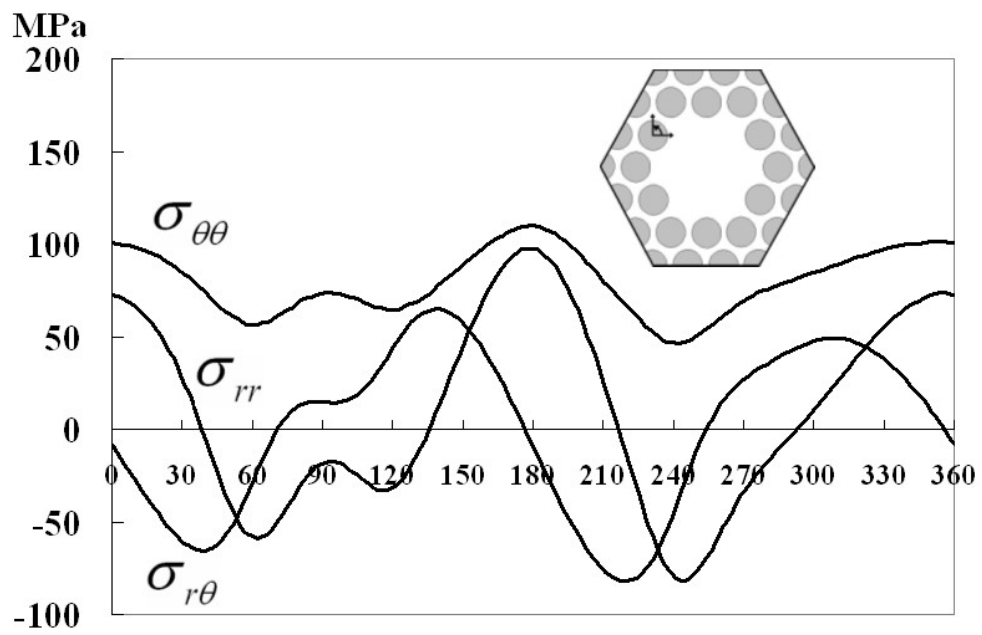


a) 6 fiber missed unit cell

Figure 4.24. Debonding and microcrack areas of 6 fiber missed large pattern unit cell

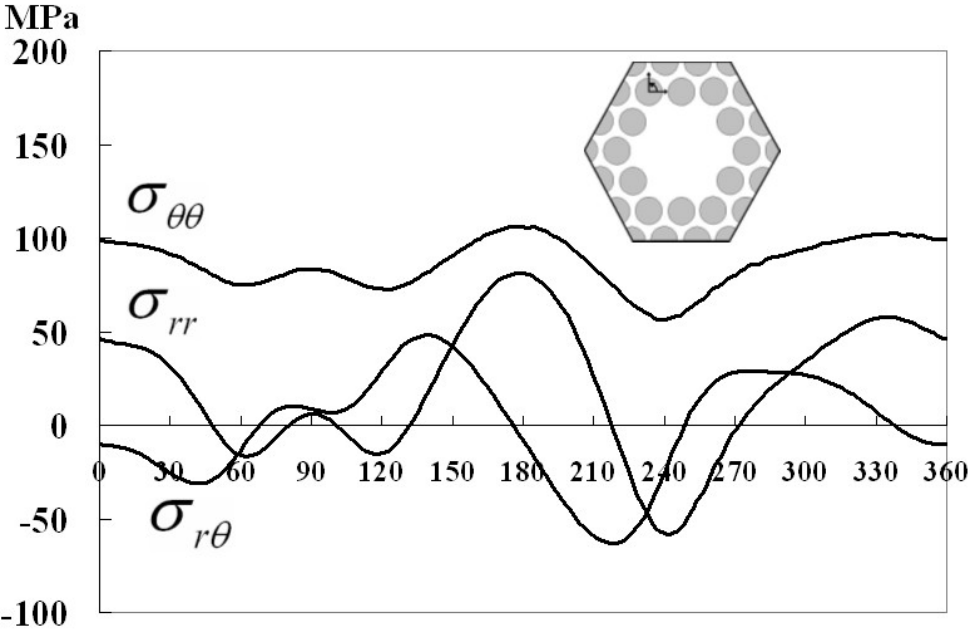


b) Interfacial stresses of fiber 1

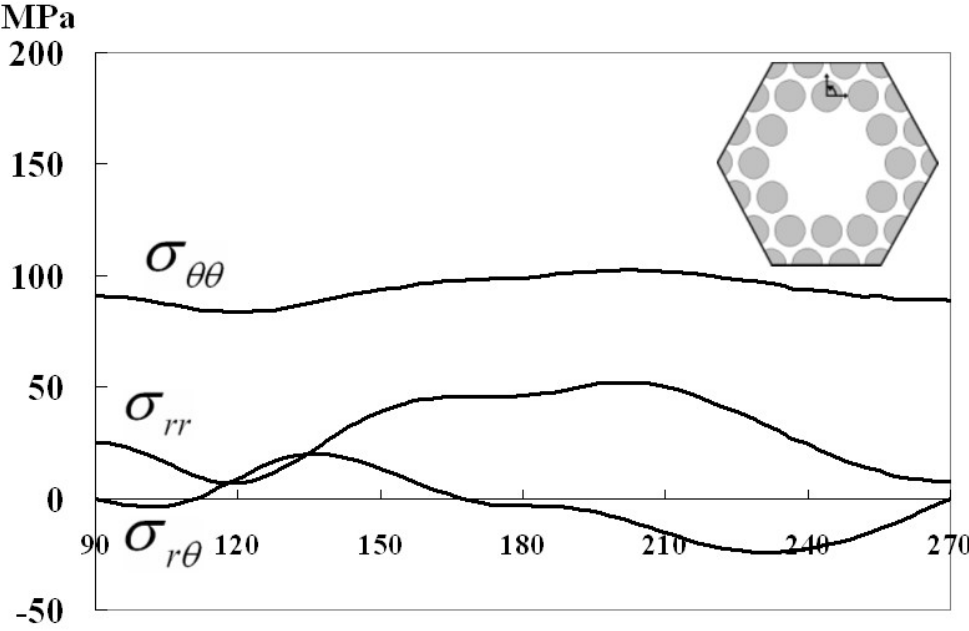


c) Interfacial stresses of fiber 2

Figure 4.24. Continued



d) Interfacial stresses of fiber 3



e) Interfacial stresses of fiber 4

Figure 4.24. Continued

In order to investigate which fiber distribution is the worst case and determine ranking of stress level, interfacial stresses of 8 fibers for 5 fiber distribution patterns in Figure 4.25 are compared.

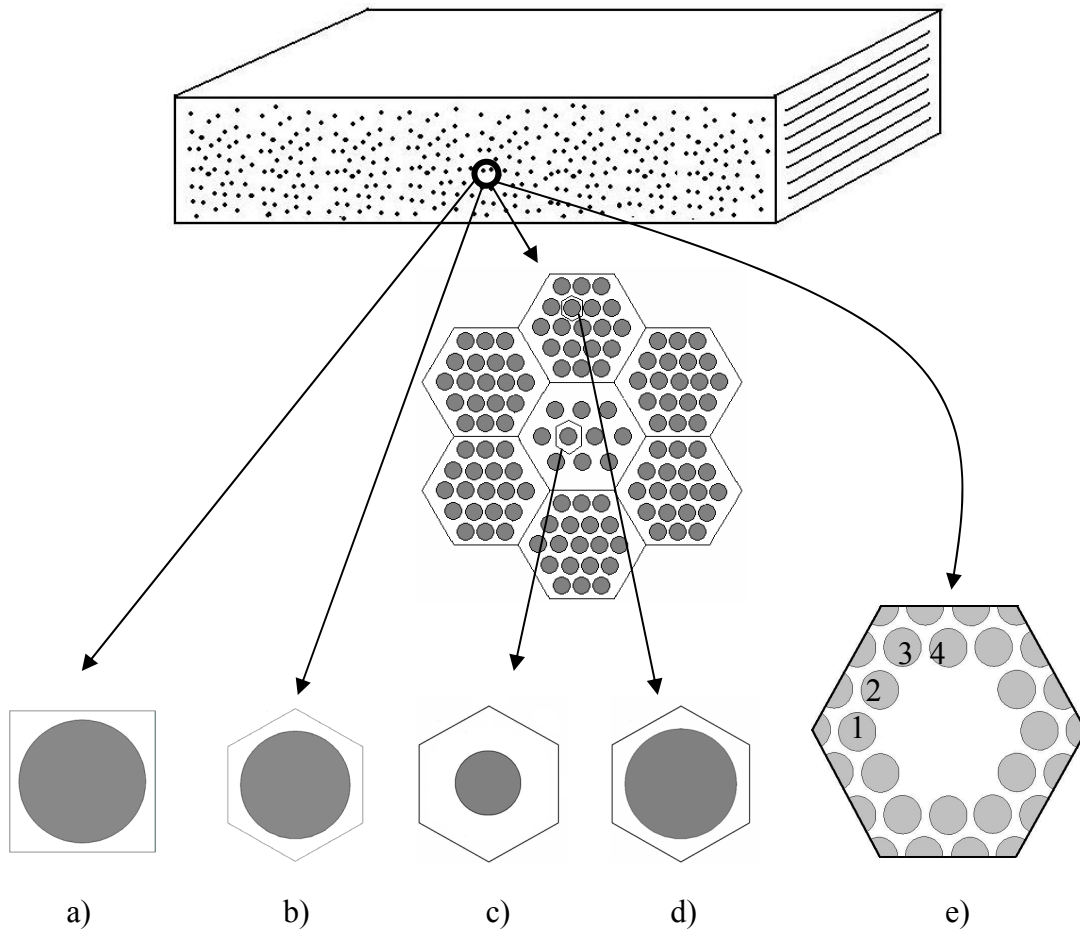


Figure 4.25. 8 fibers for 5 assumed fiber distributions

- a) Perfect square array (PS)
- b) Perfect hexagonal array (PH)
- c) Hexagonal array in low fiber volume fraction areas (HL)
- d) Hexagonal array in high fiber volume fraction areas (HH)
- e) Matrix-rich zones (M1, M2, M3, and M4)

The each interfacial stress component of 8 fibers are divided by the assumed interfacial normal strength, shear strength and matrix tensile strength respectively, and the highest value is ranked at the first in Table 4.6.

Table 4.6. Ranking of interfacial stresses of 8 fibers caused by thermal loading of a laminate

Ranking	Fiber ($\sigma_{rr} / \sigma_{rr}^S$)	Fiber ($\sigma_{r\theta} / \sigma_{r\theta}^S$)	Fiber ($\sigma_{\theta\theta} / \sigma_{\theta\theta}^S$)
1	M2 (1.55)	M1 (2.94)	M2 (1.52)
2	M1 (1.38)	M2 (2.64)	PH (1.51)
3	HL (1.37)	M3 (2.01)	HL (1.48)
4	M3 (1.26)	HL (1.76)	M4 (1.48)
5	PH (1.21)	PS (1.7)	M3 (1.47)
6	HH (1.14)	PH (1.52)	PS (1.47)
7	M4 (0.91)	HH (1.45)	HH (1.44)
8	PS (0.87)	M4 (0.82)	M1 (1.32)

σ^S : Interfacial strength

If σ / σ^S is higher than 1, it means failure based on the maximum stress criterion. From the result, it is shown that number 2 fiber of case e) is ranked at the first for fiber/matrix debonding and micro matrixcrack, and at the second for torsional sliding failure. Also it is likely that number 1 and 3 of case e) have higher possibility of failure than the other arrays. Therefore, it is concluded that case e), i.e. fiber distributions, which have matrix-rich zones, is the worst case for microcracks, and among of the fibers located near matrix-zones, number 2 fiber has the highest possible for microcracks.

While Table 4.6 shows about the ranking of interfacial stresses for thermal loading in a laminate, Table 4.7 and 4.8 show the ranking of interfacial stresses for thermal loading and mechanical loading in a lamina. If only thermal loading is

considered in a lamina, the number 2 fiber of case e) is ranked at the first for fiber/matrix debonding and micro matrixcrack, but for mechanical loading, the fiber is ranked very lowly, because matrix-rich zones are beneficial for mechanical loading to the strength, but harmful for thermal loading to the strength. As a result, for the combined loading condition, the number 2 fiber of case e) has the highest possibility of microcracks because of near matrix-rich zones.

Table 4.7. Ranking of interfacial stresses of 8 fibers caused by thermal loading of unidirectional lamina

Ranking	Fiber ($\sigma_{rr} / \sigma_{rr}^S$)	Fiber ($\sigma_{r\theta} / \sigma_{r\theta}^S$)	Fiber ($\sigma_{\theta\theta} / \sigma_{\theta\theta}^S$)
1	M1 (0.42)	M1 (2.42)	HH (1.06)
2	M3 (0.42)	M3 (2.42)	PS (1.04)
3	PS (0.23)	M2 (1.21)	M1 (1.01)
4	HH (0.07)	M4 (1.21)	M3 (1.01)
5	M2 (0.04)	PS(0.9)	M2 (0.99)
6	M4 (0.04)	HH (0.45)	M4(0.99)
7	PH (-0.11)	HP (0.3)	PH (0.97)
8	HL (-0.23)	HL(0.15)	HL (0.65)

Table 4.8. Ranking of interfacial stresses of 8 fibers caused by mechanical loading of unidirectional lamina in transverse direction

Ranking	Fiber ($\sigma_{rr} / \sigma_{rr}^S$)	Fiber ($\sigma_{r\theta} / \sigma_{r\theta}^S$)	Fiber ($\sigma_{\theta\theta} / \sigma_{\theta\theta}^S$)
1	PS (2.27)	HH (1.76)	PS (0.94)
2	PH (1.92)	M2 (1.61)	M3 (0.75)
3	M4 (1.84)	PH (1.52)	M4 (0.73)
4	M3 (1.83)	M3 (1.45)	PH (0.65)
5	M2 (1.82)	HL (1.42)	M2 (0.61)
6	HH (1.61)	PS (1.36)	HH (0.6)
7	HL (1.56)	M4 (1.27)	HL (0.58)
8	M1 (1.52)	M1 (1.36)	M1 (0.57)

4.5 Uncertainty of fiber transverse CTE

4.5.1 Importance of fiber transverse CTE

Since thermally induced stresses are due to the mismatch between coefficients of thermal expansion (CTE) of fiber and matrix, obtaining exact CTE values of fiber and matrix is very important. While CTE values of matrix are well known because the experimental tests of those are easy due to the macro level scale, very little data are available in the literature on transverse CTE of fiber. Measurement of fiber transverse CTE is very difficult because of the micro level scale of the test (The fiber diameter is $5 \sim 20 \mu m$ [26]). In addition, it is seen sometimes that the literatures have different CTE values for the same fiber. Especially the transverse CTE of fiber poses a problem on account of the small diameter of fiber. These difficulties cause measurement errors when experimental tests are conducted, and eventually these measurement errors could create significant errors when numerical analysis is performed at the macro and micro level.

4.5.2 Range of fiber transverse CTE values

Table 4.9 shows the different CTE values obtained experimentally for IM7 carbon fiber. The fiber transverse CTE values are ranged from $4.4 \times 10^{-6} / ^\circ C$ to $10 \times 10^{-6} / ^\circ C$, and the fiber longitudinal CTE values are ranged from $-2.29 \times 10^{-6} / ^\circ C$ to $-0.4 \times 10^{-6} / ^\circ C$.

Table 4.9. CTE values of IM7 carbon fiber in literatures

	[Ref 26]	[Ref 30]	[Ref 31]	[Ref 32]	Range
$\alpha_L^f (\times 10^{-6} / C^\circ)$	-0.4	-0.9	-2.29	-1.0	-2.29~-0.4
$\alpha_T^f (\times 10^{-6} / C^\circ)$	4.4~6.6	7.2	9.2	10	4.4~10

It will be considered that the fiber longitudinal CTE value is known fairly accurately because the fiber longitudinal CTE value can be obtained easily by experimental text, and the longitudinal CTE value does not affect significantly on stress fields, because of very small value compared to fiber transverse CTE, so the fixed value of $-0.4 \times 10^{-6} / C^\circ$ for longitudinal CTE will be used for this study.

Table 4.10. Variations of difference between fiber and matrix CTE values

	$\alpha_T^f (\times 10^{-6} / C^\circ)$	Variation from 4.4	$\alpha^m - \alpha_T^f (\times 10^{-6} / C^\circ)$	Variation from 53.2
[Ref 26]	4.4	-	53.2	-
[Ref 26]	6.6	50%	51	4.1%
[Ref 30]	7.2	63.6%	50.4	5.3%
[Ref 31]	9.2	109.1%	48.4	9.0%
[Ref 32]	10	127.3%	47.6	10.5%

$$\alpha^m = 57.6 \times 10^{-6} / C^\circ$$

Table 4.10 shows the variations of difference between fiber and matrix CTE values. The largest value of fiber transverse CTE has variation of 127.3% with the smallest value. This amount of variation may be very big. However, when considering that thermally induced stresses depend on the difference between fiber CTE and matrix

CTE ($\alpha^m - \alpha_r^f$), the largest variation of ($\alpha^m - \alpha_r^f$) is only 10.5% compared to the smallest variation of ($\alpha^m - \alpha_r^f$).

4.5.3 Effect of errors in assumed fiber transverse CTE values on interfacial stresses in lamina

In order to investigate the effect of uncertainty in the transverse CTE of the fiber in a lamina, a unit cell of 60% volume fraction is constructed for a lamina, and its interfacial stresses are investigated for the smallest and largest fiber transverse CTE values under thermal loading of -300°C .

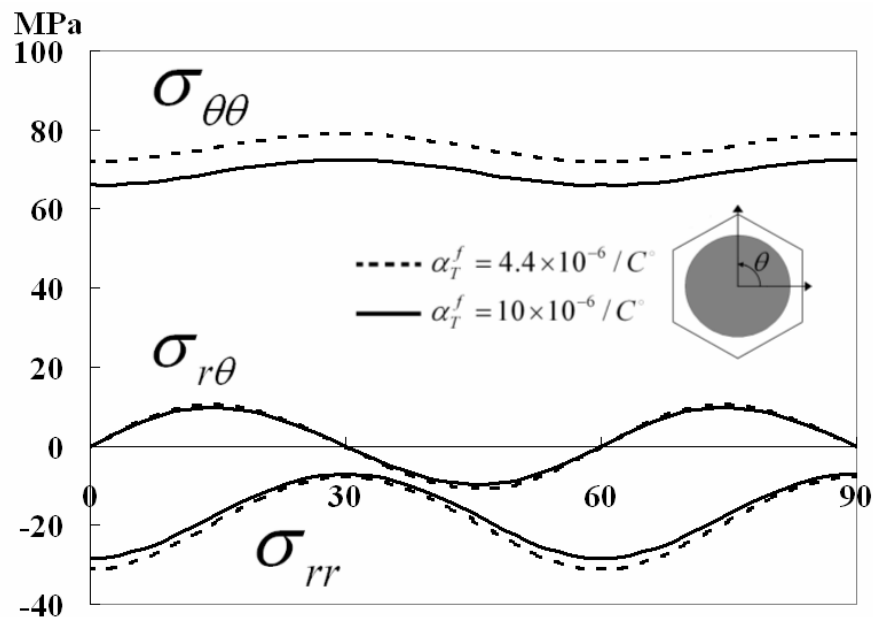


Figure 4.26. Interfacial stress states for the smallest and largest fiber transverse CTE values in lamina

Figure 4.26 shows the interfacial stress distributions for the largest and smallest fiber CTE values. The results show that the radial, shear, and tangential stresses are not much different for the two CTE values. While the fiber transverse CTE values are changed from $4.4 \times 10^{-6} / ^\circ C$ to $10 \times 10^{-6} / ^\circ C$ with the variation of 127.3%, the differences in the interfacial stresses are relatively small (10.5%) compared to the large differences in the fiber transverse CTE values (Table 410). To explain these thermally induced interfacial stresses, the following composite cylindrical model in Figure 4.27 and analytical solutions have been used [33].

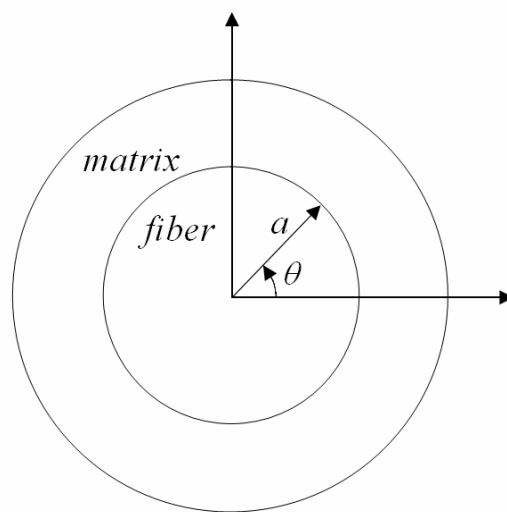


Figure 4.27. Composite cylinder model

At the interface, the interfacial stresses can be expressed.

$$\sigma_{rr} = -A \frac{V_m}{V_f} \quad (4.1)$$

$$\sigma_{\theta\theta} = A \left(1 + \frac{1}{V_f} \right) \quad (4.2)$$

where

$$A = \frac{V_f [E_f V_f (1 + \gamma_m) + E_m V_m ((1 + \gamma_f)(\alpha_m - \alpha_f) \Delta T]}{2E_f V_m \left(\frac{\gamma_m V_f}{E_m} + \frac{\gamma_f V_m}{E_f} \right)^2 - \left(\frac{V_f}{E_m} + \frac{V_m}{E_f} \right) [E_f (1 + \gamma_m + V_f - \gamma_m V_f) + E_m (V_m - \gamma_f V_m)]} \quad (4.3)$$

Regarding only thermal effect, the stress components are reduced following as

$$\sigma_{rr} = \frac{V_m E_m E_f (\alpha_m - \alpha_f) \Delta T}{E_f V_f + E_m V_m + E_f} \quad (4.4)$$

$$\sigma_{\theta\theta} = \frac{-(V_f + 1) E_m E_f (\alpha_m - \alpha_f) \Delta T}{E_f V_f + E_m V_m + E_f} \quad (4.5)$$

In the above equations, it is shown that the interfacial stresses depend on $(\alpha_m - \alpha_f)$. As in Table 4.8, the largest variation of $(\alpha_m - \alpha_f)$ between fiber and matrix is only 10.5%, i.e. the large uncertainty of fiber transverse CTE values do not affect the interfacial stress states significantly, because the CTE difference $(\alpha_m - \alpha_f)$ between fiber and matrix is the main effect on the interfacial stress states. Even though interfacial stresses depend on volume fraction, variation of interfacial stresses for the smallest and largest fiber transverse CTE values does not depend on the volume fraction. Therefore, it is concluded that if variation of 10% stress difference can be considered not much

difference, even though fiber transverse CTE is not known exactly, the interfacial stress states in lamina can be obtained fairly accurately.

4.5.4 Sensitivity of lamina CTE to change fiber volume fractions

It was studied that errors in assumed fiber transverse CTE values are not significant for interfacial stress states in a lamina, even though volume fraction is changed. In this section, how much the errors in assumed fiber transverse CTE values will affect effective lamina CTE values, when volume fraction is changed. In order to find out the effect of errors in assumed fiber transverse CTE values on the effective lamina transverse CTE values, the effective lamina transverse CTE values are obtained for the assumed fiber transverse CTE values, when its volume fractions are changed. The Figure 4.28 shows the variations of effective lamina transverse CTE values for assumed fiber transverse CTE values.

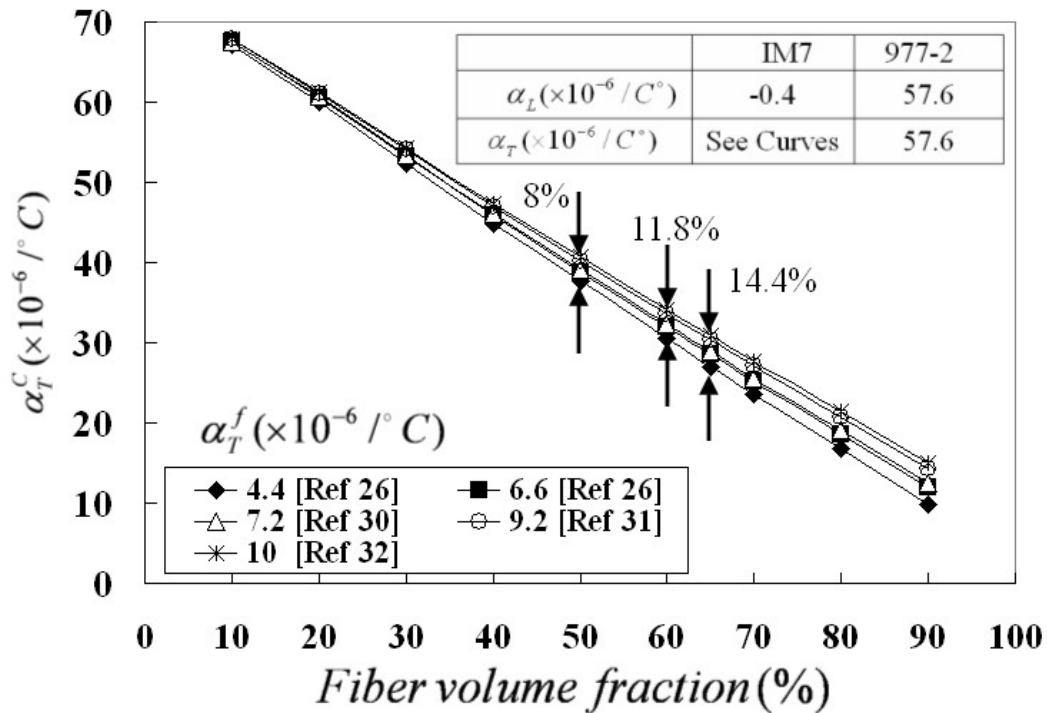


Figure 4.28. Sensitivity of effective lamina transverse CTE to fiber volume fraction

As in Figure 4.28, in low volume fractions, the variation of fiber transverse CTE values does not affect much the effective CTE significantly, but in high volume fractions, the effective CTE value for the assumed fiber transverse CTE values have much different results. Table 4.11 shows the variations of effective lamina transverse CTE values for 50%, 60%, and 65% volume fractions which are used typically in industry. While the lamina of 50% volume fraction has the variation of 8% for the smallest and largest fiber transverse CTE values, the lamina of 65% volume fraction has the difference of 14.4% for the two fiber transverse CTE values. Since lamina level properties become very important for macro level analysis, it is needed to investigate

that how much this amount of variation of effective lamina CTE value of 50%, 60% and 65% volume fraction composite will affect results of macro level analysis.

Table 4.11. Sensitivity of effective lamina transverse CTE to fiber volume fraction

	Effective α_T^c 50%	Effective α_T^c 60%	Effective α_T^c 65%
when $\alpha_T^f = 4.4 \times 10^{-6} / C^\circ$	$37.6 \times 10^{-6} / ^\circ C$	$30.5 \times 10^{-6} / ^\circ C$	$27 \times 10^{-6} / ^\circ C$
when $\alpha_T^f = 10 \times 10^{-6} / C^\circ$	$40.6 \times 10^{-6} / ^\circ C$	$34.1 \times 10^{-6} / ^\circ C$	$30.9 \times 10^{-6} / ^\circ C$
Variation	8%	11.8%	14.4%

4.5.5 Effect of errors in assumed fiber transverse CTE values on ply stresses in laminate composite

In order to investigate the effect of errors in assumed fiber transverse CTE values on laminate composites, $[90/\pm 45/0]_s$ laminate models are constructed for different volume fractions. When the thermal loading of $-300^\circ C$ is applied to the laminate composites, the ply stresses of each layer are obtained by CLPT. Using the CLPT code, the ply stresses of each layer are obtained in global coordinate system, and the ply stresses are transformed in material coordinate system. Table 4.12 shows the ply stresses of 0° layers of $[90/\pm 45/0]_s$ composite for different volume fractions, while the two smallest and largest fiber transverse CTE values are used. The negative values are the ply stress of longitudinal direction, and the positive values are the ply stress of transverse direction of the layer.

Table 4.12. Ply level stresses for smallest and largest fiber transverse CTE values in $[90/\pm 45/0]_S$ composite

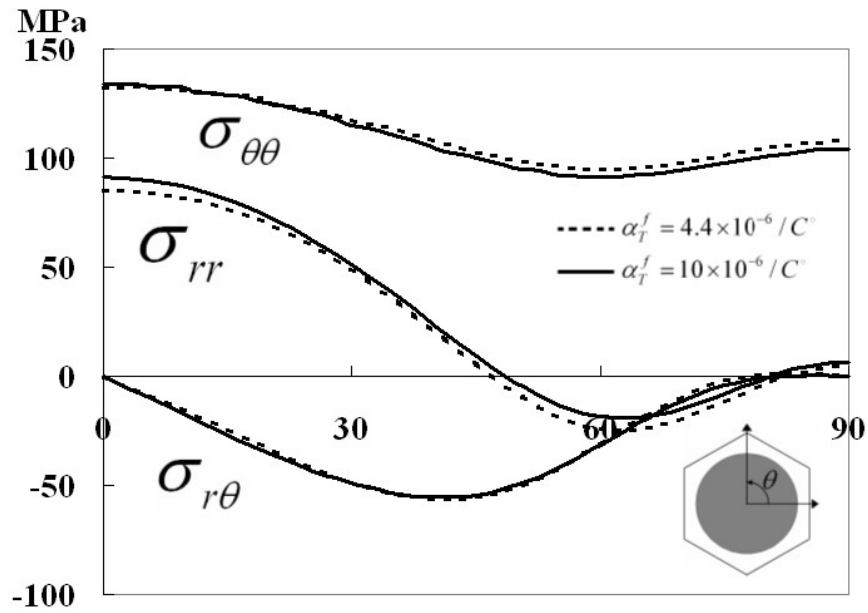
	Ply stresses (MPa) Vf= 50%	Ply stresses (MPa) Vf= 60%	Ply stresses (MPa) Vf= 65%
when $\alpha_T^f = 4.4 \times 10^{-6} / C^\circ$	∓ 75.14	∓ 71.48	∓ 69.32
when $\alpha_T^f = 10 \times 10^{-6} / C^\circ$	∓ 81.22	∓ 80.15	∓ 79.62
Increasing rate	8%	12%	15%

While the fiber transverse CTE values are used from $4.4 \times 10^{-6} / C^\circ$ to $10 \times 10^{-6} / C^\circ$, the laminate, which has 50% volume fraction, has 8.1% variation of the ply stress, and 65% volume fraction case has 14.9% variation of the ply stress. The Table 4.12 says that the uncertainty problem of errors in assumed fiber transverse CTE values will cause difficulty for predicting the ply stresses of laminate composite. As in Figure 4.24, it was already studied that high volume fraction composites have high variation of effective CTE values, while the fiber transverse CTE values are used from $4.4 \times 10^{-6} / C^\circ$ to $10 \times 10^{-6} / C^\circ$. In the next section, the effect of these variations of ply stresses on interfacial stresses will be investigated in micro level.

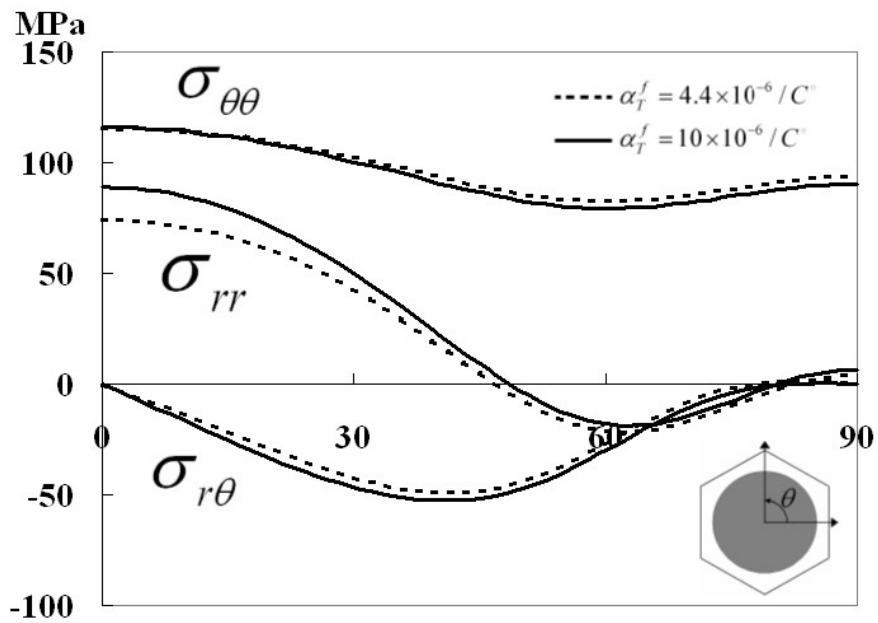
4.5.6 Effect of errors in assumed fiber transverse CTE values on interfacial stresses in laminate composite

As in Table 4.12, the 50%, and 60%, and 65% volume fraction laminate composites have the ply stress variations of 8%, and 12%, and 15% respectively, when fiber transverse CTE values are changed from $4.4 \times 10^{-6} / C^\circ$ to $10 \times 10^{-6} / C^\circ$. These

amounts of ply stresses are applied to the each volume fraction unit cell with the thermal loading of $-300^{\circ}C$, and the interfacial stress states are studied for two fiber transverse CTE values. The Figure 4.29 shows that how much the interfacial stress states are different for two fiber transverse CTE value cases. The remarkable part is that when the fiber transverse CTE is changed from $4.4 \times 10^{-6} / C^{\circ}$ to $10 \times 10^{-6} / C^{\circ}$, the radial stress of 65% volume fraction case is increased by 24% at 0° position, while 50% volume fraction case has only 11% variation at the same position, as in Table 4.13. This result means that uncertainty of fiber transverse CTE causes the higher variation of interfacial stresses for higher volume fraction laminate composites. The 60% volume fraction case has 20% variation of interfacial stresses for two fiber transverse CTE values. It was already studied that the 60% volume fraction in a lamina has only around 10% variation for two fiber transverse CTE values. However, if the ply stresses caused by laminate effect are considered to the interfacial stress states, the error in assumed fiber transverse CTE values yield 20% variation of the radial stress. Therefore, it is concluded that the error in assumed fiber transverse CTE values make high errors for predicting interfacial stress states.

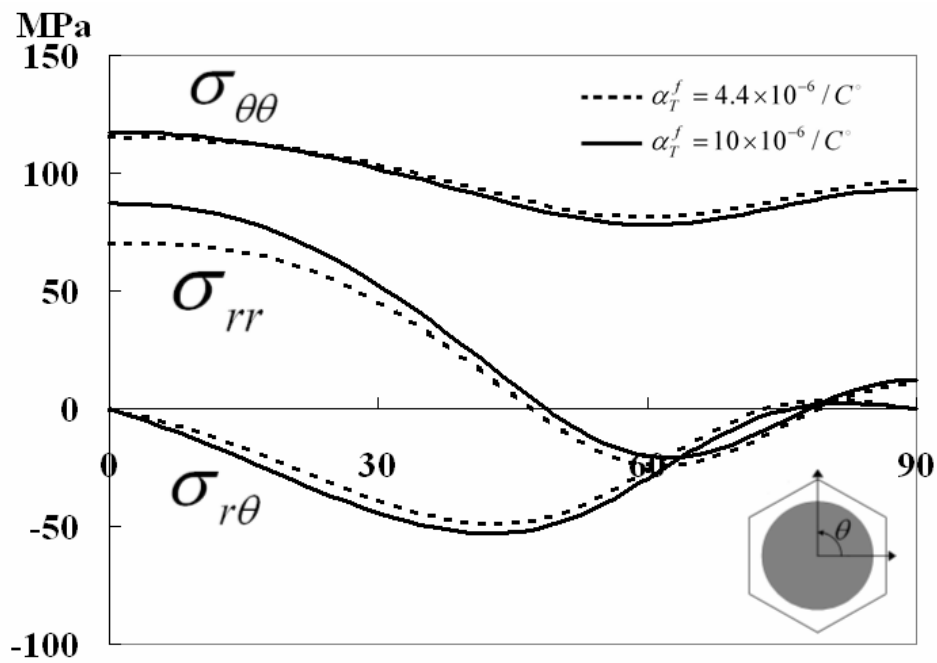


a) Interfacial stresses of 50% volume fraction



b) Interfacial stresses of 60% volume fraction

Figure 4.29. Interfacial stress states for assumed fiber transverse CTE values in a laminate



c) Interfacial stresses of 65% volume fraction

Figure 4.29. Continued

Table 4.13. Variation of radial stresses for fiber transverse CTE values

	Radial stress at 0° point (MPa) Vf= 50%	Radial stress at 0° point (MPa) Vf= 60%	Radial stress at 0° point (MPa) Vf= 65%
when $\alpha_T^f = 4.4 \times 10^{-6} / C^\circ$	82	74.1	70.1
when $\alpha_T^f = 10 \times 10^{-6} / C^\circ$	91	89	87.1
Increasing rate	11%	20%	24%

4.5.7 Effect of errors in assumed fiber transverse CTE values on interfacial stresses in high volume fraction area for laminate composite

In the previous section, it was studied that high volume fraction composite will have high variation of interfacial stresses when considering uncertainty of fiber transverse CTE values. In this section, since real composite can have high volume fraction areas and low volume fraction areas, the effect of errors in assumed fiber transverse CTE values on interfacial stresses in these non-uniformly distributed areas for laminate composite will be studied. In order to find out the effect of variation of fiber transverse CTE value on interfacial stresses in these areas, the following model is constructed as shown in Figure 4.30.

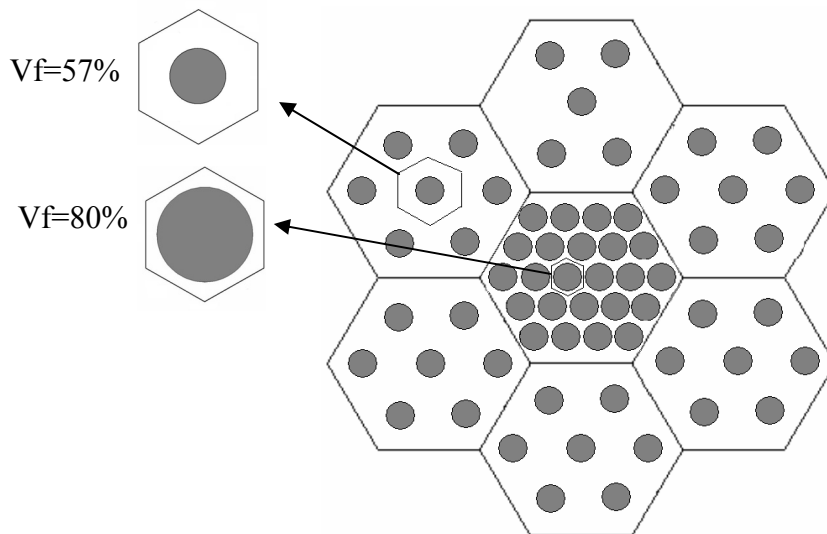


Figure 4.30. Unit cells for low and high volume fraction areas

The center area has high volume fraction with 80% and the other areas have lower volume fraction with 57%, so the total volume fraction is 60%. Therefore, it can be assumed that the center area is high volume fraction zone. Two times FEM analysis are conducted. For the first analysis, $4.4 \times 10^{-6} / ^\circ C$ is considered fiber transverse CTE value, and for the second analysis, $10 \times 10^{-6} / ^\circ C$ is considered. The same process with Figure 4.15 is used for this analysis.

As in Table 4.14, while fiber transverse CTE values are changed from $4.4 \times 10^{-6} / ^\circ C$ to $10 \times 10^{-6} / ^\circ C$, the averaged ply stresses of entire areas is increased by 12%. This variation of 12% is the same value with the result of 60% volume fraction, which is considered perfect periodic array in the Table 4.12, because the volume fraction is the same. However, the averaged stresses of the high volume fraction zone in center area are increased to 18%, and the averaged ply stresses of the other areas, which are the low volume fraction zones, are decreased to 11%. When the fiber transverse CTE values are changed, the averaged ply stresses of high volume fraction zone is increased more highly, while the averaged ply stresses of other areas are decreased. It is concluded that uncertainty of fiber transverse CTE will cause difficulty in measuring exact average ply stress fields especially in fiber-rich zones.

Table 4.14 Average stresses of low and high volume fraction areas

	Average ply stresses of total areas (MPa)	Average ply stresses of low volume fraction areas (MPa)	Average ply stresses of high volume fraction zone (MPa)
when $\alpha_T^f = 4.4 \times 10^{-6} / C^\circ$	∓ 71.2	∓ 73	∓ 60.5
when $\alpha_T^f = 10 \times 10^{-6} / C^\circ$	∓ 79.7	∓ 81	∓ 71.3
Increasing rate	12%	11%	18%

In order to investigate interfacial stress states of a fiber located in high volume fraction area, the average stresses of the high volume fraction area and thermal loading of $-300^\circ C$ are imposed to the 80% hexagonal unit cell, and its interfacial stresses are obtained. The Figure 4.31 shows the interfacial stress states having laminate effect for two fiber transverse CTE values. The remarkable result is that the radial stress is increased by 55% at 0° point. While the fiber transverse CTE of $4.4 \times 10^{-6} / ^\circ C$ causes the radial stress of 36.9 MPa, the fiber transverse CTE of $10 \times 10^{-6} / ^\circ C$ causes 57.4 MPa in high volume fraction area. In addition, if it is assumed that the interfacial normal strength is 64MPa (Table 2.1), the maximum stress criterion predicts that while the case, which uses the largest fiber transverse CTE, will be failure between 10° and 25° , the case, which uses the smallest fiber transverse CTE, will be still safe. Therefore, it is concluded that errors in assumed fiber transverse CTE values can mislead the prediction of failure possibility in high volume fraction areas.

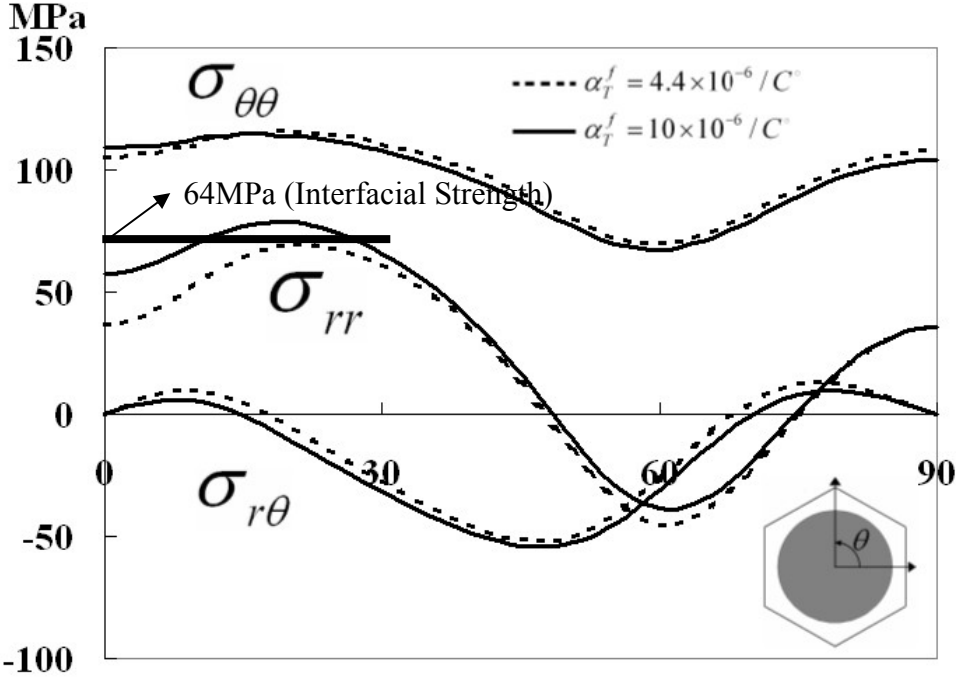


Figure 4.31. Interfacial stresses of a fiber in high volume fraction area

Table 4.15. Stress variationonn for scattered fiber transverse CTE values

	Interfacial stress in lamina (Perfect array)	Interfacial stress in laminate (Perfect array)	Interfacial stress in laminate (Fiber-rich zones)
Increasing rate	10.5%	20%	55%

Table 4.15 summarizes the results of uncertainty of fiber transverse CTE. If a lamina, which is assumed with perfectly periodic fiber arrangement and 60% volume fraction, is subjected to the thermal loading, its interfacial stress states have around 10% error for two assumed fiber transverse CTE values. However, if laminate composite is considered, the interfacial stress states of the same volume fraction case show around 20% error for two assumed fiber transverse CTE values, because the interfacial stresses

are affected by the ply stresses of laminate effect. If it is assumed that there can exist high volume fraction areas and laminate effect are considered, the radial stress at 0° of fibers located in high volume fraction areas show error of 55% for two assumed fiber transverse CTE values. Therefore, it is concluded that the uncertainty of fiber transverse CTE values will cause difficulty for micromechanical analysis.

4.6. Prediction of fiber transverse CTE by Back calculation

In section 3.2.4, if the thermal-elastic properties of fiber and matrix are known, the effective thermal-elastic properties of the composite consisting of these constituents can be obtained by micromechanics. However, since the fiber transverse CTE values are not obtained easily by experimental test, the effective lamina CTE values obtained by micromechanics have uncertainty problem. On the other hand, if laminar properties are known, back calculation can be performed to predict the fiber transverse CTE value. Figure 4.32 shows the algorithm for predicting the fiber transverse CTE of back calculation method. For this work, three composite cases are studied.

Case 1): Carbon fiber/epoxy, HTA-12/#113 at 23° [14]

Case 2): Carbon fiber/epoxy P75/ERL1962, Carbon fiber/epoxy P75/934, and Carbon fiber/cyanate ester P75/RS at 23° [34]

Case 3): Carbon fiber/epoxy, IM7/977-3 at -196° , 23° , and 150° [26]

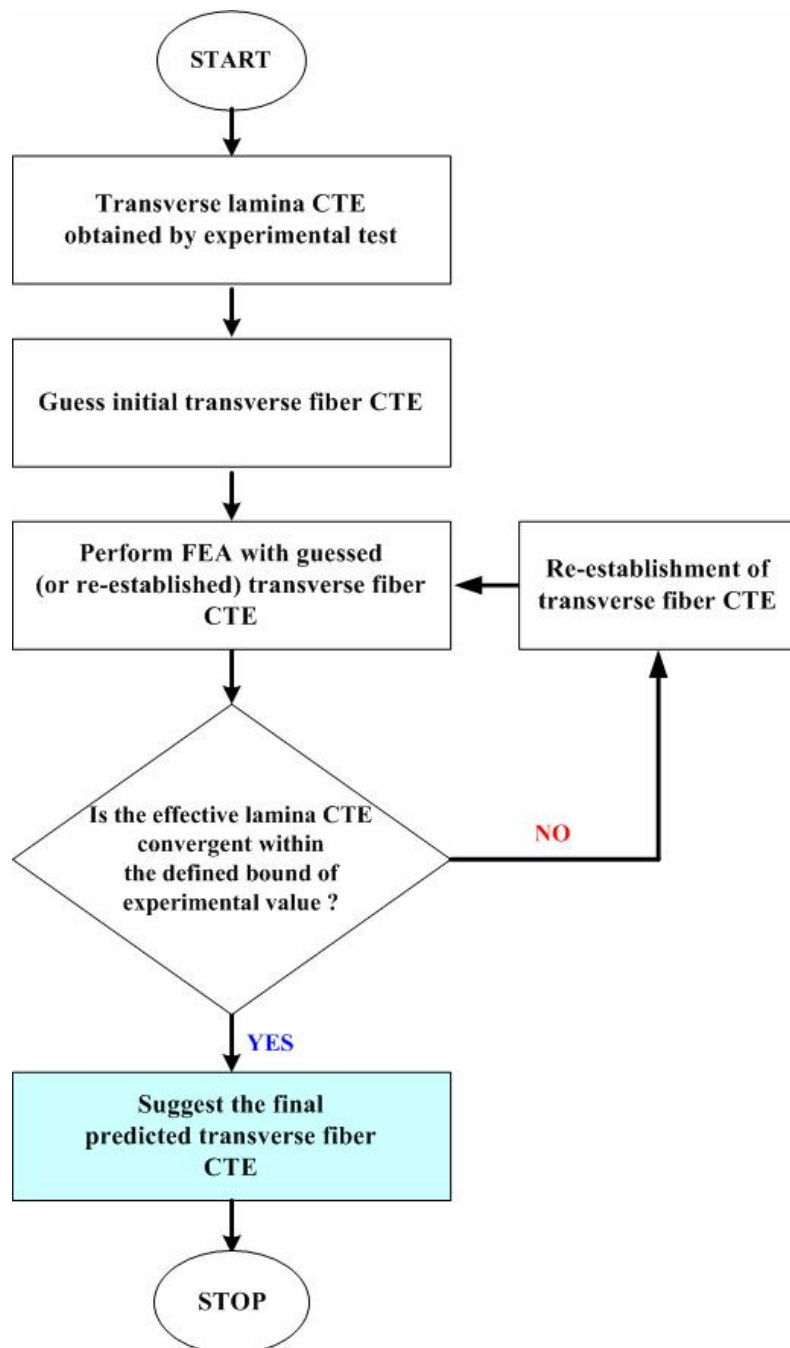


Figure 4.32. Flowchart of back calculation for predicting the fiber transverse CTE

The thermal-elastic material properties of the composites and their constituent materials are presented in Appendix B. Table 4.16 shows the results of back calculations for each composite system. As in Table 4.13, the fiber transverse CTE value of HTA-12 obtained by back calculation have good agreement with the experimental result, but the fiber transverse CTE values of P75 obtained by back calculation are little overestimated comparing with the experimental result.

The results of IM7 carbon fiber CTE values obtained by back calculation do not have big discrepancy compared with the experimental test results, $5.63(\times 10^{-6} / C^{\circ})$ for -196° and 24° temperature cases. However, the back calculation result says that the IM7 carbon fiber transverse CTE value should be $-5.5(\times 10^{-6} / C^{\circ})$ for 149° temperature case to have the same lamina CTE value. There are two possible scenarios.

- 1) At high temperature like 149° , the transverse CTE of IM7 fiber is $-5.5(\times 10^{-6} / C^{\circ})$. However, it is almost impossible, because it is known that IM7 carbon fiber has positive CTE value at high temperature [26].
- 2) At high temperature like 149° , the laminar has microcrack or fiber matrix interface debonding. Therefore, it can be considered that large amount of CTE reduction are induced by high temperature.

Table 4.16. Results of back calculation for fiber transverse CTE values

Fiber	Composite systems	Temperature	Fiber transverse CTE values ($\times 10^{-6} / C^{\circ}$)	
			Experimental	Back calculation
HTA-12	HTA-12/#113	23°	10	8.7
P75	P75/ERL1962	23°	6.84	12.2
	P75/934	23°		11.7
	P75/RS	23°		9.8
IM7	IM7/977-3	-196°	5.63	4.2
		23°		5
		150°		-5.5

Since experimental test of fibers is difficult due to the micro scale, it is not easy to believe test results sometimes. On the other hand, tests of laminar properties are easy compared to tests of fiber, because of macro level scale. Therefore, if there exists uncertainty of test results of fiber properties, these back calculation method can be one of alternative proposals.

5. CONCLUSION

A 3-dimensional finite element method has been used to compute the effective thermal-elastic properties for carbon/epoxy IM7/977-2 composite, and Classical Laminate Theory was used to compute ply level stresses for $[65/0/-65/90/-65/0/65]_T$ and $[45/90_3/-45/0_3/-45/90_3/45]_T$ laminate composite under thermal loading of $-300^\circ C$ for laminate composites. In order to investigate the effect of laminate effect on interfacial stress states, the ply level stresses were imposed to the micro unit cells with the thermal loading of $-300^\circ C$, and one more finite element method was used to obtain the interfacial stress fields of the laminate composites subjected to the thermal loading. To approximate irregularly distributed fiber arrangements, various unit cells, which can represent irregularity than perfect periodic arrays, were constructed and their interfacial stresses were studied. The interfacial stresses induced locally around a fiber showed significant dependence on the fiber distributions. For a lamina under the thermal loading, fibers located near matrix-rich zones showed high tensile radial and tangential stresses, while the radial stresses of perfect hexagonal arrangement case were compressive. These tensile interfacial stresses of fiber near matrix-rich zones will be harmful to transverse strength. Also it was found that concentrated ply stresses induced by thermal loading are concentrated in low fiber volume fraction areas, and these concentrated ply stresses produce higher interfacial stresses of fibers located in the low fiber volume fraction areas compared to perfectly periodic cases. Therefore, it is concluded that when irregularly distributed fiber arrangements are considered, fibers located near matrix-rich zones and

in low fiber volume fraction areas will have high possibility of fiber/matrix debonding and micro matrixcracks.

In order to investigate the effect of uncertainty of fiber transverse CTE values on interfacial stresses, systematic studies were performed. While interfacial stress states of a perfectly distributed fiber of 60% volume fraction in a lamina have around 10.5% errors for two assumed fiber transverse CTE values, interfacial stress states of a fiber located in high volume fraction zones in a laminate are increased by around 55% errors for the two assumed fiber transverse CTE values. Therefore, if it is assumed that there can exist high volume fraction areas and laminate effect are considered, it is concluded that the uncertainty of fiber transverse CTE values will cause difficulty for micromechanical analysis. For alternative method to predict fiber transverse CTE values, back calculation method was tried.

REFERENCES

1. Lee J. Alternative carbon fiber reinforced polymer(CFRP) composites for cryogenic applications. M.S. Thesis, Starkeville: Mississippi State University; 2004.
2. Tatiparthi AK. Investigation of microcrack growth in [0/90]s graphite epoxy composite laminates using x-ray microtomography. M.S. Thesis. New Orleans: University of New Orleans; 2004.
3. Whitley KS, Gates T. Thermal/mechanical response of a polymer matrix composite at cryogenic temperature. NASA/TM-2003-212171, Langley Research Center, Hampton, VA; 2003.
4. Final report of the x-33 liquid hydrogen tank test investigation team. Marshall Space Flight Center, Huntsville, AL, <http://x33.msfc.nasa.gov>; 2000.
5. Paris F, Correa E, Canas J. Micromechanical view of failure of the matrix in fibrous composite materials. *Composites Science and Technology* 2003;63:1041-52.
6. Kouris D, Tsuchida E. On the elastic interaction between two fibers in a continuous fiber composite under thermal loading. *Mechanics of Materials* 1991;12:131-46.
7. Dvorak GJ and Sejnoha M. Initial failure maps for ceramic and metal matrix composite laminates. *Modeling Simul. Mater. Sci. Eng* 1996;4;553-80.
8. Choi HS, Achenbach JD, Kim C. Micromechanical bilinear behavior of composite lamina subjected to combined thermal and mechanical loadings. *Mechanics of Composite Materials and Structures* 2001;8;135-55.
9. Bowles DE. Micromechanics thermal stress analysis of composites for space structure applications. *American Society of Mechanical Engineers* 1991;118;ASME

79-90

10. Zhu H, Achenbach JD. Radial matrix cracking and interphase failure in transversely loaded fiber composites. *Mechanics of Materials* 1991;11;347-56.
11. Sorensen BF, Talreja R. Effects of nonuniformity of fiber distribution on thermally-induced residual stresses and cracking in ceramic matrix composites. *Mechanics of Material* 1993;16;351-63.
12. Chandra N, Ananth CR, Garmestani H. Micromechanical modeling of process-induced residual stresses in Ti-24-Al-11Nb/SCS-6 composite. *Journal of Composites Technology & Research* 1994;16;37-47.
13. Li DS, Wisnom MR. Finite element micromechanical modelling of unidirectional fibre-reinforced metal-matrix composites. *Composites Science and Technology* 1994;51;545-63.
14. Fiedler B, Hojo M, Ochiai S, Scjulte K, Ochi M. Finite-element modeling of initial matrix failure in CFRP under static transverse tensile load. *Composites Science and Technology* 2001;61;95-105.
15. Fiedler B, Hojo M, Ochiai S. The influence of thermal residual stresses on the transverse strength of CFRP using FEM. *Composites Part A: Applied Science and Manufacturing* 2002;33;1323-26.
16. Ding W, Bowen P. Micromechanical modeling of unidirectional continuous sigma fiber-reinforced Ti-6A-4V subjected to transverse tensile loading. *Metallurgical and Materials Transaction A* 2002;33A;3045-54.
17. Chan WS, Johnson LA. Analysis of fiber/matrix interface in unidirectional fiber-

- reinforced composites. *Journal of Thermoplastic Composite Materials* 2002;15;389-402.
18. Aghdam MM, Falahatgar SR. Micromechanical modeling of interface damage of metal matrix composites subjected to transverse loading. *Composite Structures* 2004;66;414-20.
 19. Choi S, Sankar BV. A micromechanics method to predict the microcracking of the LH2 composite tank at cryogenic temperature. *Proceedings of the 5th International Congress on Thermal Stresses and Related Topics, Blacksburg, VA; 2003;441-4*
 20. Prabhacker RM. Estimation of effective elastic properties and interface stress concentrations in particulate composites by unit cell methods. *Acta Material* 2004;52;1263-70.
 21. Brockenbrough JR, Suresh S, Wienecke HA. Deformation of metal-matrix composites with continuous fibers: geometrical effects of fiber distribution and shape. *Acta Metall Mater* 1999;39;735-52.
 22. Gundel DB, Warriar SG, Miracle DB. The transverse tensile behavior of Sic-fiber/Ti-6Al-4V composites: 2. Stress distribution and interface failure. *Composites Science and Technology* 1999;59;1087-96.
 23. Bulsara VN, Talreja R, Qu J. Damage initiation under transverse loading of unidirectional composites with arbitrarily distributed fibers. *Composites Science and Technology* 1999;59;673-82.
 24. Honda K, Kagawa Y. Debonding criterion in the pushout process of fiber-reinforced ceramics. *Acta Mater* 1996;44;3267-77.

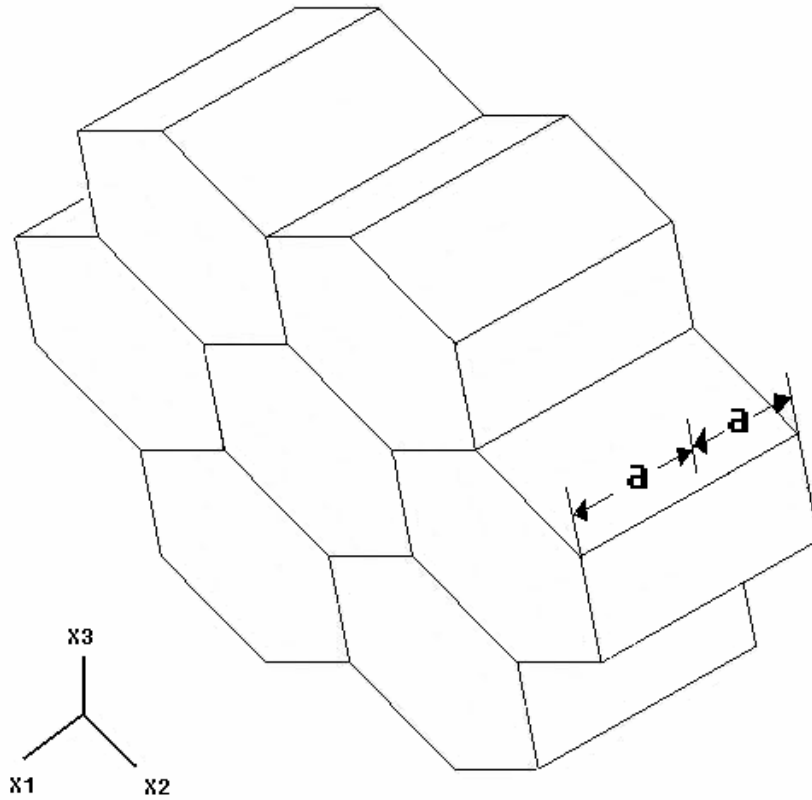
25. Thionnet A, Renard J. Multi-scale analysis to determine fiber/matrix debonding criteria in Sic/titanium composites with and without consideration of the manufacturing residual stresses. *Composites Science and Technology* 1977;58;945-55.
26. Kulkarni R. Characterization of carbon fibers: coefficient of thermal expansion and microstructure. M.S. Thesis, College Station, Texas A&M University; 2004.
27. Sun CT, Vaidya RS. Prediction of composite properties from a representative volume element. *Composite Science and Technology* 1996;56;171-9.
28. Li S. General unit cells for micromechanical analyses of unidirectional composite. *Composites: Part A: Applied Science and Manufacturing* 2000;32;815-26
29. Herakovich CT. *Mechanics of fibrous composites*. New York: John Wiley & Sons, 1998.
30. Elaseifi M. A new scheme for the optimum design of stiffened composite panels with geometric imperfections. Ph.D. Dissertation, Blacksburg: Virginia Polytechnic Institute and State University; 1998.
31. Ju J, Morgan RJ. Characterization of microcrack development in BMI-carbon fiber composite under stress and thermal cycling. *Journal of Composite Materials* 2004;38;2007-24
32. Rennick TS. Composite material manufacturing warpage-towards a better understanding through experimentation. Manufacture and Structures Laboratory, Colorado State University, <http://home.uchicago.edu/~trennick/defense.ppt>; 1998.
33. Liu Y. Anisotropic damage evolution in ceramic matrix composites. Ph.D.

Dissertation, Blacksburg: Virginia Polytechnic Institute and State University; 1997.

34. Brown TL. The effect of long-term thermal cycling on the microcracking behavior and dimensional stability of composite materials. Ph.D. Dissertation, Blacksburg: Virginia Polytechnic Institute and State University; 1977.

APPENDIX A

Periodic boundary conditions for the model of Figure 4.14



Between front surface and back surface

$$u_1(a, x_2, x_3) = u_1(-a, x_2, x_3) + \left\langle \frac{\partial u_1}{\partial x_1} \right\rangle 2a$$

$$u_2(a, x_2, x_3) = u_2(-a, x_2, x_3) + \left\langle \frac{\partial u_2}{\partial x_1} \right\rangle 2a$$

$$u_3(a, x_2, x_3) = u_3(-a, x_2, x_3) + \left\langle \frac{\partial u_3}{\partial x_1} \right\rangle 2a$$

APPENDIX B

Case 1): Carbon fiber/epoxy, HTA-12/#113 at room temperature [14]

	HTA-12	resin #113	HTA-12/#113
E_{11} (GPa)	235	3.9	163
E_{22}, E_{33} (GPa)	19.1		8.36
G_{12}, G_{13} (GPa)	24	1.45	8.07
G_{23} (GPa)	7.2		2.527
ν_{12}, ν_{13}	0.28	0.39	0.32
ν_{23}	0.33		0.55
$\alpha_{11} (\times 10^{-6} / C^{\circ})$	-0.4	57	-0.1
$\alpha_{22}, \alpha_{33} (\times 10^{-6} / C^{\circ})$	10		35

B.1. Experimental lamina properties of fiber HTA-12, resin #113, and HTA-12/#113 (vf: 60%) [14]

Case 2): Carbon fiber/epoxy P75/ERL1962, Carbon fiber/epoxy P75/934, and Carbon fiber/cyanate ester P75/RS at room temperature [34]

	P75/ERL1962 Vf=52.3%	P75/934 Vf=65.7%	P75/RS3 Vf=69%
E_{11} (GPa)	237	340	296
E_{22}, E_{33} (GPa)	6.23	6.96	6.65
G_{12}, G_{13} (GPa)	4.83	4.83	4.83
ν_{12}, ν_{13}	0.293	0.3	0.261
$\alpha_{11} (\times 10^{-6} / C^{\circ})$	-0.9	-1.17	-1.19
$\alpha_{22}, \alpha_{33} (\times 10^{-6} / C^{\circ})$	37.8	30.1	28.3

B.2. Material properties of P75/ERL1962, P75/934, and P75/RS3 composite systems at room temperature [34]

	P75	ERL1962	934	RS3
E_{11} (GPa)	550	3.7	4.14	2.68
E_{22}, E_{33} (GPa)	9.52			
G_{12}, G_{13} (GPa)	6.9	1.37	1.59	0.99
G_{23} (GPa)	3.38			
ν_{12}, ν_{13}	0.2	0.35	0.4	0.35
ν_{23}	0.4			
$\alpha_{11} (\times 10^{-6} / C^{\circ})$	-1.35	43.6	50.5	56.8
$\alpha_{22}, \alpha_{33} (\times 10^{-6} / C^{\circ})$	6.84			

B.3. Material properties of P75, ERL1962, 934, and RS3 at room temperature [34]

Case 3): IM7/977-3 at -196° , 23° , and 150°

	At -196°	At 23°	At 150°
E_{11}	182Gpa	180GPa	180GPa
E_{22}, E_{33}	11.7GPa	9.7GPa	6.9GPa
ν_{23}	0.33	0.33	0.35
G_{23}	9.2GPa	6.1GPa	5.5GPa
$\alpha_{11} (\times 10^{-6} / C^{\circ})$	0.18	0.18	0.18
$\alpha_{22}, \alpha_{33} (\times 10^{-6} / C^{\circ})$	20.4	23.4	23.4

B.4. Experimental lamina properties of IM7/977-3 (vf: 65%) [26]

	IM7
E_{11}	263.7Gpa
E_{22}, E_{33}	19.0GPa
ν_{12}, ν_{13}	0.2
ν_{23}	0.35
G_{12}, G_{13}	27.6GPa
G_{23}	6.89GPa
$\alpha_{11} (\times 10^{-6} / C^{\circ})$	-0.4
$\alpha_{22}, \alpha_{33} (\times 10^{-6} / C^{\circ})$	5.63

B.5. Experimental lamina properties of IM7

property	temperature		
	-196°	24°	149°
E	7.86	3.45	2.48
v	0.47	0.39	0.48
$\alpha (\times 10^{-6} / C^{\circ})$	32.51	44.69	51.62

B.6. Temperature dependent 977 epoxy properties

VITA

Seung-Don Zu was born in Korea. He obtained his Bachelor degree in aerospace engineering from Hankook Aviation University in Korea in February 2002. Upon completion of his master's work, he plans to have a job experience to further this research.

His permanent address is:

119-32 Dohadong, Namgu, Incheon, Republic of Korea

Phone: (82)-32-862-8375

e-mail: aerozu@tamu.edu or aerozu@gmail.com